



# Finite Element Analysis-Based Pre-operative Planning Applications of Tooth, Tibia, and Femur Bones

Submitted to the Graduate School of Natural and Applied Sciences  
in partial fulfillment of the requirements for the degree of

Doctor of Philosophy

In Department of Biomedical Technologies

by

Samet Çıklaçandır

ORCID 0000-0003-2076-2400

August, 2023

This is to certify that we have read the thesis **Finite Element Analysis-Based Pre-operative Planning Applications of Tooth, Tibia, and Femur Bones** submitted by **Samet ıklaçandır**, and it has been judged to be successful, in scope and in quality, at the defense exam and accepted by our jury as a DOCTORAL THESIS.

**APPROVED BY:**

**Advisor:** **Assoc. Prof. Dr. Yalçın İşler**  
İzmir Kâtip Çelebi University

**Committee Members:**

**Assoc. Prof. Dr. Yakup Kutlu**  
Iskenderun Technical University

**Assoc. Prof. Dr. Gökçenur Gökçe Kara**  
Izmir Katip Celebi University

**Assist. Prof. Dr. Mustafa Berkant Selek**  
Ege University

**Assist. Prof. Dr. İbrahim Kaya**  
Izmir Katip Celebi University

**Date of Defense: August 07, 2023**

# Declaration of Authorship

I, **Samet Çıklaçandır**, declare that this thesis titled **Finite Element Analysis-Based Pre-operative Planning Applications of Tooth, Tibia, and Femur Bones** and the work presented in it are my own. I confirm that:

- This work was done wholly or mainly while in candidature for the Doctoral degree at Izmir Katip Celebi University.
- Where any part of this thesis has previously been submitted for a degree or any other qualification at this university or any other institution, this has been clearly stated.
- Where I have consulted the published work of others, this is always clearly attributed.
- Where I have quoted from the work of others, the source is always given. This thesis is entirely my own work, with the exception of such quotations.
- I have acknowledged all major sources of assistance.
- Where the thesis is based on work done by myself jointly with others, I have made clear exactly what was done by others and what I have contributed myself.

Date: 07.08.2023

---

# Finite Element Analysis-Based Pre-operative Planning Applications of Tooth, Tibia, and Femur Bones

## Abstract

In pre-operative planning or training, 3D modeling and subject-specific bone model can be utilized to facilitate challenging surgical operations. Due to the development of 3D printing and simulations, this procedure has become more effective and feasible. Additionally, finite element analysis (FEA) can converge the results of mechanical analysis, making the creation of bone models and various medical equipment faster and more reliable. However, the impact of simulations and mechanical testing on models is still disputed. Therefore, in this study, the analysis including two different types of fractures, femoral head and medial malleolar was performed using 3D printed and artificial bones. In addition, in the orthodontic treatment, the miniscrews used for anchorage control were simulated to determine the most efficient application methods. The study goes into substantial detail on all the different tools required, the method to follow, and any issues that may arise.

Using interactive medical imaging control system software, a CT scan of a patient's lower abdomen and a DVT scan of another patient's head were transformed into 3D images. The femur, mandible, and teeth were segmented using Mimics. The models of the femur were produced using a 3D printer, also it was imported to the FEA software. The compression tests were conducted on the femurs until the fracture occurred. For the medial malleolus (MM), the test was repeated by placing two different plates on

composite tibia bones. In addition, different miniscrew head designs and lengths were created and simulations on the mandible and bone block for different insertion scenarios were completed. The correlation between the compression test and simulations was evaluated statistically based on the stress, strain, displacement and load-to-failure results.

The results show that experimental analysis and the CT scan-based FEA were compatible both for the stress distributions and the strain values as predicted by the models ( $R^2=0.99$ ). In the MM study, it was determined significant differences between the two plates. In the miniscrew study, the minimum and maximum stresses were calculated as 18.61 MPa and 37.11 MPa at 6 mm and 10 mm lengths, respectively. According to the insertion angles, the lowest stress was observed at  $60^\circ$ , while the highest stress was found at  $-15^\circ$ . In the designs of miniscrew, the bracket head generated the lowest von Mises stress of 5.67 MPa. On the other hand, the button head had the highest von Mises stress, at 22.4 MPa.

The prescribed process flow and all tools could be used in clinical settings for the pre-planning of the surgeries and also as an educational tool in the biomedical engineering field. Moreover, it was determined that the use of longer miniscrews increased the stress on the mandible. Since the need for low stress is substantial for the primary stability of the miniscrew, this study demonstrated that the bracket head miniscrew is the optimal head design.

**Keywords:** Anchorage control, 3D printing, femoral head fractures, finite element analysis, medial malleolus fractures, miniscrew, patient-specific modeling

# Sonlu Elemanlar Analizi Tabanlı Diş, Kaval ve Uyluk Kemiklerinin Ameliyat Öncesi Planlama Uygulamaları

## Öz

Ameliyat öncesi planlama veya eğitimde, zorlu cerrahi operasyonları kolaylaştırmak için 3D modelleme ve kişiye özgü kemik modeli kullanılabilir. Bu prosedür, 3D baskı ve simülasyonların gelişmesi nedeniyle daha etkili ve uygulanabilir hale geldi. Bunun yanında, sonlu elemanlar analizi (SEA) mekanik analiz sonuçlarına yakınsayarak kemik modellerinin ve çeşitli tıbbi ekipmanların oluşturulmasını daha hızlı ve daha güvenilir hale getirebilir. Fakat, simülasyonların ve mekanik testlerin modeller üzerindeki etkisi hala tartışmalıdır. Bu sebeple bu çalışmada femur başı ve medial malleol olmak üzere iki farklı kırığı içeren analiz 3B baskılı ve yapay kemikler kullanılarak gerçekleştirilmiştir. Bununla beraber ortodontik tedavide ankraj kontrolü için kullanılan minividalar, en verimli uygulama yöntemleri belirlemek için simüle edilmiştir. Çalışma, gerekli tüm farklı araçlar, izlenecek yöntem ve ortaya çıkabilecek sorunlar hakkında önemli ayrıntılara girmektedir.

İnteraktif tıbbi görüntüleme kontrol sistem yazılımı kullanılarak, bir hastanın alt karın bölgesinin BT taraması ve başka bir hastanın kafasının DVT taraması 3 boyutlu görüntülere dönüştürüldü. Femur, mandibula ve dişler Mimics kullanılarak bölümlere ayrıldı. Femur modelleri 3B yazıcı kullanılarak üretildi, ayrıca SEA yazılımına aktarıldı. Basma testleri, femurlar üzerinde kırık oluşana kadar uygulandı. Medial malleolus (MM) için kompozit tibia kemikleri üzerine iki farklı plak yerleştirilerek test

tekrarlandı. Bunun yanında farklı minivida baş tasarımları ve uzunlukları oluşturulmuş ve farklı yerleştirme senaryoları için mandibula ve kemik bloğu üzerinde simülasyonlar tamamlanmıştır. Basma testi ve simülasyonlar arasındaki korelasyon, stres, gerinim, yer değiştirme ve başarısızlık yükü sonuçlarına göre istatistiksel olarak değerlendirildi.

Deneysel analizin ve BT taramasına dayalı SEA'nın, modellerin öngördüğü gibi hem gerilim dağılımları hem de gerinim değerleri için uyumlu olduğunu sonuçlar göstermektedir ( $R^2=0.99$ ). MM çalışmasında iki plak arasında önemli farklılıklar tespit edilmiştir. Minivida çalışmasında ise minimum ve maksimum gerilmeler sırasıyla 6 mm ve 10 mm uzunluklarda 18,61 MPa ve 37,11 MPa olarak hesaplanmıştır. Yerleştirme açılarına göre en düşük gerilme  $60^\circ$ 'de, en yüksek gerilme  $-15^\circ$ 'de görülmüştür. Minivida tasarımlarında, braket başı 5,67 MPa ile en düşük von Mises gerilimini oluşturmuştur. Diğer yandan, düğme başı 22,4 MPa ile en yüksek von Mises gerilimine sahipti.

Öngörülen süreç akışı ve tüm araçlar, klinik ortamlarda ameliyat öncesi planlama için ve ayrıca biyomedikal mühendisliği alanında bir eğitim aracı olarak kullanılabilir. Buna ek olarak daha uzun minivida kullanımının mandibula üzerindeki stresi arttırdığı belirlendi. Minividanın birincil stabilitesi için düşük gerilim ihtiyacı önemli olduğundan, bu çalışma braket başlı mini vidanın en uygun kafa tasarımı olduğunu göstermiştir.

**Anahtar Kelimeler:** Ankraj kontrolü, 3B baskı, femur başı kırıkları, sonlu elemanlar analizi, medial malleol kırıkları, minivida, hastaya özel modelleme

*This thesis work is dedicated to my wife, Fatma, who has been a constant source of support and encouragement during the challenges of graduate school and life. I am truly thankful for having you in my life. This work is also dedicated to my parents, Selma and Muammer, who have always loved me unconditionally and whose good examples have taught me to work hard for the things that I aspire to achieve.*

# Acknowledgements

This effort is the result of numerous, difficult compromises. Above all, I would like to express my gratitude to my invaluable wife, who contributed greatly to the realization of this thesis. At the same time, I am grateful to my mother, father, and all my family for their unwavering support. Foremost I am extremely grateful to my supervisors, Assoc. Prof. Dr. Yalçın İşler for their invaluable advice, continuous support, and patience during my PhD study. I would also like to thank Assoc. Prof. Dr. Şenay Mihçin for serving on my thesis and providing helpful feedback and suggestions.

Furthermore, this thesis was supported by Izmir Katip Celebi University Scientific Research Council Agency as project number 2023-TDR-FEBE-0005.

# Table of Contents

Declaration of Authorship.....	ii
Abstract .....	iii
Öz.....	v
Acknowledgements .....	viii
List of Figures .....	xi
List of Tables.....	xiv
List of Abbreviations.....	xvi
List of Symbols .....	xix
<b>1 Introduction.....</b>	<b>1</b>
1.1 Femoral Head Fractures .....	1
1.2 Medial Malleolar Fractures .....	2
1.3 Additive Manufacturing Technologies.....	2
1.3.1 Fused Deposition Modeling (FDM).....	3
1.3.2 Selective Laser Sintering (SLS) .....	8
1.3.3 Binder Jetting (BJ).....	10
1.3.4 Stereolithography (SLA) .....	12
1.3.5 Comparison of Printing Technologies.....	13
1.4 Creating Artificial Bones .....	14
1.4.1 Commercial Composite Bone Models.....	15
1.4.2 3D Printed Bone Models .....	16
1.5 Imaging Modalities .....	18
1.6 3D Reconstruction.....	19
1.7 Mechanical Analysis .....	22

1.8 Finite Element Method.....	26
<b>2 Finite Element Analysis in Orthodontics.....</b>	<b>29</b>
<b>3 Materials &amp; Methods.....</b>	<b>35</b>
3.1 Analysis of Femoral Head Fractures.....	35
3.1.1 3D Image Reconstruction.....	35
3.1.2 3D Printing of Models.....	37
3.1.3 Compression Testing of Specimens.....	39
3.1.4 Mechanical Simulation.....	41
3.2 Biomechanical studies in composite bones.....	42
3.2.1 Preparation of specimens and the test environment.....	43
3.2.2 Design of gripper for static tester and solutions to the problems encountered.....	44
3.2.3 Statistical analysis.....	49
3.3 Analysis of Miniscrews Stability.....	49
3.3.1 The Effect of Miniscrew Head Designs.....	49
3.3.2 The Effect of Application of Miniscrew to Mandible in Different Ways.....	51
<b>4 Results.....</b>	<b>55</b>
4.1 Experimental results of Femur.....	55
4.2 Computational results of Femur.....	57
4.3 Results of plates in composite bone.....	59
4.4 FE results of miniscrew applications.....	62
<b>5 Discussion.....</b>	<b>71</b>
<b>6 Conclusion.....</b>	<b>81</b>
<b>References.....</b>	<b>85</b>
<b>Appendix.....</b>	<b>104</b>
<b>Curriculum Vitae.....</b>	<b>105</b>

# List of Figures

Figure 1.1	FFF technology working principle .....	4
Figure 1.2	Working principles and components of SLS technology .....	9
Figure 1.3	Principle of operation for BJ technology.....	11
Figure 1.4	Working principle of SLA technology .....	13
Figure 1.5	The steps to follow for 3D reconstruction up to 3DP.....	22
Figure 1.6	Components of the tensile tester.....	24
Figure 2.1	Schematic representation of geometry properties of miniscrew ((a) Head diameter, (b) head length, (c) collar length, (d) body length, (e) inner diameter, (f) outer diameter, (g) length of screw, (h) pitch depth, (i) apical phase angle, (j) pitch width, (k) thread angle, (l) flank, (m) thread shapes, (n <sub>1</sub> ) cylindrical miniscrew, (n <sub>2</sub> ) tapered miniscrew, (r <sub>1</sub> ) self-drilling, (r <sub>2</sub> ) self-tapping, (p) different types of head designs, and (o) miniscrews manufactured with different designed types) [116,118,119].....	32
Figure 3.1	(a) The 3D image of the lower abdomen removed from soft tissue, (b-c) The left and right femoral heads' respective 3D models, (d-e) After editing operations, the 3D model of the left and right femoral heads.....	36
Figure 3.2	Femoral head models printed with BJ technology .....	37
Figure 3.3	The representative measurements of left and right models, as well as the cross-section area of the left femur .....	38
Figure 3.4	The placement of the cylindrical specimen between the compression plates and deformation of the specimen at the end of the compression test.....	39

Figure 3.5 (a) The left femur placed on the grippers of the Shimadzu universal testing machine, (b) Failure of the specimen as a result of testing, (c-d) Fracture path after applying load in the left model and the right model, respectively .....	40
Figure 3.6 The meshing of (a) the left model, (b) the right model, (c-d) The direction of the force and fixed support points on the left model and right model, respectively .....	42
Figure 3.7 Tibia bone preparation and installation of gripper apparatus for testing	44
Figure 3.8 (a) Fixing points of the sliding mechanism to the tensile tester, (b-c) 3D drawing of the sliding mechanism, (d-e) 3D printing of the mechanism and its placement on the tester.....	45
Figure 3.9 Diagram of the error-detecting system .....	46
Figure 3.10 (a) Installation of a movable camera mechanism, (b) Adapting the camera system to the 3D printer, (c) Raw colour image captured from the camera, (d) Black and white image with detected edges as a result of image processing.....	47
Figure 3.11 (a) 3D drawing of the filament holder mechanism, (b) Calibration of load cell with standard weight, (c) Measurement of filament weight with precision scale and validation process with the system, (d) Adaptation and operation of all parts of the system to the 3D printer .....	48
Figure 3.12 (a-f) Dimensions and 3D drawings of miniscrew; cross head, mushroom head, button head, bracket head, and through-hole head, respectively, (g) Definition of boundary conditions, (h) Meshing .....	50
Figure 3.13 Workflow of the FEA process, (a) 3D image segmentation, (b) Drawing of miniscrews in CAD software, (c) Angulation relative to the frontal plane, (d) Transparent view of miniscrew inserted between teeth, and screw hole after removal miniscrew, (e) The meshing of mandible and miniscrew, (f) Force and fixed supports surfaces, (g) Force directions according to power arm.....	53
Figure 4.1 (a) The compression test results for six cylindrical specimens and calculation of Young's modulus from curves.....	56

Figure 4.2 (a) The left model's and (b) the right model's stress distributions on the FE models .....	58
Figure 4.3 Comparison of experimental results and simulation results for the left model.....	58
Figure 4.4 Comparison of experimental results and simulation results for the right model.....	59
Figure 4.5 Boxplots of load-to-failure of two plates.....	60
Figure 4.6 Measurement data of filament weight while the printer is running.....	61
Figure 4.7 Measurement of the distance between the nozzle and the part according to the layer number.....	62
Figure 4.8 Stress distributions of Miniscrew head types isolated from bone block (cross head, mushroom head, button head, bracket head, through-hole head, respectively) .....	63
Figure 4.9 (a-e) Von Mises stress distributions of the miniscrew cavity, (f-j) Total deformations of miniscrew head types, (k-o) Equivalent strain results of miniscrew head types, for all images, from left to right, cross head, mushroom head, button head, bracket head, and through-hole head, respectively .....	64
Figure 4.10 Mesh convergence analysis result for von Mises stress .....	65
Figure 4.11 (a) Von Mises stress results of all models, (b) the graph of mesh convergence analysis for three models in different lengths .....	67
Figure 4.12 (a) Sagittal view of stress distributions on the mandible according to insertion angles and miniscrew lengths, (b) Frontal view of stress distributions of miniscrew separated from mandible and teeth models .....	68

# List of Tables

Table 1.1 Movable XYZ planes concerning coordinate systems in different working principles.....	4
Table 1.2 CAD and CAM software features [18,19] .....	5
Table 1.3 Comparison of 3DP Material Properties [21,22] .....	7
Table 1.4 Comparison of popular 3D printers commonly encountered in the market [50,51].....	14
Table 1.5 Tensile and compressive properties of natural and artificial bones [59,64–68] .....	17
Table 1.6 Properties of both commercial and free software for 3D reconstruction [79,80].....	21
Table 1.7 The following formulas are calculated from the data obtained using tensile testing.....	26
Table 1.8 Commonly available FE software in the market [92].....	27
Table 2.1 General characteristics and dimensions of miniscrews available in the market (Dimensions may vary according to different brands) [116,117].....	31
Table 3.1 The number of elements and nodes of the models remeshed according to different application variations of all models.....	52
Table 3.2 Elastic modulus and poisson’s ratio of FE models [126,128].....	54
Table 3.3 Components of forces vector according to angles (N) [141] .....	54

Table 4.1	Time spent on each process .....	57
Table 4.2	The statistical comparison of medial malleolar anatomic plate (MP) and tubular plate (TP) .....	60
Table 4.3	Analysis results for each model .....	63
Table 4.4	Meshing details of all models .....	65
Table 4.5	Averages of von Mises stress values and statistical analysis results (* indicates statistically significant differences and the significant value was 0.05).....	69
Table 4.6	P-values for each condition (* indicates statistically significant differences and the significant value was 0.05).....	69

# List of Abbreviations

3D	Three-Dimensional
3DP	3D Printing
FDM	Fused Deposition Modeling
SLS	Selective Laser Sintering
BJ	Binder Jetting
SLA	Stereolithography
FFF	Fused Filament Fabrication
CAD	Computer-Aided Drawing
CAM	Computer-Aided Manufacturing
RP	Rapid-Prototyping
PLA	Polylactic Acid
ABS	Acrylonitrile Butadiene Styrene
PEEK	Polyetheretherketone
PETG	Polyethylene Terephthalate Glycol
TPU	Thermoplastic Polyurethanes
PET	Polyethylene Terephthalate
PC	Polycarbonate
PVA	Both polyvinyl acetate
BVOH	Butenediol Vinyl Alcohol Copolymer
HIPS	High Impact Polystyrene
MRI	Magnetic Resonance Imaging
CT	Computed Tomography

PA	Polyamide
PS	Polystyrene
TPE	Thermoplastic Elastomers
PP	Polypropylene
PE	Polyethylene
UHMWPE	Ultra-high-molecular-weight polyethylene
Ti6AlV4	Grade 5 Titanium Alloy
SiO <sub>2</sub>	Silicon Dioxide
Si <sub>3</sub> N <sub>4</sub>	Silicon Nitride
Al <sub>2</sub> O <sub>3</sub>	Aluminum Oxide
BaTiO <sub>3</sub>	Barium Titanate
SiC	Silicon Carbide
TiC	Titanium Carbide
HA	Hydroxyapatite
CP	Calcium Phosphates
(CaSO <sub>4</sub> ) <sub>2</sub> H <sub>2</sub> O	Calcium Sulfate Hemihydrate
PET	Positron Emission Tomography
HU	Hounsfield Unit
DICOM	Digital Imaging and Communications in Medicine
FEM	Finite Element Method
FE	Finite Element
FEA	Finite Element Analysis
TADs	Temporary Anchorage Devices
TiA	Titanium Alloy
SS	Stainless Steel
FHL	Femoral Head Length
VDH	Vertical Diameter of the Head

FOV	Field of View
C <sub>7</sub> H <sub>9</sub> NO <sub>3</sub>	Allomethadione
DVT	Dental Volumetric Tomography
CPU	Central processing unit
GHz	Gigahertz
GB	Gigabyte
RAM	Random-access memory
MP	Medial malleolar anatomic plate
TP	Tubular plate

# List of Symbols

$\%$	Percent
$\pm$	Plus or minus
$\sim$	Approximately equal
$\varepsilon_t$	Total strain
$\mu$	Micro
$\sigma$	Stress [MPa]
$\varepsilon$	Strain
$\sigma_T$	True Stress [MPa]
$\varepsilon_T$	True Strain
$L_0$	Initial Length [mm]
$L$	Final Length [mm]
$E$	Young Modulus [MPa]
$A_0$	Original Cross Sectional Area [mm <sup>2</sup> ]
$A$	Final Cross Sectional Area [mm <sup>2</sup> ]
$\nu$	Poisson's Ratio
$F$	Force [N]
$m$	Mass [kg]
$\$$	Dolar
$W$	Width [mm]
$D$	Depth [mm]
$H$	Height [mm]
$\delta$	The percentage deviation (%)

$\sigma_{EXP}$	Experimental result
$\sigma_{FE}$	Finite element result
$E_{tana}$	Tangent modulus of elasticity
$\Delta\sigma$	Difference between compressive stresses
$\Delta\varepsilon$	Difference between axial strains
g	gram
cm <sup>3</sup>	Cubic centimetre
mm <sup>2</sup>	Square millimeter
MPa	Megapascals
GPa	Gigapascals
Pa	Pascals
°	Degree

# Chapter 1

## Introduction

### 1.1 Femoral Head Fractures

The longest bone of the human body, which is located in legs, is the femur. Since the weight of the whole body is shared by both legs, femur plays a crucial role in lower body kinetics for load-bearing, especially. In addition, the acetabular bone, a part of the pelvis, contacts to the femur bone to transmit the body weight to other bone structures including tibia and the fibula. A problem in these bones may affect the lower body kinetics of the skeletal system.

Fractures may result from skeletal issues brought on by osteoporosis, hereditary illnesses, severe traumas, and accidents [1]. In particular, fractures of the hip, which consists of the femoral head and acetabulum, affect the life quality of patients. Besides, these fractures cause severe trauma and lead to increase in the mortality rate [2]. These fractures become more common as people age, and their recovery takes longer. In Turkey, there were about 24,000 hip fractures overall in 2010; by 2035, that number is predicted to rise to 64,000 [3]. By 2050, there will be 6.26 million hip fractures yearly due to an aging population worldwide [4].

Moreover, the treatment of these fractures requires open surgeries, resulting in severe blood loss and intense pain, in general. Planning prior to such operations is necessary to increase the success of the surgeries [5]. The pre-operation planning, however, is exceedingly challenging. For this purpose, 3D modeling and printing technologies may be useful to visualize body parts and give touchable models in detail to physicians.

## 1.2 Medial Malleolar Fractures

Ankle fractures are frequent injuries, accounting for 17% of all hospitalized fractures [6]. It is a condition that can be observed at any age as a result of exposure of the ankle to impact, crashing, and falling. Ankle stability is mostly dependent on the medial malleolus. The ankle is a joint in which the talus body is bounded by the medial malleolus, tibial plafond, and distal fibula, and stability is provided by the strong ligaments between these bones [7]. The best fixation technique for these injuries, which might involve using a K-wire, tension band, a screw alone, or a variety of plate applications, is still debatable [8]. The debate intensifies in vertical shear fractures, which happen when a supination adduction force is applied across the medial malleolus articular surface [9]. These vertical fractures have been proven to be biomechanically better fixed using neutralization plates than with screws [8]. On the other hand, compression brought about by screws passing perpendicular to the fracture line produces a significant advantage in screw fixation techniques [10]. Surgeons created a unique medial malleolus plate with two holes for cannulated compression screws and a sliding compression mechanism to combine the benefits of both techniques. Therefore, in order to determine the most effective treatment strategy, a biomechanical analysis of several plates is required.

## 1.3 Additive Manufacturing Technologies

Additive manufacturing, also known as three-dimensional (3D) printers, is becoming more and more widespread and is among the most important elements of the future. The prompt development of additive manufacturing technology has been stimulated by the demand for increased versatility and the evolution of custom-made goods [11]. They offer rapid prototyping, robustness, diversity, user freedom, low electricity consumption, and do-your-self. In addition, it is in almost every environment with affordable devices and cheap material costs. 3D printing technology in medical applications is promoting and is predicted to enhance healthcare [12]. The most frequent of these applications is the personalization of medical equipment. Some of the benefits this technology brings are productivity, cooperation, and the democratization of design and production. In addition, today's 3D printing (3DP)

technology offers a significant possibility to assist medical corporations in developing more specialized equipment, enabling the rapid manufacture of medical implants, and altering how doctors and surgeons approach surgical planning [13]. In terms of maximal therapeutic, reduction of cost and more accurate surgical treatment, it has been demonstrated that custom-made manufacturing is far more beneficial than ready-made manufacturing [14].

3D printers used in the market can be classified according to their working principle. The most common among these are Fused Deposition Modeling (FDM), Selective Laser Sintering (SLS), Binder Jetting (BJ), and Stereolithography (SLA) [15]. These technologies were mentioned in detail in the following sections.

### 1.3.1 Fused Deposition Modeling (FDM)

FDM, also known as Fused Filament Fabrication (FFF), the parts are produced by the deposition of the melted material in layers. S. Scott Crump evolved FDM in the late 1980s, and Stratasys released it around 1990 [16]. This method brings the thermoplastic material to certain melting temperatures and converts it to a fluid state. The filament is heated to a usable temperature using a heater block [17]. In addition, there is a temperature control unit with sensors. A smaller diameter is used to push the heated filament out of the nozzle. The fluid material is shaped using the three-axis moving mechanisms and the fans are used for fast cooling. The working principle of the FDM printer is shown in Figure 1.1. The nozzle moves in X and Y planes using two stepper motors. The build platform moves up and down vertically and the shaping process occurs. Unlike these, there are different types of printers that have a fixed nozzle and a mobile build platform. Printers with different movement combinations available in the market are given in Table 1.1. The reason for these movement differences is due to the reference coordinate system. Coordinate systems consist of three different types: cartesian, delta and polar.

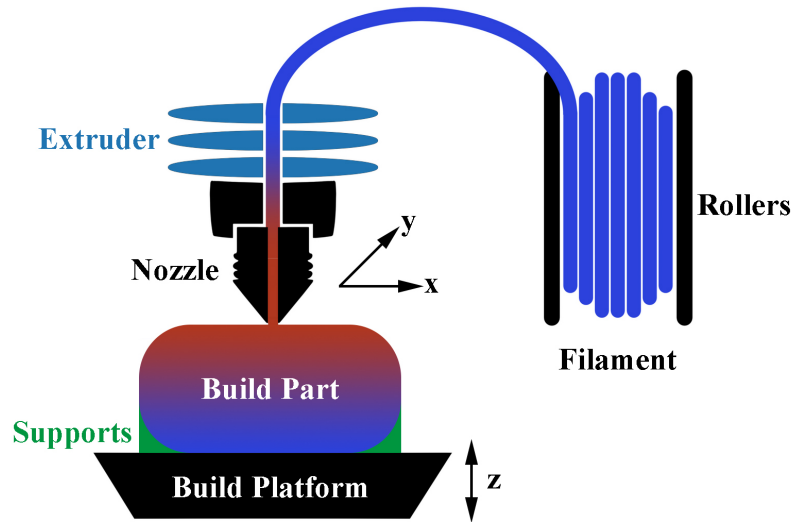


Figure 1.1: FFF technology working principle

Table 1.1: Movable XYZ planes concerning coordinate systems in different working principles

Printhead	Build Platform
X, Z	Y
X, Y	Z
X, Y, Z	-
Z	X, Y
X	Y, Z

It is possible to describe the software for completing the 3D print process in two different ways. These are 3D modeling (computer aided drawing (CAD)) and Slicers & 3D Printer Hosts (Computer-aided manufacturing (CAM)) software. In the 3D modeling process, the 3D part is drawn using many different CAD software such as SolidWorks, Autodesk Inventor, TinkerCAD, FreeCAD, Fusion 360, AutoCAD, Catia, Rhino, Siemens NX and etc. Although this software has advantages over each other, some of them are commercial and some are free. On the other hand, CAM converts CAD drawings into particular instructions for manufacturing devices. The software to be used in this process can be listed as Cura, Simplify3D, Slic3r,

3DPrinterOS, OctoPrint, and AstroPrint. A detailed comparison of all these software is shown in Table 1.2.

Table 1.2: CAD and CAM software features [18,19]

Software	Usage	Operating system	File Format (Export/Import)*	Pricing**
SolidWorks	Design	Windows	ACIS, CATIA, DXF/DWG, IGES, PARASOLID, STEP, STL	\$1295/Annually
Autodesk Inventor	Design	Windows	DWG, DWF, DWFx, IGES, JT, OBJ, SAT, STEP, STL, CATIA, PARASOLID, Pro/ENGINEER	\$2300/Annually
TinkerCAD	Design	Browser	STL, OBJ, GLTF, USDZ, SVG	Free
FreeCAD	Design	MacOS Windows	STEP, IGES, STL, SVG, DXF, OBJ, IFC, DAE	Open Source
Fusion 360	Design	MacOS Windows	F3D, IGES, SAT, SMP, STEP, FBX, OBJ, STL	\$382/Annually
Catia	Design	Windows	STL, 3D XML, CATIA, DXF, IGES, STEP, VRML	\$12000-\$15000
Rhino	Design	MacOS Windows	3DM, 3DS, DWG, IGES, FBX, OBJ, TXT, RAW, SLDPRJT, SLDASM, STEP, STL	\$1075
Siemens NX	Design	MacOS Windows	JT, IGES, DXF, DWG, STEP, SOLID EDGE, PARASOLID, PLMXML, STL	\$6900/Annually
Cura	Slicer 3D Printer Host	MacOS Windows	STL, OBJ, X3D, 3MF	Free
Simplify3D	Slicer 3D Printer Host	MacOS Windows	STL, OBJ, 3MF, GCODE, X3G, MAKERBOT, 3W, G3DREM, BFB	\$199
Slic3r	Slicer 3D Printer Host	MacOS Windows	STL, OBJ, AMF	Open Source
3DPrinterOS	Slicer 3D Printer Host	Browser Cloud-Based	3DS, 3MF, AMF, OBJ	Free
OctoPrint	Slicer 3D Printer Host	Browser MacOS Windows	STL, OBJ, 3MF	Open Source
AstroPrint	Slicer 3D Printer Host	Browser	STL, GCODE, X3G	Free

\* Not all formats are listed.

\*\*Additional tools are not included in the prices. May not include maintenance fees.

Software may generate file extensions in a variety of forms, but when transferring formats between applications, it must support functions like reading and editing. Therefore, rapid prototyping (RP) requires software that can process STL files, a universal language. The STL file created with CAD software should be converted to G-Code format that can be read by 3D printers. There is software from various companies in the market for this conversion. Some of this software is compatible for many different types of 3D printers. The most popular among these is Cura (Ultimaker B.V., ED Utrecht, Netherlands). There are several printing options available with this free program that can be utilized with various 3D printers. It has integration with CAD software such as SolidWorks, Autodesk Inventor, and Siemens NX within an ecosystem. At the same time, it can perform remote printing and queue management, real-time monitoring. In addition to Cura, it is accessible in various commercial software.

The most popular materials in FDM are polylactic acid (PLA) and acrylonitrile butadiene styrene (ABS), whose thermal and rheological characteristics facilitate the production process [20]. In addition, filaments such as nylon, polyetheretherketone (PEEK), thermoplastic polyurethanes (TPU), polyethylene terephthalate (PET), polycarbonate (PC) and composite are frequently used for FDM devices. Comparison of these materials with each other is shown in Table 1.3 in detail.

Table 1.3: Comparison of 3DP Material Properties [21,22]

Materials	Pros	Cons	Extruder Temperature ( $\pm 10^{\circ}\text{C}$ )	Bed Temperature ( $\pm 10^{\circ}\text{C}$ )	Pricing (\$/kg)
PLA	<ul style="list-style-type: none"> <li>• Easy of Printing</li> <li>• High Visual Quality</li> <li>• Biocompatible</li> </ul>	<ul style="list-style-type: none"> <li>• Low Impact Resistance</li> <li>• Low Heat Resistance</li> </ul>	210-215	60	10-20
ABS	<ul style="list-style-type: none"> <li>• High Heat Resistance</li> </ul>	<ul style="list-style-type: none"> <li>• Low Elongation at break</li> </ul>	240-255	110	20
Nylon	<ul style="list-style-type: none"> <li>• High Impact Resistance</li> <li>• Durable</li> <li>• Flexible</li> </ul>	<ul style="list-style-type: none"> <li>• Low Layer Adhesion</li> <li>• Low Humidity Resistance</li> </ul>	250	90	30-50
PEEK	<ul style="list-style-type: none"> <li>• Biocompatible</li> <li>• High Strength</li> </ul>	<ul style="list-style-type: none"> <li>• Lack of Thermoformability</li> <li>• Complexity</li> <li>• High Cost</li> </ul>	400	130	600-1000
TPU	<ul style="list-style-type: none"> <li>• High Elongation at break</li> <li>• High Impact Resistance</li> <li>• Excellent Resistance to Abrasion</li> </ul>	<ul style="list-style-type: none"> <li>• Difficulty in printing</li> <li>• Difficult to Post-process</li> </ul>	220-250	50	30-50
PET	<ul style="list-style-type: none"> <li>• Easy of Printing</li> </ul>	<ul style="list-style-type: none"> <li>• Low Elongation at break</li> </ul>	240-270	90-110	20-30
PC	<ul style="list-style-type: none"> <li>• High Heat Resistance</li> <li>• High Impact Resistance</li> </ul>	<ul style="list-style-type: none"> <li>• Susceptible to Scratching</li> <li>• High Cost</li> </ul>	250	115	40-60

The preferred material is changed according to the purpose. In medical applications, a biocompatible material should be used. Among these materials, PLA, PEEK, PETG (Polyethylene terephthalate glycol) stand out with their biocompatibility features [23]. Due to their surface roughness, non-toxicity, high level of sterilization, and ease of processing, these materials exhibit excellent outcomes in terms of cell adhesion and proliferation.

FDM uses support material to create complex shaped parts. This feature helps maintain the structural integrity of the part until it is reinforced and supports overhanging structures throughout the process [24]. Support materials may be readily broken and removed from the main part since they can be printed with various infill ratios by adjusting the parameters. On the other hand, some printer types can comply with soluble support materials differently from the main filament. In this manner, the support material dissolves without the need of any physical force by employing practical solvents. Both polyvinyl acetate (PVA) and the butenediol vinyl alcohol copolymer (BVOH), which is suitable with a wide range of materials, are completely soluble in water. High Impact Polystyrene (HIPS), another soluble support material, is widely used with ABS, PC. It can be dissolved, but only when d-limonene is used as the solvent [25].

As feeding materials that pass through the nozzle, range from 1.75 mm to 3 mm in diameter circular filaments is employed [26]. This diameter varies according to the printer. To prevent difficulties with jamming, this must fit with the nozzle on a printer. Even though 1.75 mm filament is now quite common, numerous suppliers still make 3 mm filament. Fast printing, low power requirements, low cost, and high printing accuracy are achieved with the thin filament, while low filament bending, low moisture absorption, and high extruder flow are obtained with the thick filament [27].

As a result, there are many parameters that affect the print quality of FFF technology. The most optimal parameter setting varies according to the printer and the material. This ends with the end user wasting a lot of filaments to find the best settings. No complete solution has yet been found for this problem. The most crucial of these parameters are as follows: printer speed, layer thickness, infill density, pattern, build orientation, raster angle, nozzle diameter, retraction, cooling, and adhesion type [28].

### 1.3.2 Selective Laser Sintering (SLS)

SLS is the technique of producing parts by processing CAD models or obtaining data from various 3D digitizing systems such as Magnetic Resonance Imaging (MRI), Computed Tomography (CT). Powder particles made of thermoplastic materials are combined using the guidance of the laser system, which is the infrared heating beam, and production is carried out layer by layer [29]. The components of the SLS are

described in Figure 1.2. The printing chamber is completely filled with powder so that the upper surface is flat and smooth. The powder-filled bed also provides support to parts during the printing, thereby, material consumption can be reduced due to the reusability of the powder material. In addition, because there is no removal of the support material from the part, it saves time compared to other methods and facilitates the production of more complex parts. The laser scanner system, enabling very fast printing, is selectively directed onto the powder so that a small amount of heat is sufficient to melt the plastic powder [30]. When the process of the powders on the upper layer is finished, the horizontally moving piston is elevated one layer and the upper layer is filled with the new powder by means of a roller. The horizontally moving piston is raised one layer once the process of transferring the powders to the top layer is complete, and a roller is then used to fill the upper layer with the fresh powder. After printing is finished, surplus powder on the component may be quickly removed with a compressed air jet or manually, and the powders can then be returned to the chamber for further use. The parts can be placed versatily on top of each other or side by side in the build area, so the cost and time per part are low and it provides an advantage in mass production. However, since the objects are sintered without finish curing, their surface quality is very poor and porous [31].

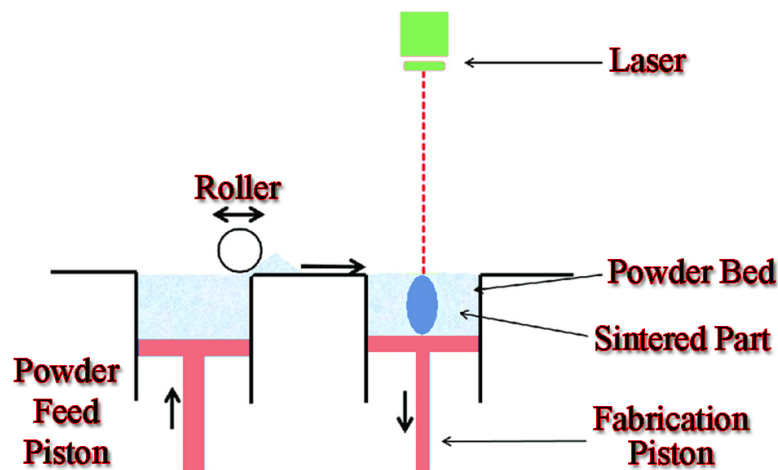


Figure 1.2: Working principles and components of SLS technology

Materials such as polyamide (PA), carbon-filled and aluminum-filled PA, polystyrene (PS), thermoplastic elastomers (TPE), polypropylene (PP), PC, PEEK, stainless steel, cobalt, glasses, and ceramic can be utilized in SLS technology [32]. Since powders should have an average particle size diameter of between 45  $\mu\text{m}$  and 90  $\mu\text{m}$ , it is not possible to employ powders of every material in this procedure [33]. Although the choice of materials varies according to the application, in biomedical applications, materials such as PEEK, polyethylene (PE), Ultra-high-molecular-weight polyethylene (UHMWPE), and Ti6AlV4 alloy are popular due to their biocompatible properties [34]. Especially with the capability of serial production, it comes to the forefront of preoperative planning applications by providing surgeons with experience to facilitate surgery procedures [35]. This improves communication between the patient and the doctor and allows for the simulation of surgery by creating bone models that are suited for the patient's bone morphology. In addition, for complex defects such as craniofacial, tumoral and etc. occurring in any part of the person, custom-made models can be implanted as biocompatible and indistinguishable from the original. Another area of usage is the production of porous 3D scaffolds that provide a suitable environment for tissue regeneration [36]. Conditions such as attachment, interconnectivity, nutrition, and waste change necessary for the life of cells can be performed with high porosity and non-toxic materials.

On the other hand, it's important to consider the drawbacks of SLS technology, such as shrinkage, warping, and powder removal [37]. The high temperature that occurs during printing causes warping and shrinkage on the part. Therefore, the dimensional accuracy of a printed part is approximately  $\pm 0.3\%$  according to an original model [38]. Escape holes are necessary to get the unsintered powder out of the part's enclosed section.

### 1.3.3 Binder Jetting (BJ)

BJ is a printing technology, similar to SLS technology but not requiring heat, in which a binder is used to glue powder particles instead of a laser [39]. The part is produced by selectively joining the powders with the binder sprayed on the layer by the inkjet head. The working principle of the BJ method is shown in Figure 1.3. The inkjet system works by spraying droplets that accumulate and can be refilled in a printing

device. The piston descends when the printing on the upper layer is finished, and rollers are used to sweep the unbound powders to the top layer. Since the build chamber is filled with powder material, support structures are not needed, however, powder escape holes should be in the model design for removing the unsintered powder in enclosed cavities. Escape holes can be single or multiple on a model, but if a single hole is preferred, it should not be less than about 5 mm for easy discharge [40]. On the other hand, if it is desired to be a more reinforced structure, this cavity can be printed with special infill patterns or powder trapped inside without escape holes. However, unlike FDM technology, the software cannot make these patterns automatically, instead, the end-user should draw support patterns on a model. Post-processing in BJ is one of the biggest drawbacks in that it takes a long time and is challenging [39]. Because an air pump is used to remove excess powder remaining on the part, and it must dry to obtain the final part over a specific period of time. In addition, the strength of the part sintered with powder particles may not be sufficient, so the part is immersed in a container full of binder or epoxy and left to dry again. However, the waiting period can be considered reasonable as they usually vary between 1-2 hours [41].

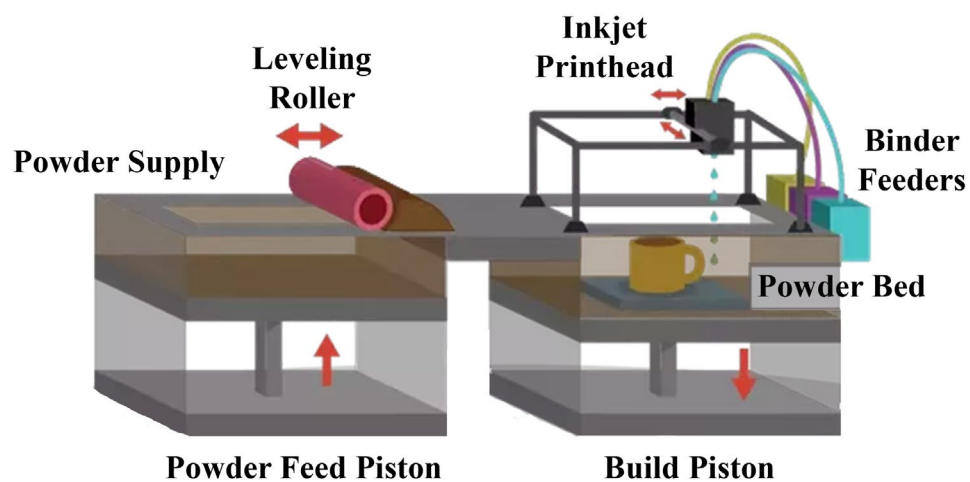


Figure 1.3: Principle of operation for BJ technology

In the BJ method, the powder bed consists of ceramic-based materials. These materials include silicon dioxide ( $\text{SiO}_2$ ), silicon nitride ( $\text{Si}_3\text{N}_4$ ), aluminum oxide ( $\text{Al}_2\text{O}_3$ ), barium titanate ( $\text{BaTiO}_3$ ), silicon carbide ( $\text{SiC}$ ), titanium carbide ( $\text{TiC}$ ), hydroxyapatite (HA), calcium phosphates (CP), sulfate hemihydrate ( $(\text{CaSO}_4)_2\text{H}_2\text{O}$ ) etc [42]. All these powder materials typically have particles between 2 and 200  $\mu\text{m}$  in size [43]. Although strength, density, flowability, particle size, and shape are all different from one another in terms of a material's properties, these ceramic materials have low strength and accuracy. However, there are some ways to overcome this disadvantage. Among these, it is possible to obtain better prints by making necessary improvements in powder, binder, software parameters, printing device, and post-processing [44].

### 1.3.4 Stereolithography (SLA)

These methods make use of resins that are photo-curable and solidify as a result of a photochemical reaction [45]. SLA technology is based on the principle of solidifying certain areas of the photopolymer resin layer by means of a point UV laser source. The resin layer merges with the first layer and the solidifying process continues at particular points determined by a computer in order to produce the part. The build platform lifts upward at a safe distance after a layer is complete [46]. For every layer, these processes are repeated. The entire cross-sectional area of the model is light cured. After all layers are complete, the part is removed from the resin pool. The working principle is shown in Figure 1.4. In this method, photopolymerization is not appropriate for recycling. SLA components cannot be changed back into liquid form. In SLA, the support structure is always necessary. Due to the part's orientation having an effect on the amount of support structure present, placement becomes essential. The support structures must be manually removed after printing because they are printed on the same material as the component [47]. Therefore, it is important to pay attention to not using any support material in areas where the surface quality should be excellent.

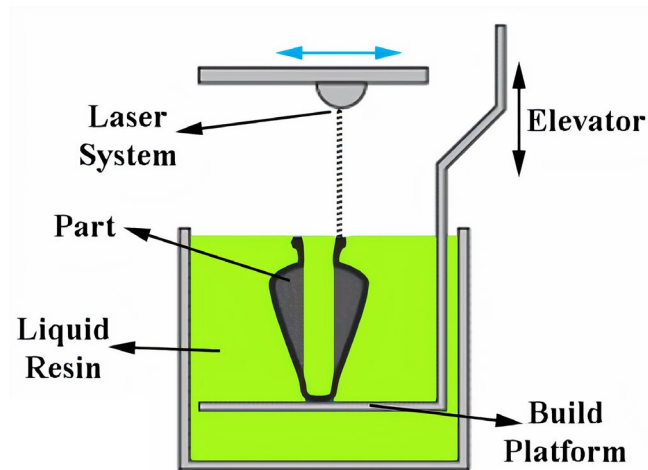


Figure 1.4: Working principle of SLA technology

### 1.3.5 Comparison of Printing Technologies

The utilization of these technologies varies according to the aims, but the factors that are often taken into account include material cost and quality, strength, visual quality, light and chemical reactions, and biocompatibility. Among these, FDM is most commonly encountered because it is a cost-effective technology with both material and device prices [48]. However, it has low accuracy and low surface quality compared to others. Due to its biocompatible filaments, FDM is superior than others in non-complex medical manufacturing. On the other hand, they are not preferred because their success in elaborate anatomical structures is quite low [49]. In these models, BJ and SLA technologies print more successful parts in terms of surface finish. Models produced with SLA have higher strength than BJ. For this reason, it would be better to use SLA where high strength is required. However, there are losses in the level of biofidelity since SLA needs support material. The four different printing technologies are thoroughly compared in Table 1.4, along with technical details.

Table 1.4: Comparison of popular 3D printers commonly encountered in the market [50,51]

	FDM	SLS	BJ	SLA
Material	Filament	Powder	Powder	Liquid
Resolution	100-400 $\mu\text{m}$	20-150 $\mu\text{m}$	10-150 $\mu\text{m}$	25-300 $\mu\text{m}$
Pros	Simple prototyping and efficient	Easy post-processing	High resolution	Highest resolution, accuracy
	Lowest price and Low-cost 3D machines	No Support	Low-cost parts	Low material consumption, reusability of resin
	Usage of all thermoplastic materials	A wide range of materials	No support structures	Usage of transparent, flexible resins
	High strength (20-75 MPa)	Higher part strength	Multiple productions at once	Fast prototyping
	Time-resistant parts	Complex parts in metal	Best for complex parts	Smooth surface finish
Cons	Low details	Porous surface and high shrinkage	Limited range of materials	Fragile resin parts and expensive materials
	Need for support structures	Long time in cooling and heating up	Rough surface, long drying time	Sensitive to sunlight
	Ability to print limited designs	Toxic gas may occur	Difficulty of use	Need for support structures
	Difficulty in temperature control	Expensive	Expensive 3D machines	No time resistance

## 1.4 Creating Artificial Bones

In cases where it is not possible to reach a cadaver, artificial bones are produced with similar properties to real bones, creating an opportunity for many studies [52]. These studies include educational activities, pre-operative planning, implant testing, and other experimental studies. In education studies, it is one of the features that should be similar to real bone in terms of surface and cross-sectional details [53]. In addition, colored artificial models increase students' learning abilities because anatomical features can be easily distinguished. In pre-operative planning, bones should have mechanical properties similar to real bones and be produced in the most consistent to the model obtained from the patient's image [54]. In experimental studies,

standardization and low variability between specimens have great importance in order not to affect the results [55]. For all these purposes, low cost, easy accessibility, and quality are among the desirable. However, creating these bones with properties that can mimic real bones brings a very high cost. Therefore, it is possible to come across the production of artificial bones with different qualities and properties. In order to reduce these costs, 3D printers, which have been commonly used in the medical field in recent years, are making efforts to produce artificial bones. The detailing of commercial and 3D printing artificial bone models is carried out in the following sections.

### 1.4.1 Commercial Composite Bone Models

Bone models are used quite frequently because they provide many benefits to researchers in the field of orthopedic biomechanics. The difficulty of finding cadavers, the need for ethical permissions and the risks of infection have led researchers to artificial bone models [56]. In addition, cadaver bones have negative sides such as high cost and storage trouble, low bone quality due to usually belonging to the elderly, and difficulty in reproducibility of experimental results. However, cadaver bones have been utilized for many years for purposes such as orthopaedic research, medical education, comparison studies of fracture fixation techniques and surgical procedure practice [57]. On the other hand, recently, glass fiber and epoxy mixed bone models were produced by the injection moulding method, and it is possible to obtain a model very similar to the biomechanical characteristics of human bone. On the other hand, through recent advances in material technology, glass fiber and epoxy mixed bone models have been produced by the injection moulding method [57]. Therefore, it is possible to obtain a model very similar to the biomechanical characteristics of human bone. Regarding mechanical properties, its response to bending, axial and torsional loads resemble the results of an ideal natural bone [58].

Four different generations have emerged in the development process of composite bones so far. Although the first-generation models were produced from polyurethane foams and reinforced with epoxy, they are quite weak and have many problems such as delineation which is observed as a kind of failure under compression load. Second-generation bones were manufactured with fiberglass fabric reinforced epoxy using the

pressure injection method [59]. Unlike the previous generation, flexural stiffness results close to natural bone, but there was a manufacturing difficulty in this generation as it required hand-workmanship. In the third-generation, an advanced bone model has been realized compared to the previous generations, with new materials and development in production processes. Instead of handcrafted production, glass fiber-reinforced epoxy is produced around the polyurethane foam according to the injection-molded technique [57]. Therefore, models that are high fidelity to the anatomy of the bone obtained from an adult were constructed. Furthermore, axial and torsional load values were improved according to the second generation. Although the fourth and last generation has the same production technique as the third generation, higher stiffness values have been achieved with the optimized epoxy material.

In today's technology, commercial composite bones indicate results close to characteristics of human bone and provide a standardized sample, however, they have several drawbacks. At the beginning of these, since a particular human bone mold is used, the variety of models is inadequate and it is not possible to manufacture a custom-made model in serial production [60]. They may not overcome biomechanical studies that require a different bone size or shape because they are produced in an average size and geometry. Similarly, they cannot be used for the practice of the surgery or pre-operative planning processes, as models should be similar to the patient's bone anatomy. In addition, high prices per model in advanced commercial bones are now challenging researchers because orthopedic studies require large amounts of samples for reducing the margin of error, making it based on particular assumptions, and providing validity of a study [61].

### 1.4.2 3D Printed Bone Models

A human bone that is complex-shaped and detailed can be printed uncomplicated and cost-effectively with developments in printing technology and filament materials [62]. In addition, the scan images of the patient can be appropriately rebuilt in 3D with fast prototyping and advanced image processing methods. 3DP models in pre-operative planning applications, which have limited time, allow environments where surgeons can practice and have experience. Although these models cannot perfectly mimic natural bone properties, they can be produced in accordance with the patient's bone

geometry [63]. Strength properties according to different 3D printer material types and artificial composite bones are shown in Table 1.5.

Table 1.5: Tensile and compressive properties of natural and artificial bones [59,64–68]

Bone Samples	Tensile Strength	Tensile Elastic Modulus	Compressive Strength	Compressive Elastic Modulus
2nd-Generation	172 Mpa	18.6 Gpa	275 Mpa	14.2 Gpa
3rd-Generation	90 Mpa	12.4 Gpa	120 Mpa	7.6 Gpa
4th-Generation	107 Mpa	16 Gpa	154 Mpa	16.6 Gpa
Cadaver	130 Mpa	17 Gpa	170 Mpa	17 Gpa
3D Printing (Peek)	110 Mpa	3.6 Gpa	118 Mpa	3.8 Gpa
3D Printing (Abs)	45 Mpa	2.2 Gpa	55 Mpa	1.5 Gpa
3D Printing (Pla)	70 Mpa	3.2 Gpa	60 Mpa	1.8 Gpa
3D Printing (Sla Resin)	84 Mpa	3.4 Gpa	72 Mpa	3.4 Gpa
3D Printing (Sls Pa-Aluminum Filled)	48 Mpa	3.8 Gpa	-	-
3D Printing (Metal Ti6al4v)	900 Mpa	110 Gpa	-	-

Depending on the application, the use of different bone materials has advantages and shortcomings relative to each other. According to Table 1.5, the strength characteristics of the fourth-generation composite bones are quite similar to those of the cadaver bone. The first reason is that the production method is more suitable and they are produced with more than one different material. Because a human bone consists of two tissues with different properties, cortical and trabecular. Cortical bone forms the outer surface of a bone that has high stiffness for interior protection, while the trabecular bone which has anisotropic material and a highly porous structure is usually on the inside [69]. On the other hand, 3D printers are challenging to print multiple different materials and many devices are not suitable for this purpose. While the chambers are filled with a single material in SLA and SLS, multiple materials can be used with more than one nozzle feed in the FDM method. However, this is both

time-consuming and increases the possibility for potential disruptions to occur. Furthermore, software instability may result from the structures that will be printed using which materials. Therefore, it requires to make advanced parameter settings of software and fast change of material in the nozzle. Another problem with FDM is that multiple materials need different melting temperatures. Temperature changes on the nozzle can result in increasing printing times due to the fact that it is quite slow. As a result, it is extremely complex to obtain bone printing with more than one material with diverse characteristics in a 3D printer. As considered the Table 1.5, results far from the mechanical properties of natural bone were obtained in 3D printers.

Developing the 3D printing material that can most appropriately represent the mechanical properties of bone still has technical problems [70]. However, there are studies that obtain stiffness and strength close to the mechanical properties of a cortical bone [71]. These significant achievements in material technology will pioneer additive manufacturing technology for creating subject-specific 3D-printed bone. On the other hand, there is no requirement to exactly imitate the mechanical properties of natural bone in applications such as educational studies and pre-operative planning. In such applications, it is a major concern to obtain convenient bone morphology and geometry for fidelity to natural bone. The methods used to construct a comprehensive 3D model that can replicate the morphology of human bone are covered in the next section.

## 1.5 Imaging Modalities

Imaging methods are overutilized by medical practitioners for purposes such as medical diagnoses and determining treatments, obtaining anthropometric data, and performing custom-made production using the information on body shape and size. Because imaging techniques allow for quantitative analysis of the images being evaluated, they increase the ability of medical professionals to reach an objective conclusion quickly [72]. Therefore, it can be diagnosed that is more exact and provided treatments that are calculated and precise with noninvasive imaging techniques [73]. These methods can be classified as radiology, microscopy, photography, graphics and 3D reconstruction. In this study, radiology and 3D reconstruction methods will be discussed. Radiology includes X-ray (2D Radiography), Magnetic resonance imaging (MRI), Computed tomography (CT), Ultrasound, and Positron emission tomography

(PET). Since there is no cross-sectional image in Ultrasound and X-ray unlike MRI and CT, they cannot be obtained in 3D. Among the 3D reconstruction methods, 3D scanning comes to the forefront. With 3D scanning, it is possible to obtain anatomical structures with high-precision measurements.

CT, one of the non-invasive methods, reveals the object's internal details using X-ray tubes [74]. Other components of the system consist of a rotary table, an X-ray detector, and a data processing unit that performs computation, visualization, and data analysis of measurement results. Cross-section images are produced by projecting an item once while transmitting a beam of photons into one plane of the object at certain angles [75]. X-ray rays interact with the object they pass through and reach the detector with attenuation or absorption. The detector and X-ray, which are placed in a rotating ring called a gantry, conduct the transmission and collection of photons passing on the object from every angle. Gray values obtained from the electron density distribution are formed for the scanned object. In order to interpret CT images, the Hounsfield Unit (HU), which is a standard scale in radiology, is used by measuring radio density. It was determined using a linear attenuation coefficient of the X-ray beam and while distilled water is arbitrarily approved as 0 HU, the air is accepted as -1000 HU [76].

## 1.6 3D Reconstruction

The display of 3D models has advanced greatly in recent years. State-of-the-art computer applications that aid in 3D reconstruction and the creation of bio-models increases the feasibility of many analyzes [77]. Images obtained in two-dimensions are required for the formation of these models. Advanced software, whether commercial or free, is needed for the 3D reconstruction of radiological images. Table 1.6 shows the most used popular software. Most of the details listed in the table may be found on the websites of the respective businesses. The stages from an image file to the reconstruction of a 3D model are shown in Figure 1.5. Firstly, the Digital Imaging and Communications in Medicine (DICOM) file is opened and the correct orientation is selected. In the selection of orientation, it is necessary to pay attention to the placement of the sagittal, coronal, and axial planes. Then, the Hounsfield Unit value is determined as the threshold to distinguish the interested tissue. Pixels in this selected value range are brought together to obtain a 3D voxel image. Unwanted pixels may show up in the

image as a result of this operation. Various algorithms with machine learning-based auto-segmentation techniques were developed for removing them. These image-processing algorithms, which are generally encountered in commercial software, make it convenient for the user. In addition, it is included in advanced automatic algorithms that can segment tissues such as teeth, hearts, and bones. Manual segmentation has algorithms such as region-growing and dynamic region-growing, while there are also advanced tools in automated segmentation such as Orthopedics (for hips, knees, and ankles), Cardiovascular (coronary, heart, heart valve, stent, blood pool, muscle tissue), Pulmonary (lungs, airway). These algorithms create a 3D image by combining the pixels determined in each mask. Various defects, which can cause problems in the rendering step, may emerge on the surface of the 3D image. These distortions can be regarded as holes, tunnels, spikes, non-manifold edges, self-intersections, highly creased edges, and non-manifold components. As a result of non-fixing these, the corrupted STL file will cause problems when transferred to other software. Thus, it directly affects the results of the analysis to be used in the printing process or in other environments. Elimination of these problems may require additional software that is quite practical. Software that improves surface quality such as Geomagic Studio and Mesh Doctor have been developed for this purpose [78]. In the final step, the 3D model is exported according to the environment to be used.

Table 1.6: Properties of both commercial and free software for 3D reconstruction  
[79,80]

Software	Cost	Input File Format	Output File Format	Image Segmentation	OS	Radiology Modality	FE Solver
Amira Avizo (Thermo Fisher Scientific, Berlin, Germany)	Non-free	DICOM TIFF BMP JPEG	STL, IGES STEP CATIA5 SURFACE	Deep Learning	Windows Unix MacOS	CT, MRI 3D Microscopy PET SPECT	Mesh Processing
Democratiz 3D (Embodi3D, Washington, USA)	Free	NRRD	STL	Threshold	Online Image Processing	CT, MRI	-
InVesalius 3 (Brazil)	Free	DICOM, TIFF, BMP, JPEG, PNG	STL, JPEG VTK POLYDATA, X3D	Semi-automatic	Windows Linux MacOS	CT, MRI	-
ITK-Snap (USA)	Free	DICOM, Nifti	STL, PNG TIFF JPEG, VTK POLYDATA	Semi-automatic	Windows Linux MacOS	CT, MRI	-
MeVisLab (MeVis Medical Solutions, Bremen, Germany)	Free	DICOM, PNG, JPG, BMP, TIFF	JSON, STL	Live Wire, Fuzzy Connectedness, Threshold, Manual Contours Manual and Semi-automatic	Windows Linux MacOS	CT, MRI	-
MIMICS (Materialize, Leuven, Belgium)	Non-free	DICOM, JPEG, TIFF, BMP	STL STEP IGES	Manual, Fully and Semi-automatic	Windows	CT, MRI	+
OsiriX (Pixmeo SARL, Swiss)	Non-free	DICOM	STL, OBJ VRML RIB, IV	Region Growing, 3D VR Bone Removal	Window MacOS Linux	CT, MRI	-
Real 3D VolviCon (South Korea)	Free	DICOM, VTI, MHD, VOL, RAW	STL, PLY VRML OBJ, IV BMP	Threshold	Windows	CT, MRI	Mesh Processing
Simpleware (Synopsis technology, CA, USA)	Non-free	DICOM, JPEG	STL STEP IGES CATIA	Semi-automated, Manual	Windows Linux	CT, MRI Micro-CT FIB-SEM	ANSYS COMSOL Abaqus NASTRAN LS-DYNA
Pro Surgical 3D (Stratovan, Sacramento, CA, USA)	Free	DICOM, VTK, HDR, NII	STL, PLY	Threshold	Windows	CT, MRI	-
VMTK Lab (Orobix, Bergamo, Italy)	Non-free	DICOM, NRRD, NIFTI, VTK, STL, PVTU	VTP, STL	Colliding Fronts, Fast Marching, Threshold, Isosurface, Active Tubes	Windows MacOS Linux	CT, MRI	Mesh Processing
3D Doctor (Able Software, MA, USA)	Non-free	DICOM, TIFF, GIF, PGM, RAW	STL, DXF IGES, 3DS OBJ VRML PLY, XYZ	Fully and Semi-automatic, Interactive	Windows	CT, MRI PET Microscopy	-
3DSlicer (The Slicer Community)	Free	DICOM	STL, OBJ NRRD	Fully and Semi-automatic	Windows MacOS Linux	CT, MRI US Nuclear Medicine Microscopy	-

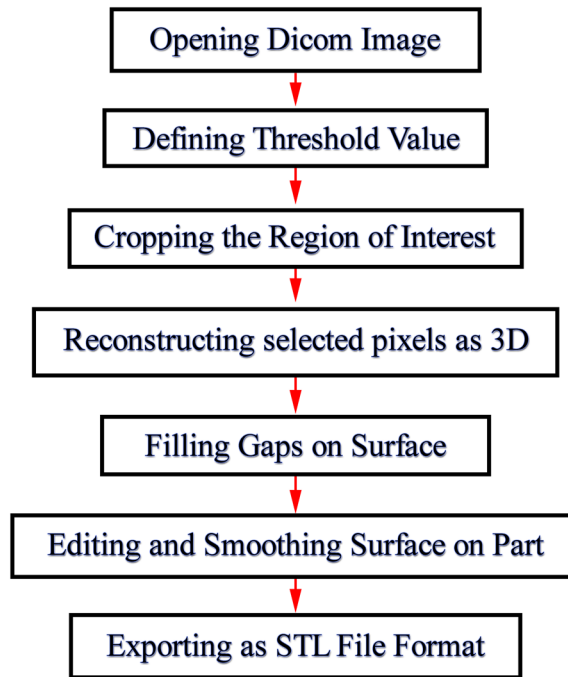


Figure 1.5: The steps to follow for 3D reconstruction up to 3DP

Some of this software is easy to install and interface. However, the flexibility of this software is very low and there are only certain operators. Non-free software is more complicated and allows you to do more processes. The properties of the software have been provided by the websites and have been tried by installing free software.

## 1.7 Mechanical Analysis

The mechanical properties of a material are related to how it responds to an applied load. Materials can also be categorized and described in this way using their mechanical properties. These properties are calculated to determine how materials deform (elongate, compress, bend) or fracture as a function of applied load, time, and environmental conditions. Information about the properties of the material such as strength, ductility, hardness, impact resistance, and fracture toughness are collected through various instruments. Ductility and strength properties such as percent elongation, young modulus or modulus of elasticity, yield point, stress, strain, and deflections are revealed by the tensile test [81]. In tensile testing, real-time measurements of the elongation of the sample are obtained as a specimen is subjected

to a continuously increasing uniaxial tensile force. This test, which is quite simple and widely available, is performed with a loading apparatus produced by companies such as Tinius Olsen (USA), Shimadzu (Japan), ZwickRoell (Germany), and Instron (USA) [82]. The capacity of these devices varies from 0.02 N to 2500 kN (tension and compression), and the test speed is between 0.001 and 1000 mm/min. One of the most important elements of the device is the load cell that performs measurements using transducers based on strain gauges. Even when subjected to static and quasistatic stresses, they have a high measurement accuracy ( $\sim 0.5\%$ ) and little drift. A tensile tester with equipment is shown in Figure 1.6. If there is an auto-calibration of the device, it should be performed before starting the test. Then, the sample is placed and jammed between the grippers in accordance with horizontal and vertical alignment, and the tension that may occur meanwhile should be relieved by fine force adjustment. The extensometer, which is one of the most important pieces of equipment of the device, can compute the extension of a sample under load with its non-contact high measurement accuracy [83]. It performs the measurement by capturing continuous images throughout the test on the sample marked with special markers (detecting the marker on the sample from the color and texture difference in the image). Acquired data can be calculated and reported by the software of the device and graphics such as stress-strain curves can be exported in many files format. Tensile, compression, 3- or 4-point bending (flexural testing), peel, and tear tests can all be carried out using a tensile tester, also known as a universal testing machine, in either a single or cycle configuration.

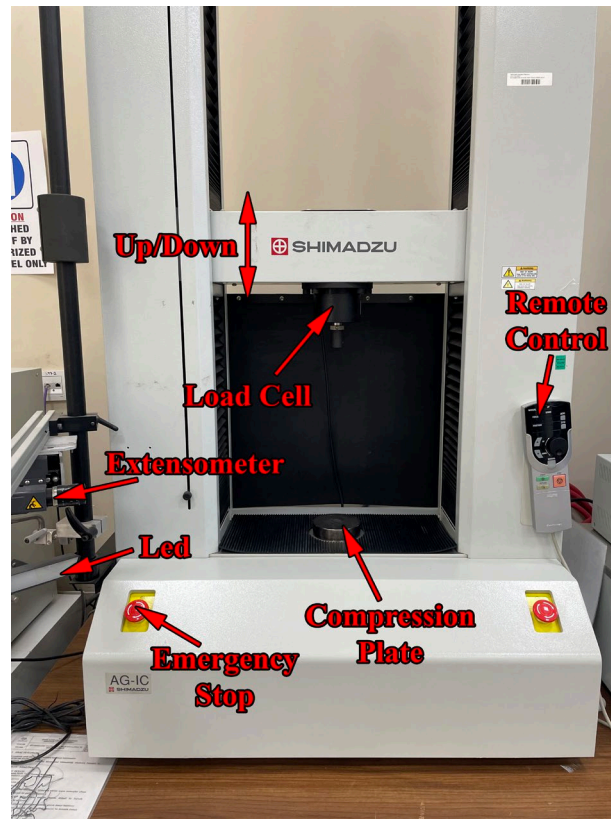


Figure 1.6: Components of the tensile tester

Five different states of force application can be observed on an object; tensile, compression, bending, shearing, and torsion. As a result of this loading, material-specific properties can be obtained using appropriate test devices. These interactions in a sample create two important variables: stress and strain. Stress can be described as the ratio of the perpendicular force applied to a sample divided by its initial cross-sectional area (Eqn. 1.1) [84]. In other words, it is the internal distribution of forces in it that compensates the loads applied to it and as a result of a reaction to them. The applied force can be uniformly distributed on the object, or on the contrary, it can be applied at loads applied from a specific point whose intensity decreases as the distance increases. A system's reaction to an applied stress is called “strain”. Strain is the proportion of the length change caused by deformation to the specimen's initial length (Eqn. 1.2) [84]. As a result, the number becomes unitless. Stress on the vertical axis and strain on the horizontal axis are combined to form a single graphic stress/strain curve. Data on Young's modulus, elongation, area reduction, tensile strength, yield point, and strength may all be accessed using this graph. The relationship between

stress and strain initially increases linearly in the tensile test, then reaches the yield point. This is called the linear-elastic part of the curve and indicates that no plastic deformation has occurred. In the elastic region, the material will return to its original shape when the load on the object is removed. The slope of the curve in this region is calculated and provides the elastic or Young's modulus properties characteristic for each material (Eqn. 1.3). It indicates a measure of the stiffness of a particular material. The region after the yield point is called “plastic” and permanent deformation has occurred on the specimen. After this point, even if the load is removed, the specimen will not return to its original, unstressed status. This point, known as yield strength, is specified as the stress needed to create a plastic deformation [85]. At the same time, axial strain creates lateral stresses that are opposite and equivalent to each other in two directions perpendicularly. These stresses cause strain on the specimen to lengthen vertically and shorten horizontally. This ratio, known as Poisson's ratio, is calculated by dividing lateral strain by axial strain for a uniaxial stress condition (Eqn. 1.4). This value, which is a characteristic feature of each material, varies between 0 and 0.5 according to the material [86]. The formulas for all the tensile properties mentioned above are given in Table 1.7.

However, there are two different approaches: engineering and true stress/strain. There is a shift in cross-sectional area as the material starts to neck against the applied force. However, in engineering stress, this time-dependent change in area is neglected and the stress is calculated according to the initial area. On the other hand, true stress is found to be higher than engineering stress since it is obtained by dividing the force by the cross-sectional area that decreases with time (Eqn. 1.5). Similarly, true strain is obtained at a lower rate than engineering strain because the change in length will be proportional to the current length instead of the initial length (Eqn. 1.6) [87]. However, since the difference between true and engineering stress/strain is quite low in the elastic region, this difference is negligible. Conversely, the difference in the plastic region tends to increase.

Another important property of materials is ductility, the ability of a material to maintain a great permanent deformation under loading until the point of fracture or plastically deformed without failure [88]. Ductility can be computed as two variables: reduction of area or percent maximum elongation. Reduction of area is described as

proportion of the difference between the initial and final cross-sectional areas at failure to the initial cross-sectional area (Eqn. 1.7). Elongation, which indicates how much a sample flexes or elongates during tensile testing, is the ratio of the difference between the initial and final lengths to the initial length (Eqn. 1.8).

Table 1.7: The following formulas are calculated from the data obtained using tensile testing

Engineering Stress	$\sigma = \frac{F}{A_0}$ (1.1)	Engineering Strain	$\epsilon = \frac{L-L_0}{L_0}$ (1.2)
Young's Modulus	$E = \frac{\sigma}{\epsilon}$ (1.3)	Poisson's ratio	$\nu = -\frac{\epsilon_{lateral}}{\epsilon_{axial}}$ (1.4)
True Stress	$\sigma_T = \sigma_e(1 + \epsilon_e)$ (1.5)	True Strain	$\epsilon_T = \ln(1 + \epsilon_e)$ (1.6)
% Reduction of area	$\frac{A_0-A}{A_0} \times 100$ (1.7)	% Elongation	$\frac{L-L_0}{L_0} \times 100$ (1.8)

## 1.8 Finite Element Method

The finite element method (FEM) was first stated by Clough in the 1960s. Since then, studies on this subject have increased exponentially; thus, there is an innumerable number of books, studies, and research available today, and it is still becoming more and more popular [89]. The sequence of processes is as follows: physical model, mathematical model, numerical model and computer model [90]. In order to apply this method, it is necessary to produce mathematical formulations of physical phenomena and to perform numerical analyses of these models. In the final step, the physical system is simulated by developing computer codes. For all these stages, processes such as the laws of physics, linear or nonlinear algebraic equations, differential equations, derivations, matrix organization, assumptions, estimations, and calculation tools follow each other. Since many problems are complicated to solve in this laborious process, they can be obtained as approximate solutions or by simplifying them.

FEM is defined as a discretization of complex geometric shapes into a set of finite elements (FE) [91]. FEM generates structures called nodes and elements, also called the meshing process, using advanced algorithms. This method is possible to use in many fields of physics such as static, dynamic, thermal, flow, electromagnetic, and acoustic. In all problem types, analysis steps are similar to each other, followed by creating the model, determining the material properties, defining the boundary conditions, and solving the problem. Table 1.8 is a list of the most widely used FE programs available today.

Table 1.8: Commonly available FE software in the market [92]

Free	Elmer FEM solver ( <i>Center for Science, Espoo, Finland</i> ) FEBio ( <i>The University of Utah, UT, USA</i> ) FEATool Multiphysics ( <i>Precise Simulation Ltd., Wan Chai, Hong Kong</i> ) Hermes ( <i>hp-FEM Group, USA and Czech Republic</i> ) MFEM ( <i>MFEM team, Livermore, CA, USA</i> ) Range Software ( <i>developer by Tomoltys</i> )
Commercial	ANSYS ( <i>Workbench, PA, USA</i> ) Abaqus ( <i>Dassault Systemes, Valizy-Villacoublay, France</i> ) Comsol Multiphysics ( <i>COMSOL Inc., MA, USA</i> ) ADINA ( <i>ADINA R &amp; D Inc., Watertown, MA, USA</i> ) Nast ( <i>MSC Software, CA, USA</i> ) Autodesk Simulation ( <i>Autodesk, CA, USA</i> )

In order to perform finite element analysis (FEA) correctly, the accuracy of the inputs to the system is significant. Thus, the material properties must be accurately entered into the system. In the studies, material properties are considered as Young Modulus, Poisson ratio, and density. There are several different ways of obtaining Young's Modulus and assigning material properties. Material properties are obtained by compression-tensile tests and can be given as input to the system. In another method, the Young Modulus can be calculated using the data obtained from CT [93]. Hounsfield Unit values of pixels are converted to physical density values by using previously calculated equations. Then, physical density values are converted into apparent density to obtain Young Modulus. Young modulus can be assigned as

isotropic, anisotropic or orthotropic. The most realistic results are orthotopically assigned, but it is difficult to give input to the system [94].

Recently, with the rapid development of technology, both the hardware and software features of computers have improved. It is very difficult to follow the latest technological systems during this period. However, due to these developments, auxiliary systems for doctors increased the success of the surgeons and reduced the possibility of revision. As a result, it was possible for the patient to be treated at a lower cost and suffer less pain. With the individual analysis of the implants to be used, long-lasting and successful surgeries can be performed without revision. In this study, information about which steps should be taken for finite element analysis of implant or bone fractures and which tools should be used is brought together for static analysis. Depending on the analysis to be performed, the software that needs to be selected and their differences are mentioned in this paper.

## Chapter 2

# Finite Element Analysis in Orthodontics

Many analyses involving teeth and bones in the human body have been carried out up to the present for purposes such as diagnosing diseases, learning the mechanism of fractures, determining the strength of implants or prostheses, and trying new treatment methods. Among these studies, the areas where fractures such as hip, knee, elbow, and spine have most commonly come to the fore. On the other hand, FEA is frequently encountered in the fields of orthodontics and dental surgery in applications such as implant analysis, dental implant designs, and temporary anchorage devices. This chapter focused on dental applications of finite element analysis.

Undesirable tooth movement, also known as anchorage control, is one of the important factors affecting the outcome of orthodontic treatment. Anchorage in traditional orthodontics can be placed in various anatomical regions such as teeth or tooth groups, opposing tooth arch, palate and palatal mucosa, parietal and occipital regions of the head, nape, jaw tip, and muscles around the mouth. During orthodontic treatment, when a force is applied to a tooth or tooth group in accordance with Newton's action-reaction principle, a force or moment of the same magnitude but opposite direction occurs [95]. In traditional orthodontic treatment, a large number of extraoral appliances such as “headgear” and various intraoral appliances have been designed to provide anchorage control [96,97]. However, patient cooperation is required for the use of these appliances, which often leads to loss of anchorage despite the use of appliances [96,98].

Miniscrews are commonly entitled to temporary anchorage devices (TADs). Recently, miniscrews, which do not require patient compliance, have been used by researchers as absolute anchoring devices in orthodontic treatment [99,100]. Besides, in the literature, very successful treatment results have been documented using miniscrews

for orthodontic anchorage in various malocclusions [101,102]. The recovery period is faster than traditional methods; in addition, surgical procedures are easy, and application is simpler. Undesired tooth movements are prevented because force is not applied directly to the teeth. Finally, increased patient comfort, minimized risk of infection and inexpensive material and application costs combine with the above points to demonstrate the many advantages of using miniscrews [103]. On the other hand, some complications may be encountered during treatment, such as fracture during insertion, removal of the miniscrew, penetration into the sinus cavities, risk of inflammation, embedding, pain, bleeding, and allergic reactions [104]. Overall, further study is required to clarify the consequences of miniscrews, which are already widely used [105].

The stability of the miniscrew and the success of treatment are directly related to the properties of the specific type of miniscrew used [106]. The success rate in miniscrew applications has been reported to be relatively high in the literature. According to a 2011 study, a high success rate of 87.7% was reported in miniscrew application [107]. In another study, the overall failure rate of miniscrew implants was determined to be 14%; this percentage is thought to be highly acceptable and supports the efficacy of the devices in clinical practice [108]. Additionally, a 93% success rate following miniscrew insertion led researchers to the conclusion that the device's initial stability was significantly influenced by the insertion site and clinical expertise [109]. Also, miniscrew design, bone quality, the region where the implant is inserted, placement method and angulation, loading duration, and closeness to the tooth roots were also observed to impact the stability of miniscrews [110]. Recently, Kuroda et al. demonstrated that root proximity is a significant contributor to miniscrew failure [111]. Miniscrews can be made smaller to minimize root contact, however doing so fails because shorter screws are unable to endure the stresses associated with orthodontic treatment. Therefore, it is vital to develop an ideal design for the smallest miniscrew sizes that can bear the orthodontic load and to investigate the relationship between the orthodontic load and the miniscrew's stress distribution.

Furthermore, primary stability heavily depends on miniscrew designs [112]. These properties comprise material, length, thread dimensions and shapes, pitch width and depth, outer-inner diameter, neck length, shape, tip, and head design [113–115]. The

many defining features of commercially available miniscrews are shown in Table 2.1. Optimal properties should be selected to provide adequate retention, prevent bone loss, and enhance osseointegration. Figure 2.1 illustrates a generic representation of the geometric characteristics of miniscrews. Manufacturers of miniscrews believe their products perform better because they have unique geometric features. Nevertheless, each of these characteristics may result in varying levels of force needed, differences in adhesive strength, and stress distributions in the bone tissue. On the other hand, it is challenging to investigate such characteristics using empirical research since it requires specialized knowledge and takes a lot of time. To simulate and analyze the aforementioned issues, computational mechanics methods have been constructed.

Table 2.1: General characteristics and dimensions of miniscrews available in the market (Dimensions may vary according to different brands) [116,117]

Miniscrew Properties	Description and Dimensions
Form	Tapered, Cylindrical
Lengths	From 4 mm to 15 mm
Collar Lengths	From 1 mm to 3 mm
Thread shapes	Square, V-Shaped, Buttress, Reverse Buttress (Symmetrically, Asymmetrically)
Thread angle	From 120° to 150°
Pitch width	From 0.4 mm to 1 mm
Pitch depth	From 0.1 mm to 0.5 mm
Flank	From 250 μm to 400 μm
Inner (Minor) Diameter	From 1 mm to 2.5 mm
Outer (Major) Diameter	From 1.1 mm to 2.5 mm
Apical Phase Angle	From 55° to 58°
Tip Design	Self-Drilling, Self-Tapping
Head Design	Bracket Head, Button Head, Through-Hole Head, Mushroom-shaped Head, Cross Head, Circle Head
Neck	From 1 mm to 1.6 mm
Materials	Titanium Alloy (TiA), Stainless Steel (SS)

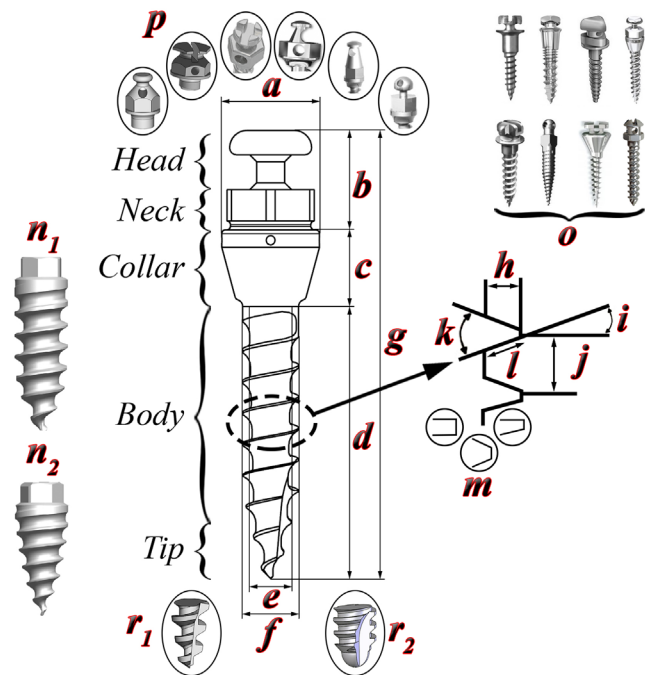


Figure 2.1: Schematic representation of geometry properties of miniscrew ((a) Head diameter, (b) head length, (c) collar length, (d) body length, (e) inner diameter, (f) outer diameter, (g) length of screw, (h) pitch depth, (i) apical phase angle, (j) pitch width, (k) thread angle, (l) flank, (m) thread shapes, (n<sub>1</sub>) cylindrical miniscrew, (n<sub>2</sub>) tapered miniscrew, (r<sub>1</sub>) self-drilling, (r<sub>2</sub>) self-tapping, (p) different types of head designs, and (o) miniscrews manufactured with different designed types)

[116,118,119]

The selection of the appropriate size for a miniscrew depends on the amount of alveolar bone in the area in which it is to be inserted, the gingival thickness, and the length of the screw head. Miniscrews ranging in length from 6 to 10 mm are inserted into special locations in applications, for example, an up to 6 mm long miniscrew in the mandible, an 8 mm long miniscrew in the mandible or maxilla, and a 10 mm long one in the maxillary or mandibular retromolar region [120]. Studies have shown that the diameter and length of the miniscrew are directly linked to its stability, so it is important to pay attention to screw selection [121]. Additionally, miniscrews have many application placements. The spaces in the alveolar bone between the tooth roots are the most crucial use areas.

In previous studies, the FEA of the miniscrew was generally carried out by simplifying the bone structure. The cortical and cancellous bone structure was designed as a cube, a miniscrew was inserted, and different properties were compared. Yushan et al. investigated the thread depth and thread pitch of miniscrews on a bone block [122], simulating seven different models by changing the thread depth and pitch. They determined the most appropriate thread sizes according to the stress and displacement values for developing a new type of miniscrew. In another comprehensive study, the properties of miniscrews placed in the bone block, including cortex thickness, force direction and the size, length and diameter of the miniscrew were analyzed [123]. Although there is FEA research evaluating the different properties of the miniscrew, the comparison of miniscrew head designs remains unclear. Therefore, in the present study, different head designs on the bone block were created in accordance with the original dimensions and compared using FEA.

FEM was used in various studies to compare the different characteristics of miniscrews in order to determine the optimal anchoring technique. One of them, Perillo et al., used a miniscrew at angles ranging from 30° to 150° with 30° increments to simulate the mandible on a simpler bone block [124]. From their simulation, they conclude that inserting at a 90° angle results in the least stress on the cortical bone. Only the miniscrew's positioning angles and force direction were altered during the investigation. Additionally, miniscrew length and insertion angles were investigated in another study that assumed the mandibular and maxillary bones to be a bone block [125]. Similar to the previous study, they deduced that placing the miniscrew at a 90° angulation caused the least stress concentration in the bone. Ammar et al. placed the miniscrew on the mandibular in treatment planning for orthodontic tooth movement and analyzed stress distributions by simulating the retraction of a single-rooted mandibular canine [126]. They demonstrated that the miniscrew placement between the roots can be predicted virtually and the optimal treatment planning can be chosen under FE loading scenarios for optimizing miniscrew anchorage stability and minimizing patient risk. In another study, Fattahi et al. calculated the effects of different thread shapes and force directions of miniscrew on stress distributions for cortical and cancellous bones [127]. While no relationship could be attained with thread shapes, the applied force directions on the head of the miniscrew affected the stress results and the lowest stress was obtained at the 90° angulation. Unlike other

studies, Liu et al. also investigated the effects of miniscrew on bone quality [128]. In addition, parameters of cortical thickness, cancellous bone density, force direction and magnitude, miniscrew, and exposed lengths were compared in detail using FEA for orthodontic anchorage. According to the simulation results, they concluded that the quality of cancellous bone for miniscrew stability is not very critical. Another important result of the study should be carefully analyzed the implant location and the orientation of the miniscrew in terms of reducing the failure rate. Considering all these studies, miniscrew studies were carried out from different viewpoints. However, in these studies, the models were simplified and performed on a bone block representing the bone. Therefore, there is uncertainty about the effects that the miniscrew may have on a model of the real mandibular bone and on the surrounding tissues. In this study, patient-specific mandibular bone was modeled using medical 3D image-based engineering software, and the effects of force direction applied at a head of miniscrews were investigated in different scenarios. In addition, the effects of miniscrew length and diameter at different sizes on cortical and trabecular structures were calculated using FEA.

# Chapter 3

## Materials & Methods

In this section, firstly, the finite element analysis method for femur fractures was mentioned. In the following section, the methods used in orthodontics were given elaborately.

### 3.1 Analysis of Femoral Head Fractures

The general workflow is as follows; (i) acquiring a 3D medical image, (ii) printing a 3D model, (iii) analyzing the model using finite element analysis, and (iv) correcting the 3D model of the image.

#### 3.1.1 3D Image Reconstruction

The lower abdomen of a 24-year-old male person was CT scanned (Sensation 64, Siemens, Erlangen, Germany) in the DICOM format. A CT image data was obtained with the ethical permission of the Izmir Katip Celebi University's Education and Research Hospital. The individual had no history of bone illness, according to their medical records. The scan images were acquired with a slice thickness of 1 mm, voltage of 120 kV, a pixel size of 512x512, and a pixel spacing of 0.6426. To distinguish between hard tissues and soft tissues, the lower abdomen was segmented using MIMICS (v17.0, Materialize, Leuven, Belgium) software. MIMICS is favored because it has a wide range of 3D image editing tools and strong radiological image processing capabilities. In the segmentation procedure, threshold and region-growing algorithms were utilized. The HU of the image, which varied from 0 to 1680, was set at 661 as the threshold value. When there is little to no space between soft and hard tissues or between the pelvis and the femoral head on the acetabular surface, the

region-growing algorithm may occasionally not work as intended. For this reason, in the CT scan slices, the pixels adjacent to each other in the reference planes and incorrect pixels in each slice were cleaned manually using a multiple slice editing procedure. Figure 3.1a displays a three-dimensional image of the lower abdomen (separated from the soft tissue). In Figures 3.1b and 3.1c, femoral heads, separated from the lower abdomen are shown. As shown in Figures 3.1a, 3.1b, and 3.1c, gaps or undesirable roughness might occur in the 3D image. Using the 3-Matic software (v9.0, Materialize, Leuven, Belgium), the smoothing and wrapping operators were utilized to eliminate unwanted artifacts. Figures 3.1d and 3.1e show the images after these operations with 3D models of the proper patient-specific femoral heads. In the final stage, the 3D image was converted to STL format to be imported into the printer software.

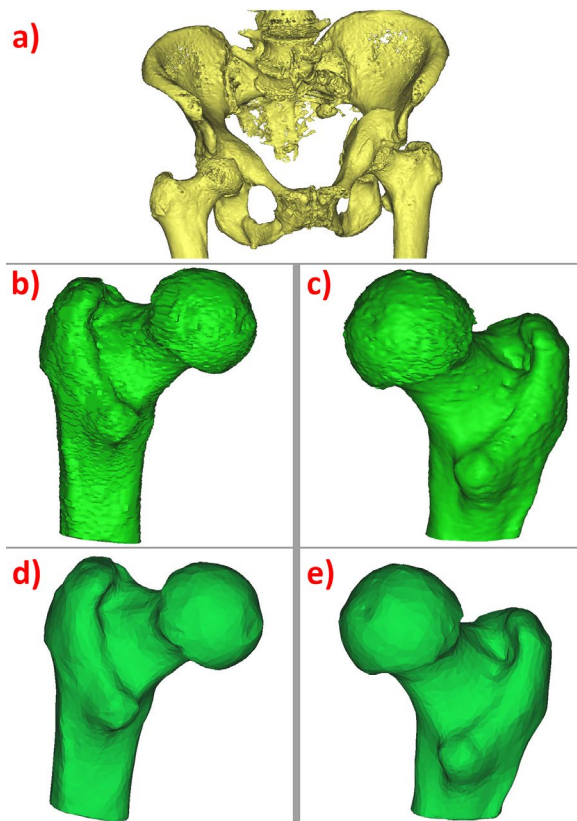


Figure 3.1: (a) The 3D image of the lower abdomen removed from soft tissue, (b-c) The left and right femoral heads' respective 3D models, (d-e) After editing operations, the 3D model of the left and right femoral heads

### 3.1.2 3D Printing of Models

The models were loaded into the printer build area of the 3DPrint program (v1.01, 3D Systems, South Carolina, USA) using the STL file. An SLS-style printer is the ProJet160 from 3D Systems in South Carolina, USA. SLS-type printers were chosen because they do not require support structures to print components with smooth surface finishing and fine detail. The material of the printer is a powder, composed of calcium sulfate hemihydrate ( $(CaSO_4)_2H_2O$ ). In order to increase the adhesion of the powder particles and avoid cracking, the binder was applied to the powder particles after printing. The drying process took two hours to be completed. Figure 3.2 depicts the printed femoral head after all these procedures have been finished. Three test specimens were printed on the same printer in order to determine the material properties. The following printing settings were used to print these parts: 0.1016 mm layer thickness, 3 hours and 15 minutes build time, 111.9 ml of binder volume, with the total volume of parts  $314.87\text{ cm}^3$ , and total surface area of  $9489.18\text{ cm}^2$ .



Figure 3.2: Femoral head models printed with BJ technology

The dimensions of the right and left femoral heads are shown in Figure 3.3. Accordingly,  $B_L$  and  $B_R$  stand for left-right femoral head length (FHL) while  $A_L$  and  $A_R$  stand for the measurement of the vertical diameter of the head (VDH) of the femur. The left VDH was determined to be 46.26 mm and the right VDH to be 45.47 mm. The measured FHL distances for the left and right were found to be 117.91 mm and 100.27 mm, respectively. There is a little discrepancy between the right and left FHL because of the field of view (FOV) of the CT image that was received from the patient. However, instead of comparing the right and left sides, we try to examine each structure independently.

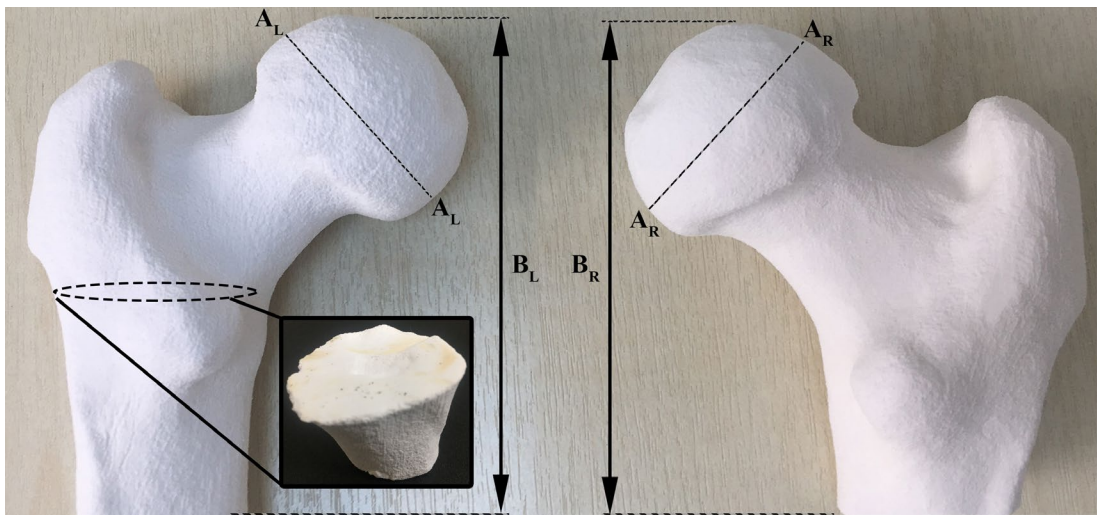


Figure 3.3: The representative measurements of left and right models, as well as the cross-section area of the left femur

For cylindrical specimens, printing parameters were as follows: 15 minutes of printing time, 14.7 ml of binder usage, 24.61 cm<sup>3</sup> of total volume, 189.26 cm<sup>2</sup> of total surface area with 0.1016 mm layer thickness. The parts were hardened using around 30 g of ColorBond (Allomethadione (C<sub>7</sub>H<sub>9</sub>NO<sub>3</sub>), 3D Systems, Inc., Rock Hill, SC, USA) glue once the drying process was complete, and they were then allowed to cure for one day.

### 3.1.3 Compression Testing of Specimens

The cylindrical specimen for the compression test was manufactured in compliance with ISO 5833. SolidWorks (v.2016, SolidWorks Corp., MA, USA), CAD software was used to create drawings of the specimens, which had a total length of 12 mm and a diameter of 6 mm. Compression tests were carried out at a speed of 1 mm/min since the powder material (calcium sulfate hemihydrate) is based on ceramic (Figure 3.4). Due to the fact that the components were made using SLS, they have low strengths. Therefore, to precisely quantify the rupture and load distributions, the load cell with a capacity of 500 N was used. It took approximately  $29\pm 3$  seconds to complete the compression tests. The test findings obtained for use in the finite element analysis demonstrate that the test specimen was fractured at the upper stem of the neck area. The powder material's elastic modulus was determined to be 347.43 MPa. The Poisson ratio was used as 0,19 according to previous studies for FEA [129].

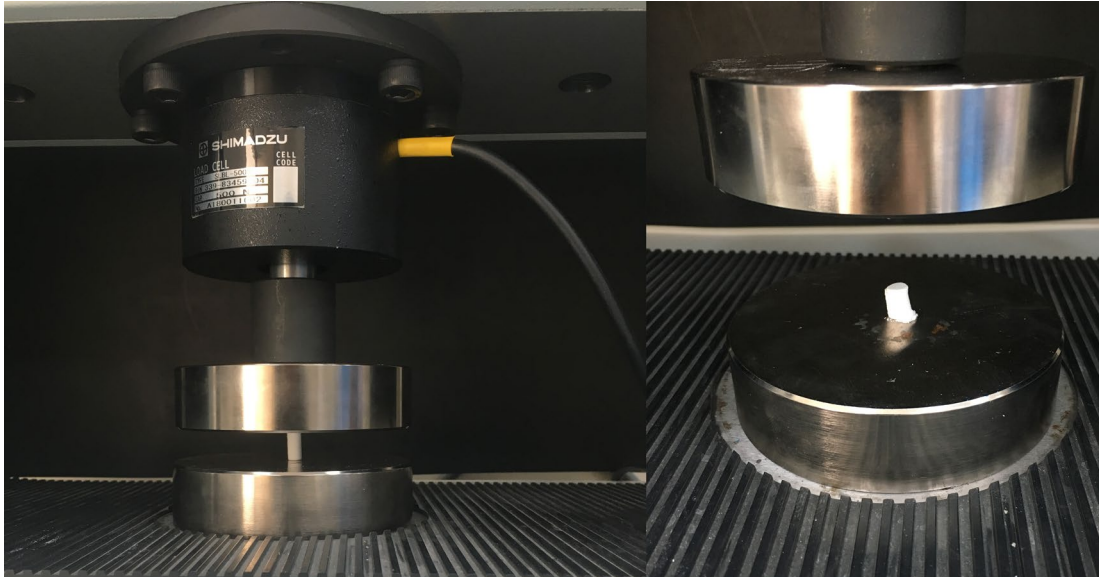


Figure 3.4: The placement of the cylindrical specimen between the compression plates and deformation of the specimen at the end of the compression test

In a calibrated, authorized biomechanics facility, compression tests were carried out using a Shimadzu AG-IC static tester (Shimadzu Corp., Kyoto, Japan). The femoral shaft was fixed to the bottom gripper of the device (Figure 3.5a). Until the fracture was observed, both models were compressed using a 500 N load cell at a speed of 1 mm/min. The models were positioned on the test machine vertically with an inclination of 20° of valgus. Figures 3.5c and 3.5d depict the cracking route and the implementation of the compression test. As a consequence of the test, the failure loads for the left and right femur specimens, respectively, were determined to be 252.67 N and 351.92 N. We assessed each model independently, but the disparities in the outcomes are caused by variations in size, geometry, and moment arms.

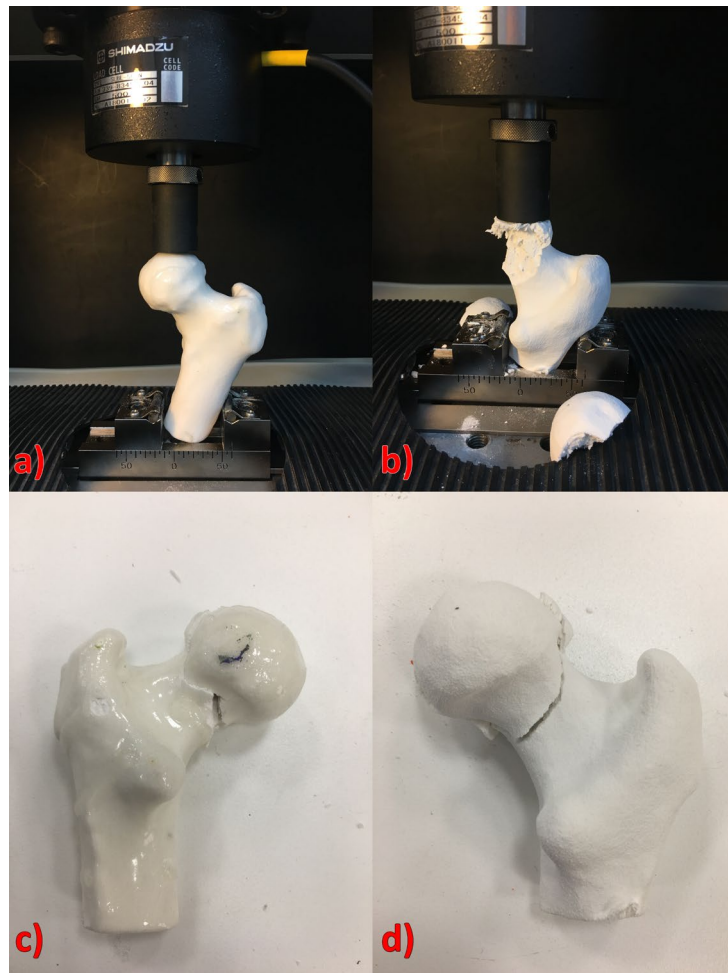


Figure 3.5: (a) The left femur placed on the grippers of the Shimadzu universal testing machine, (b) Failure of the specimen as a result of testing, (c-d) Fracture path after applying load in the left model and the right model, respectively

### 3.1.4 Mechanical Simulation

For analysis, models were exported. The study was carried out as a static structure using the finite element software ANSYS (v16.1, Workbench, PA, USA). According to the outcomes of the mechanical tests, the material properties of the model were classified as isotropic. Ten node-tetrahedral meshing was performed and it was calculated 217673 nodes and 126940 elements for the left femur model, 190714 nodes, and 111097 elements for the right femur model. In ANSYS, a mesh convergence study was carried out. The mesh was therefore modeled with elements with sizes of 1.5 mm, 2 mm, 2.5 mm, and 3 mm. Mesh sizes more than 3 mm were not taken into account because the findings were 48% bigger than the calculated value. Additionally, there was only a 4.3% difference between the stress measurements produced by the 1.5 mm, 2 mm, and 2.5 mm edge length meshes. As a result, a mesh size with an average edge length of 2.5 mm was determined to be appropriate. The mesh image is shown in Figures 3.6a and 3.6b. The fixed support on the femoral shaft was chosen as the boundary condition. In accordance with the findings of the compression test performed using femur samples, loading was applied to the superior of the femoral head. Failure load results of the experimental measurements are shown in the Figures 3.6c and 3.6d, they were found to be 252.67 N, 351.92 N for the left femur and the right femur, respectively. After all inputs were completed, stress distribution, maximum von Mises stress, and strain values were calculated in ANSYS.

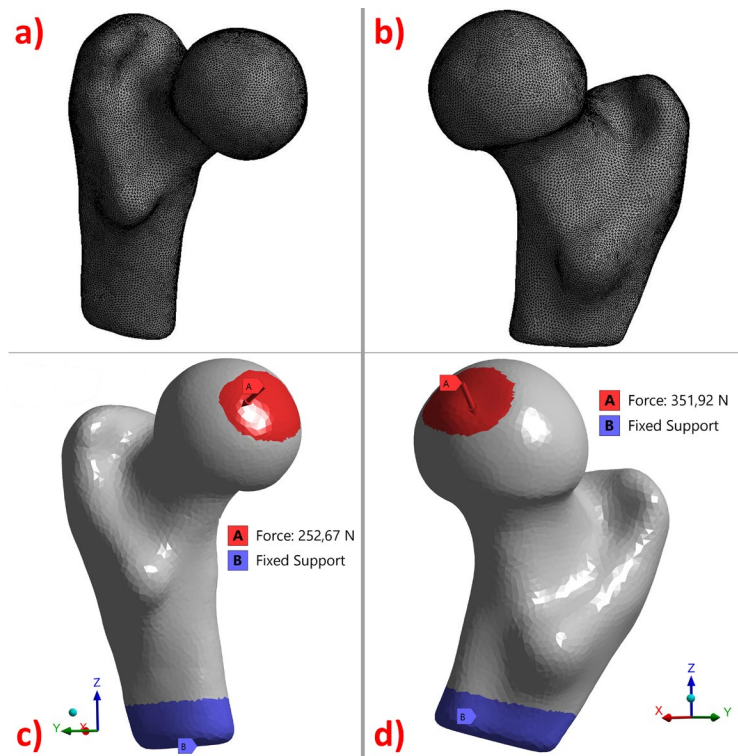


Figure 3.6: The meshing of (a) the left model, (b) the right model, (c-d) The direction of the force and fixed support points on the left model and right model, respectively

The Pearson correlation coefficient ( $r$ ) was calculated to compare the simulation and experimental data statistically. In statistics, the strength of the linear relationship between two different variables is assessed by the Pearson correlation. While this coefficient can be between -1 and 1, 0 indicates that there is no correlation. If the results are close to 1, it means there is a positive correlation between the two variables, whereas a result of -1 means there is a negative correlation [130].

### 3.2 Biomechanical studies in composite bones

In this section, instead of bone samples obtained from a 3D printer, studies on composite bones were mentioned. Thus, the differences between 3D-printed bone samples and commercial bone samples were determined more clearly.

### 3.2.1 Preparation of specimens and the test environment

We concentrated on medial malleolar fractures in contrast to the prior femur analysis since we have available tibia composite bone samples. Fourteen identical synthetic third-generation composite polyurethane bone models of the right distal tibia were obtained. The same fracture line was achieved with a custom-made osteotomy guide in all bone models. A medial malleolus 3.5 mm compression plate and tubular plate were inserted into bone models. The biomechanical testing was conducted to determine the difference between both plates using Shimadzu AG-IC static tester (Figure 3.7). The force/displacement curve and the load-to-failure were calculated. The load cell in the test device measures the reaction to the force that occurs as a result of the displacement change on the sample over time. In addition, many properties related to the material can be obtained from the force-displacement graph. Moreover, the load-to-failure can be described as the point where the material reaches the end point of deformation under the force or breakage occur. In this study, the failure point was acknowledged as a 2 mm displacement from the test's starting position. It was defined as a 1 mm/min testing speed in Shimadzu and forces against 0.5 mm, 1 mm, 1.5 mm, and 2 mm displacement values were recorded. The reason for choosing these values is to increase the number of samples in order to analyze the data statistically. Since it is generally assumed to fail after about 2 mm of displacement in studies, the displacement after this value was not calculated. In addition, it was determined that the force on the samples began to decrease as a result of a 2 mm displacement.

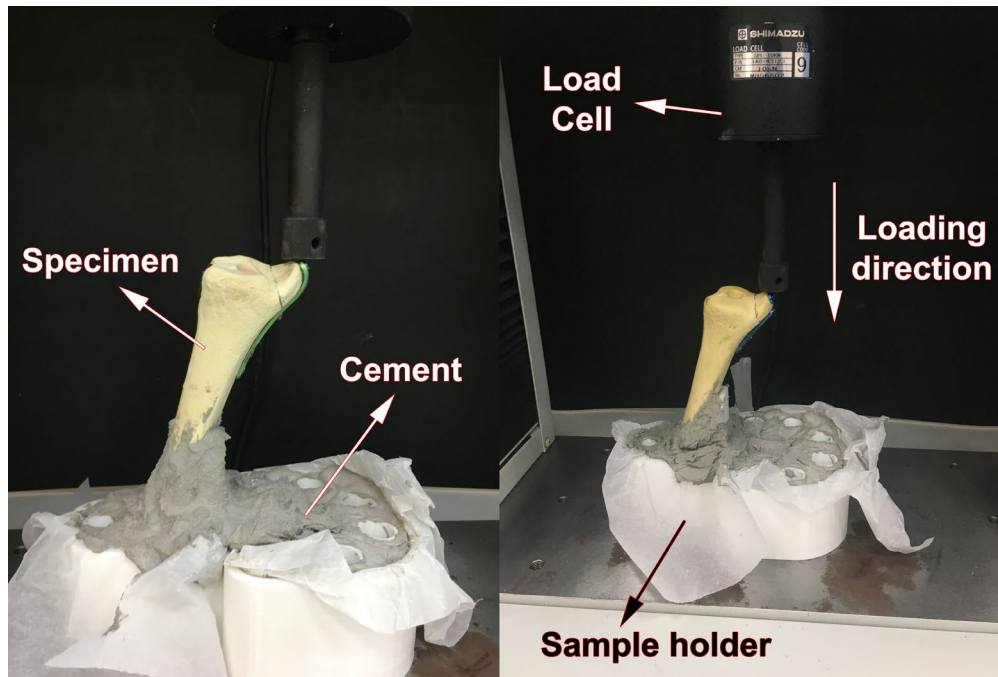


Figure 3.7: Tibia bone preparation and installation of gripper apparatus for testing

On the other hand, since the test device did not have the necessary equipment to grip the bone models, a gripper was designed compatible with the device. As a result, several issues were encountered during the construction of grippers, and various solutions were created to address these issues.

### 3.2.2 Design of gripper for static tester and solutions to the problems encountered

Although the static tester has the equipment to test many different samples, it does not have the necessary tools for special samples. However, the versatility of the fixing points of the device provides a suitable environment for many designs (Figure 3.8a). Instead of employing metal-based components at this point, the grippers were created using a 3D printer. The gripper was drawn using SolidWorks software as shown in Figures 3.8b and 3.8c. In the design, it is ensured that the test device is compatible with the screwing places and has high durability in order not to undergo any deformation during the test. This apparatus consists of fixing points, cementing, and a slider mechanism, as shown in Figure 3.8d. Cylindrical hollow pipes were produced for easy removal of screws during cementation. In order to apply the force exactly to

the desired points, a sliding mechanism is designed on the gripper that can move the bone horizontally. In addition, an inclination ramp was designed to load the bone at an appropriate angle (Figure 3.8e). In this study, the tilt angle was determined as 17 degrees based on previous studies [131]. The part was exported as STL and transferred to Simplify3D (v.4.0, Cincinnati, OH, US) software. They were manufactured with polylactic acid (PLA) material at 100% infill using the Ultimaker (Ultimaker 2 Extended +, Ultimaker B.V., Utrecht, Netherlands).

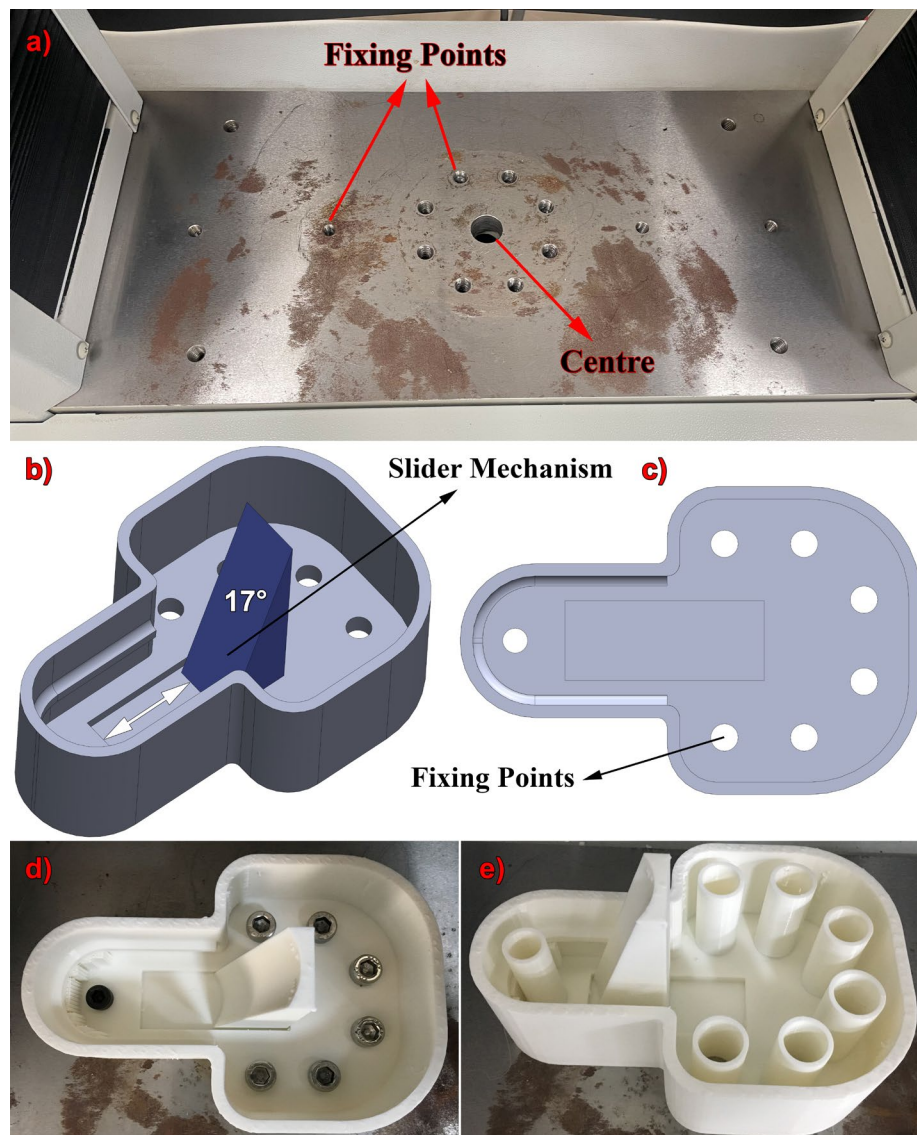


Figure 3.8: (a) Fixing points of the sliding mechanism to the tensile tester, (b-c) 3D drawing of the sliding mechanism, (d-e) 3D printing of the mechanism and its placement on the tester

However, some problems were encountered while printing the parts on the printer. One of these problems is that the printing process is frequently interrupted by filament breaking during printing. For this reason, a system has been developed that detects problems during printing, interrupts the printing process, and informs the user at the same time. The flowchart of the system is given in Figure 3.9.

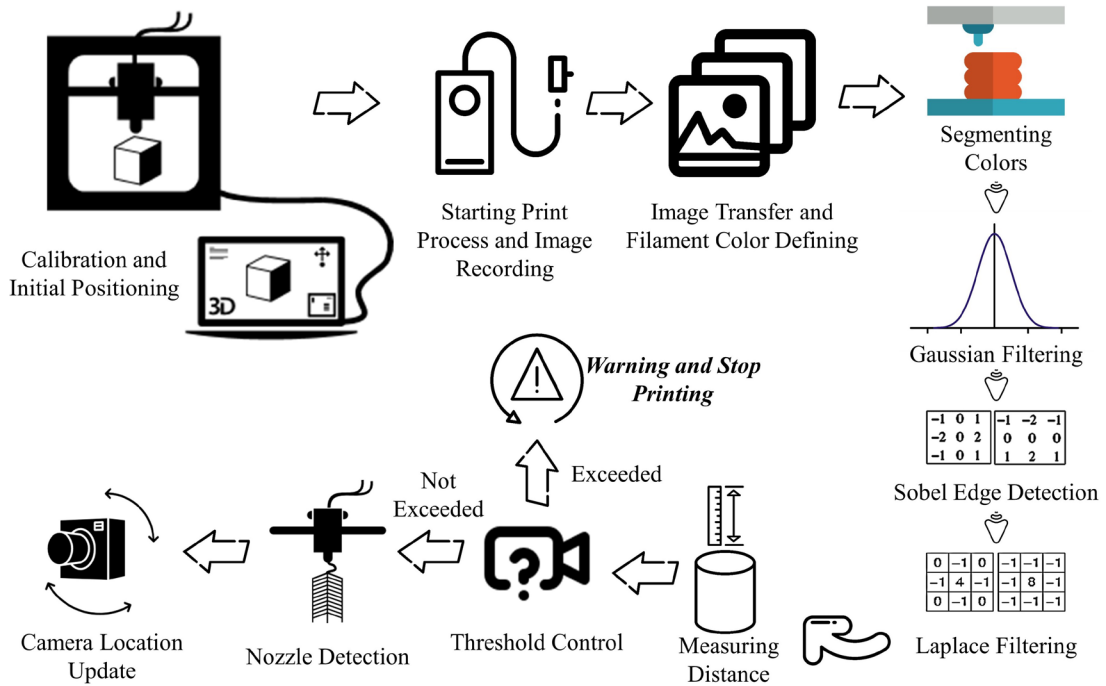


Figure 3.9: Diagram of the error-detecting system

In order to allow vertical movement of the camera, the base part that carries the rails was designed with SolidWorks and produced in a 3D printer (Ultimaker 2+ extended, Utrecht, Netherlands). The camera configuration was set up to allow the rails to move 30 cm and rotate 120° in the vertical plane. The vertical movement is performed by one of the motors, while the rotational movement is accomplished by the other. Arduino Yun with a Wifi connection and Ethernet port was preferred as the control unit. To obtain images, an OV7670 camera with 640x480 resolution, 25 angles of view, 30 fps image rate, 8-bit data resolution and 2.0 lens aperture was used. The setup of the developed system is shown in Figures 3.10a and 3.10b. The acquired images were transferred to MATLAB (v.2019a, MA, USA) software in real-time and the image processing was carried out. Firstly, the noise on the image was removed by

using Gaussian filtering. Because the image was acquired as RGB, color-based segmentation methods were utilized. The nozzle was identified by combining object and color segmentations since it is black and looks as a triangular. The background in the camera's field of view was adjusted to white for removing undesired objects (Figure 3.10c). Using edge detection algorithms, the nozzle of the printer, the printing bed and the printed part were distinguished. After the segmentation processes, the image was first converted to a grayscale to measure the gap between the nozzle and the part (Figure 3.10d).

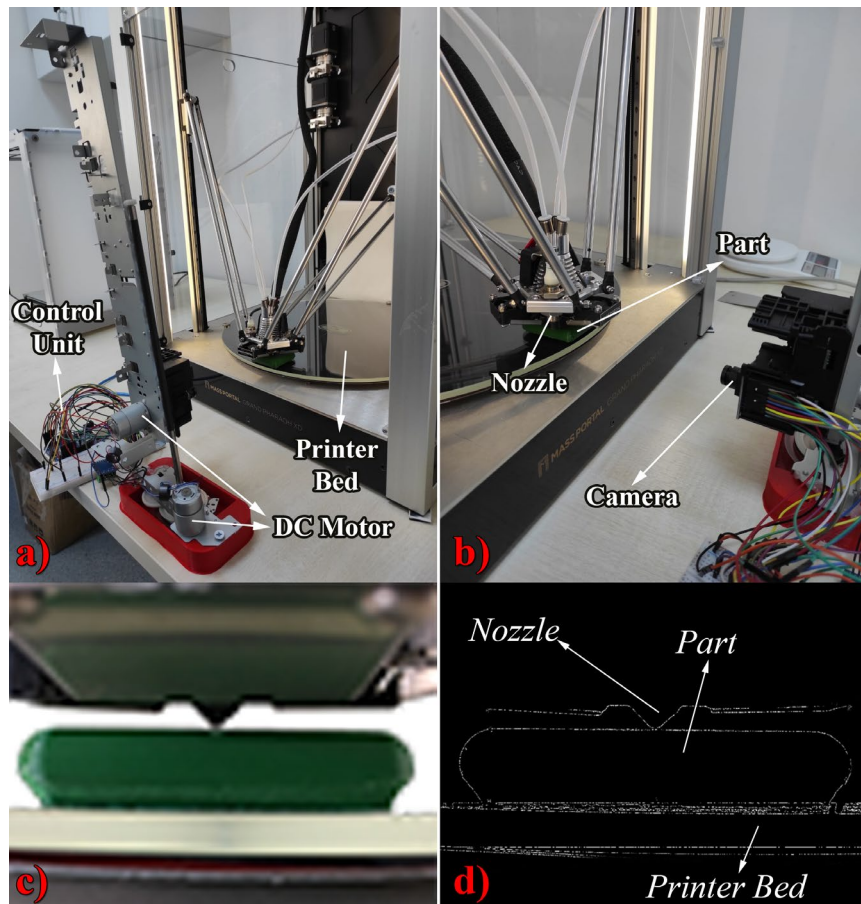


Figure 3.10: (a) Installation of a movable camera mechanism, (b) Adapting the camera system to the 3D printer, (c) Raw colour image captured from the camera, (d) Black and white image with detected edges as a result of image processing

Through the use of this system, which involves coding on an Arduino, any printing problems are promptly addressed [132]. Another problem is that the filament runs out during printing and the printer cannot detect this problem. Because the gripper required for the test was printed in large numbers, the filament frequently ran out and the printing process was interrupted. For this reason, the weight of the material was monitored simultaneously by placing a weight gauge on the filament holder at the back of the device. The mechanism to measure the weight of the filament was drawn using SolidWorks and produced by the printer (Figure 3.11a). The measuring procedure was carried out by using Arduino to process the data from the load cell (Figure 3.11b). In the software algorithm, by comparing the weight of the filament with the approximate weight of the part to be printed, it is checked whether the existing filament is sufficient. If the remaining filament weight is less than the required material weight of the part, the system stops working and requests the user to renew the filament (Figure 3.11c). A potential filament breaking may be detected by the system, which measures the filament's weight in real time, and the printing process can be stopped. The operation of the system is shown in Figure 3.11d.



Figure 3.11: (a) 3D drawing of the filament holder mechanism, (b) Calibration of load cell with standard weight, (c) Measurement of filament weight with precision scale and validation process with the system, (d) Adaptation and operation of all parts of the system to the 3D printer

### 3.2.3 Statistical analysis

In order to determine if there is a statistically significant difference between groups, test results for forces at four different displacements were analyzed using the analysis software SPSS (v.25, IBM, NY, US). Since there were two groups in this study, an independent t-test, also known as the two-sample t-test, was performed. This test compares the means between two unrelated groups after ensuring that the variances are homogeneous, the variables are normally distributed, and the dependent variable is continuous. In this study, the statistical significance level was accepted as 0.05. In other words, there is a significant difference between these two groups for loading if the p-value is less than 0.05.

## 3.3 Analysis of Miniscrews Stability

In order to analyze the stability of the miniscrews, the design of the miniscrews and their implantation methods were investigated.

### 3.3.1 The Effect of Miniscrew Head Designs

Miniscrew models and bone blocks were designed using SolidWorks (v.2016, SolidWorks Corp., Waltham, MA, USA). Five distinct miniscrew head designs were sketched in their real dimensions: cross head, mushroom head, button head, bracket head, and through-hole or circular head (Figure 3.12 [121,133,134]). All miniscrew types were accepted as cylindrical in form and sized so that their dimensions were 8 mm and 1.6 mm in length and diameter, respectively. The screws were not given threads in order to simplify the model. The cortical and cancellous structures were represented by the two components that made up the bone block. Instead of using complicated bone structures, the problem was simplified, and the bone block was recreated as a rectangular block in dimension 20x20x2 (WxDxH) for cortical bone and 20x20x13 (WxDxH) for cancellous bone [123]. Miniscrews were positioned at a 90-degree angle in the center of the block. The miniscrew cavity on the bone block was created using the tool of Boolean subtraction. Contrary to the previous study, this analysis was carried out by utilizing the simulation tool in SolidWorks. The contact

between the screw and the cortical and cancellous bones was defined as “fully bonded” [135]. All materials were assumed to be linearly elastic, homogeneous, and isotropic [123]. Elastic Modulus values were assigned to 114 GPa for the miniscrew, 14.7 GPa for cortical bone, and 1.5 GPa for cancellous bone. Also, Poisson's Ratios were determined as 0.34, 0.3, and 0.3, respectively. [136–138]. The ideal mesh size was found to be 0.5 mm after the mesh convergence study. (Figure 3.12h). In addition to the design of the miniscrew, the methods of application also have an effect on stability. For this reason, in the next step, different application methods are explained elaborately based on the cross head miniscrew design.

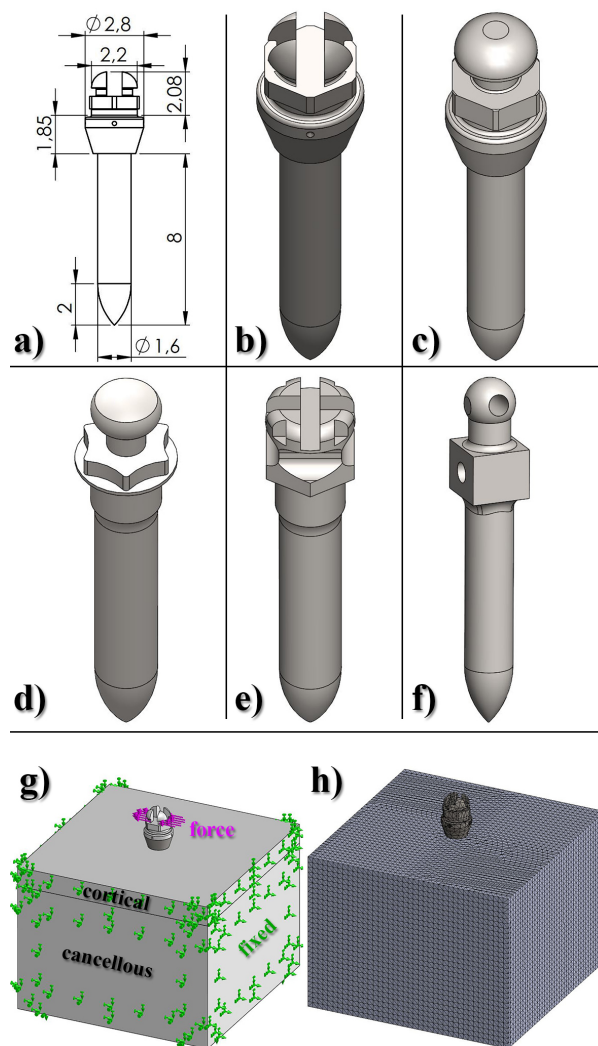


Figure 3.12: (a-f) Dimensions and 3D drawings of miniscrew; cross head, mushroom head, button head, bracket head, and through-hole head, respectively, (g) Definition of boundary conditions, (h) Meshing

### 3.3.2 The Effect of Application of Miniscrew to Mandible in Different Ways

The method to be followed to investigate the effects of different application forms on the mandible on the miniscrew's stability is shown in Figure 3.13. To model the mandibular bone, a patient's (17-year-old male) Dental Volumetric Tomography (DVT) scan was collected. The Izmir Katip Celebi University's ethics committee determined that our study did not require ethical approval (no. 0488, November 18, 2021). The patient applied to the hospital due to jaw stenosis and has no history of any other illnesses. The image was obtained using a NewTom<sup>®</sup> Panoramic Radiography (NT5G, QR Srl, Verona, Italy) with a 0.25 mm pixel spacing, a 704x660 FOV, and a 0.25 mm slice thickness. As seen in Figure 3.13a, the mandibular bone was extracted from the skull in the segmentation process using the Mimics program (v21, Materialize, Leuven, Belgium). To segment the hard tissue, a manually calculated Hounsfield Unit (HU) value in the range of 575 to 15383 was used. The artifact pixels were eliminated using the region-growing method. The teeth on the mandible were divided into segments and removed from the alveolar bone. Since it is challenging to distinguish between cortical and cancellous bones using radiological imaging, studies often involve approximation modeling [128]. The whole mandibular was subjected to a ten-pixel (10x0.25 mm) erode procedure in order to differentiate the cortical and cancellous bones. Then, cortical bone was created by subtracting the mandibular bone from the cancellous bone.

Cross head miniscrews were drawn in SolidWorks using the schematic of Tomas<sup>®</sup>-pin SD (Ti6Al4V, self-drilling, Dentaureum GmbH & Co. KG, Ispringen, Germany). Three separate miniscrews were used in its design, and their dimensions were as follows: lengths of 6 mm, 8 mm, and 10 mm; inner diameter of 1.2 mm; outer diameter of 1.6 mm; pitch width of 0.56 mm; pitch depth of 1.15 mm; and height of gingival collar of 2 mm (Figure 3.13b). After implementing the miniscrew into the inter radicular gaps between the first molar and second premolar at 11 mm from the alveolar crest, miniscrew models were imported as STL into Mimics and subtracted from the mandible model for grooving (Figure 3.13d) [139]. The miniscrews were not in contact with the tooth roots, and four different angles were applied: 45° and 60° from the

surface in the direction of the crown, 90° as perpendicular to the surface, and 15° inclined towards the root (Figure 3.13c).

Mesh defects were eliminated by evenly re-meshing the models using the 3-Matic software (v13, Materialize, Leuven, Belgium). The ten-node tetrahedral element, which is suitable for complicated geometries, is achieved with a meshing size of 0.3 mm (Figure 3.13e). Table 3.1 displays the models' element and node numbers. The same tooth models were employed in all combinations because the alteration of conditions had no impact on them. The total number of elements and nodes in the tooth model was 575.773 and 987.145, respectively. To remove the artifacts and spikes from surfaces, smooth and wrap operations were used in the Geomagic Studio program (v12, 3D Systems, Rock Hill, SC, USA). Finally, all models were imported as cdb file format to Ansys (v21r1, Workbench, PA, USA) for analysis.

Table 3.1: The number of elements and nodes of the models remeshed according to different application variations of all models

Angles	Models	6 mm		8 mm		10 mm	
		#Elements	#Nodes	#Elements	#Nodes	#Elements	#Nodes
-15°	All Bone	121484	213990	122095	214973	123234	216798
	Miniscrew	43028	79594	51260	94619	59092	108876
45°	All Bone	122757	215792	122065	214762	122628	215831
	Miniscrew	43115	79711	51188	94531	58867	108597
60°	All Bone	122309	215055	122099	214907	123335	216853
	Miniscrew	43037	79605	51158	94477	59030	108792
90°	All Bone	121892	214602	121862	214645	123093	216455
	Miniscrew	42968	79546	51216	94591	58946	108700

The material properties to be used in the models are given in Table 3.2, considering the literature. It was assumed that the finite element models had isotropic and linear elasticity properties. Since the condylar processes on either side of the jaw interact

with the temporal bone, they were fixed symmetrically in all directions as given in Figure 3.13f. The surfaces on which the force will be applied were defined to the head of the miniscrew (Figure 3.13f). Table 3.3 displays the component vector values at three distinct angles ( $30^\circ$ ,  $45^\circ$ , and  $60^\circ$ ) parallel to the bone surface in accordance with three different power arm lengths (4 mm, 6 mm, and 8 mm, as shown in Figure 3.13g), where the force was supplied as 200 gf ( $\approx 2$  N) [140]. Strictly bonded was used to describe the connection between the mandibular bone and the miniscrew. The contact algorithm for the models in Ansys was selected as the Augmented Lagrange approach.

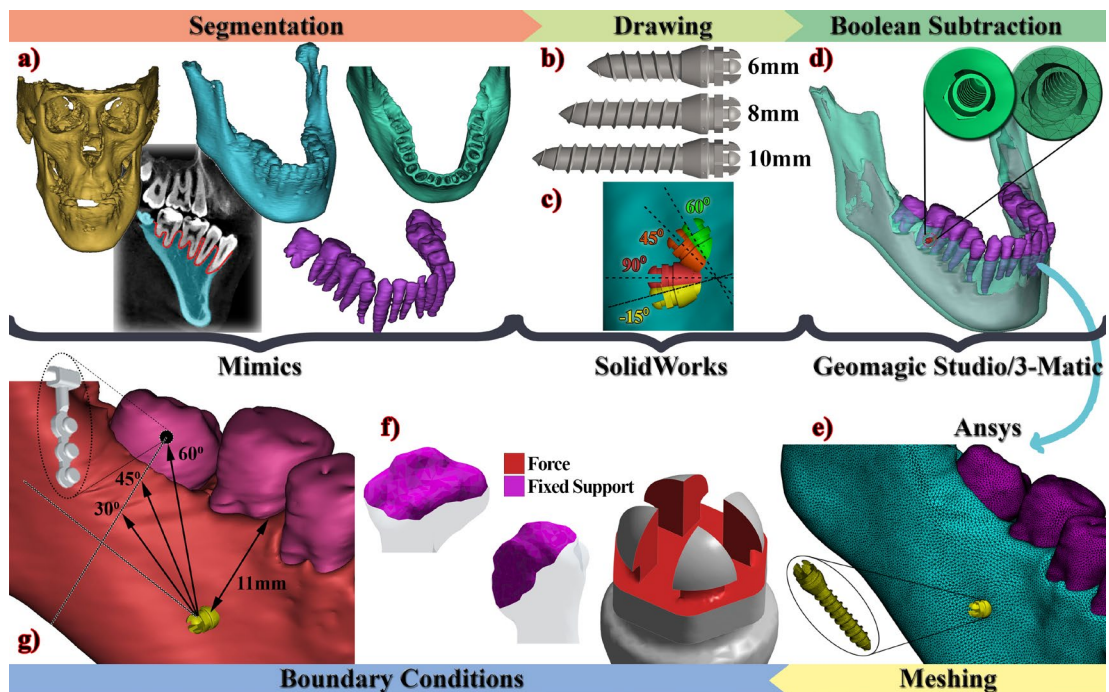


Figure 3.13: Workflow of the FEA process, (a) 3D image segmentation, (b) Drawing of miniscrews in CAD software, (c) Angulation relative to the frontal plane, (d) Transparent view of miniscrew inserted between teeth, and screw hole after removal miniscrew, (e) The meshing of mandible and miniscrew, (f) Force and fixed supports surfaces, (g) Force directions according to power arm

Table 3.2: Elastic modulus and poisson's ratio of FE models [126,128]

3D Model	Elastic Modulus (GPa)	Poisson's Rate
Cortical Bone	14.0	0.30
Cancellous Bone	1.3	0.30
Teeth	20.7	0.30
Miniscrew	113.0	0.30

Table 3.3: Components of forces vector according to angles (N) [141]

Force Direction	x	y	z
$30^\circ$	-0.30	1.73	1.00
$45^\circ$	0	1.42	1.41
$60^\circ$	0.42	1.01	1.68

# Chapter 4

## Results

The FE results and experimental results of the femur, tibia, and miniscrew studies are provided in detail. For the femur application, both experimental and FE analyses were carried out; however, FE analyses were not undertaken for the tibia plate comparison. On the other hand, only FE analysis results were given for the miniscrew application.

The deviation was calculated as the percentage error to assess the difference between experimental results and FE simulation results. It was computed by dividing the absolute value of the difference between them by the experimental result using the following equation [142]:

$$\delta(\%) = \left| \frac{\sigma_{FE} - \sigma_{EXP}}{\sigma_{EXP}} \right| \times 100 \quad (4.1)$$

where  $\delta$  is the percentage deviation of experimental results ( $\sigma_{EXP}$ ) from the FE results ( $\sigma_{FE}$ ).

### 4.1 Experimental results of Femur

The compression test results are given in Figure 4.1 for six cylindrical specimens. It is notable that the results of the standardized cylinder samples are very close to each other. The large number of samples is used to reduce potential test variations and manage the reproducibility of the results. Despite their being a variance across samples after the maximum force, the slope of the curve is nearly constant throughout all experiments.

For the purpose of determining the material properties of 3DP material, the slope on the force/displacement graph was computed at the boundaries of the elastic region. By choosing two different points on the curve, the tangent angle was obtained according to the formula (4.2). The compression tests took about  $69.00 \pm 15.59$  seconds for each sample. According to the results of the testing, the printed specimen's density is  $2.60 \text{ g/cm}^3$ , the average elastic modulus is  $347.43 \pm 37.34 \text{ MPa}$ , the maximum force is  $180.52 \pm 12.53 \text{ N}$ , and the strain is  $0.0385 \pm 0.0019$ . To provide data for the simulation, the properties of the 3DP material were computed.

$$E_{\tan\alpha} = \frac{\Delta\sigma}{\Delta\varepsilon} \quad (4.2)$$

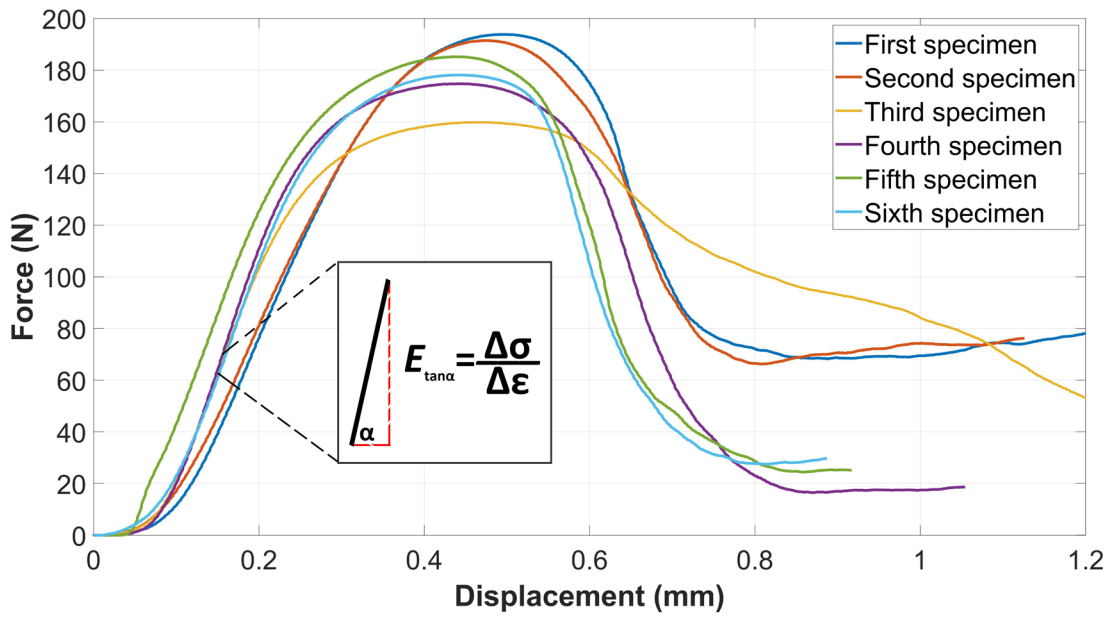


Figure 4.1: (a) The compression test results for six cylindrical specimens and calculation of Young's modulus from curves

On the other hand, according to compression results of the printed models, maximum stress values were observed as  $0.275 \text{ MPa}$  and  $0.234 \text{ MPa}$  for the left and right femurs, respectively.

## 4.2 Computational results of Femur

Using a workstation equipped with 64-bit Windows 8.1, an i7-4712MQ CPU clocked at 2.3 GHz, 8 GB of RAM, and a 2 GB video card, the FEA of both models and 3D reconstruction were carried out. Since rapid modeling/printing is significant in pre-operative planning, the time spent during the whole process is shown in Table 4.1.

Table 4.1: Time spent on each process

Process	Time (min)
3D reconstruction of the model	65
Pre-printing preparation	18
Build time	195
Drying and post-printing processes	90
Compression test	45
Defining of FEA inputs	12
FEA-runtime	3.21
<b>Total</b>	<b>428.21</b>

Although printing took up the majority of the time, due to printer technology, post-printing processes took a long time. On the other hand, the modeling process was incredibly quick because to the employment of a sophisticated computer and user-friendly software.

The simulation showed that the maximum stresses for the right FE femur model and the left FE femur model were 0.264 MPa and 0.308 MPa, respectively (Figure 4.2). In all models, the stress-strain curve was graphed for simulation and compression testing, and the red and blue circles in Figures 4.3 and 4.4 indicate the locations where maximum stress values were observed. Additionally, a statistical analysis of the correlation between simulation and experiment data in the linear elastic area was performed on the same graph. The correlation coefficients ( $r$ ) for the left model were determined to be 0.9987, and those for the right model to be 0.9960.

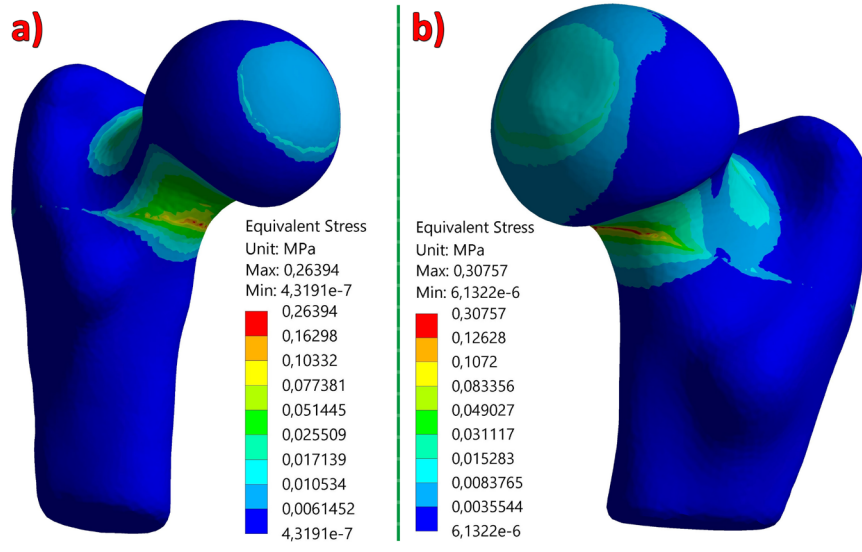


Figure 4.2: (a) The left model's and (b) the right model's stress distributions on the FE models

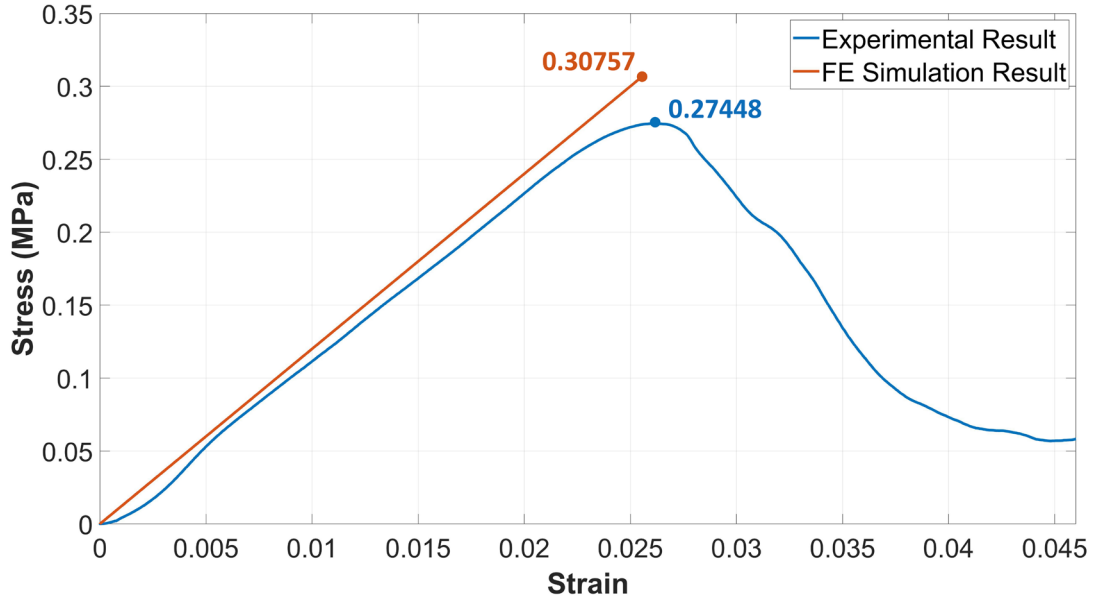


Figure 4.3: Comparison of experimental results and simulation results for the left model

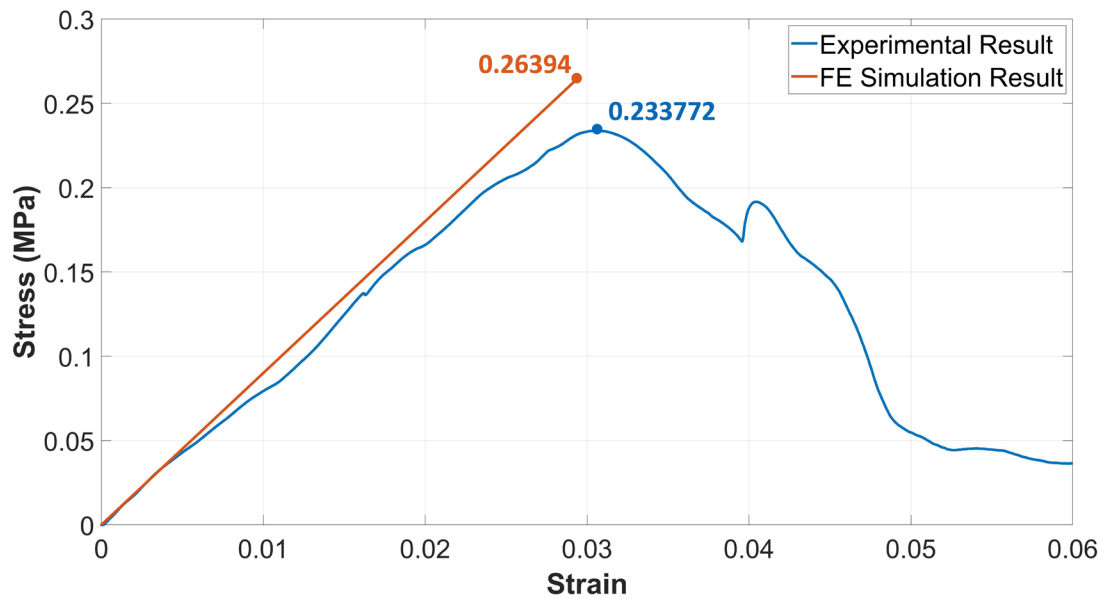


Figure 4.4: Comparison of experimental results and simulation results for the right model

### 4.3 Results of plates in composite bone

A statistical test was carried out for the forces corresponding to 4 different displacement values, which were decided as a result of the compression tests of both groups, MP and TP. The independent t-test was used and calculated against each displacement value separately in SPSS. The statistical results are given in Table 4.2 for each displacement.

Table 4.2: The statistical comparison of medial malleolar anatomic plate (MP) and tubular plate (TP)

Groups	Mean Axial Load (N) Mean $\pm$ SD			
	0.5 mm	1 mm	1.5 mm	2 mm
MP	55.54 $\pm$ 13.22	100.89 $\pm$ 33.64	148.97 $\pm$ 54.68	192.14 $\pm$ 76.89
TP	30.53 $\pm$ 14.78	49.42 $\pm$ 21.95	69.38 $\pm$ 22.84	95.04 $\pm$ 27.97
Mean Difference	25.01	51.47	79.59	97.10
P-value	0.006	0.005	0.007	0.015

According to all displacement results, a significant difference was observed between the two plates. Additionally, Figure 4.5 displays a box plot of the load-to-failure values for the two groups. The MP group required twice as much load to achieve a displacement as compared to the TP group.

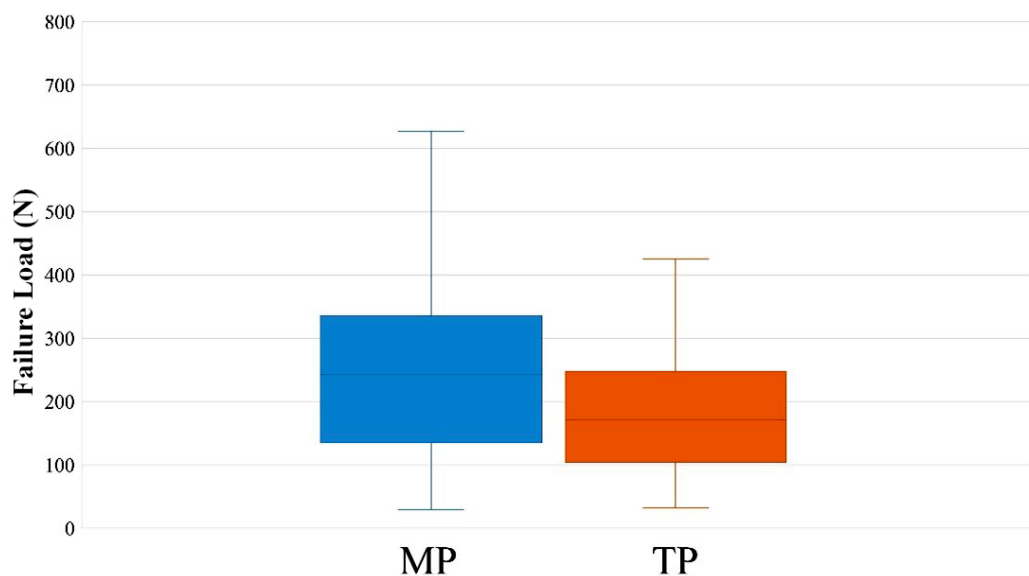


Figure 4.5: Boxplots of load-to-failure of two plates

Furthermore, the grippers manufactured for this study satisfactorily fixed the specimens without any cracking or breakage in all tests. Similarly, any cracking was not observed in the tile adhesive surrounding the bone samples during the test.

The details of the parts of the system developed to prevent printing problems are as follows: The first part was printed on the Ultimaker Extended 2+ using 49 g of PLA material at a cost of approximately \$1 and was completed in 4 hours and 2 minutes. In the second part, 71 g of PLA material were used, printed at \$1.43 in 6 hours and 56 minutes. These parts were successfully mounted behind the printer and the weight of the filament was tracked (Figure 4.6).

An example of printing problems encountered is mentioned below. The printing process has been started on the printer for printing gripper parts. While the filament weight is initially 650 g, it decreases as time progresses. In the 3rd hour of printing, the rate of weight reduction slows down due to nozzle clogging. Since there was no change in the weight measurement after a predetermined amount of time, the printing was halted and the user was expected to intervene.

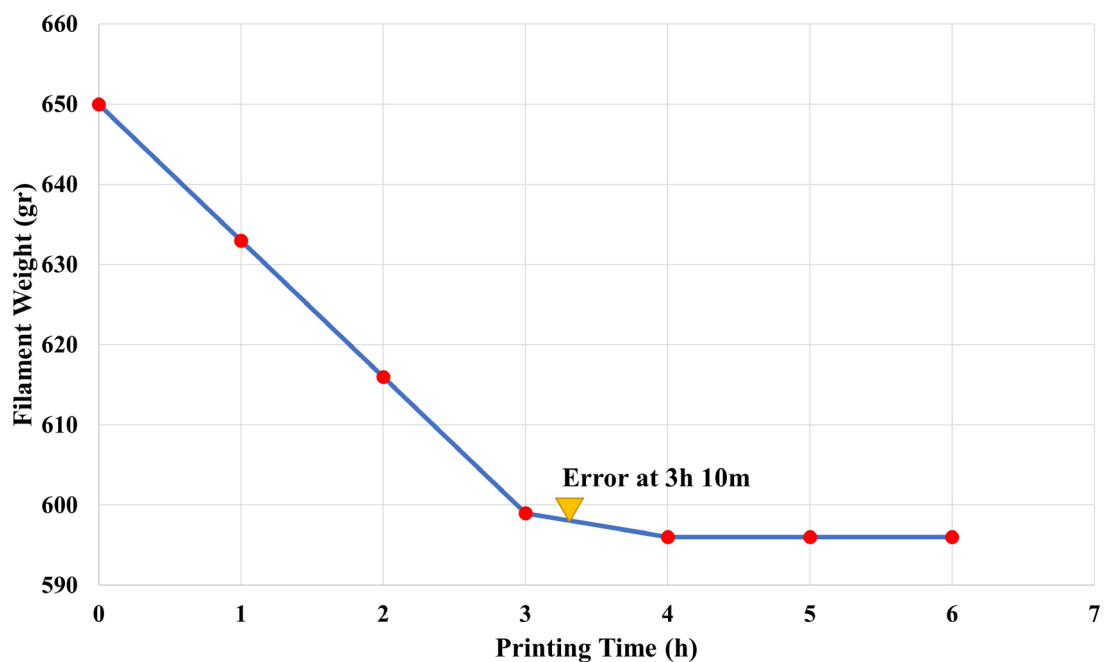


Figure 4.6: Measurement data of filament weight while the printer is running

Through another developed system, possible problems that can emerge in the 3D printer were prevented such as filament breakage, clogging, and slippage of a part from the printer bed. The distance measurement graph obtained in real-time with the image processing algorithms during the printing process is shown in Figure 4.7. Each layer's nozzle-to-part distance was assessed, and if it was more than the threshold value of 0.25 mm, printing was halted and the user was warned. During printing, this error occurred at the 54th layer number.

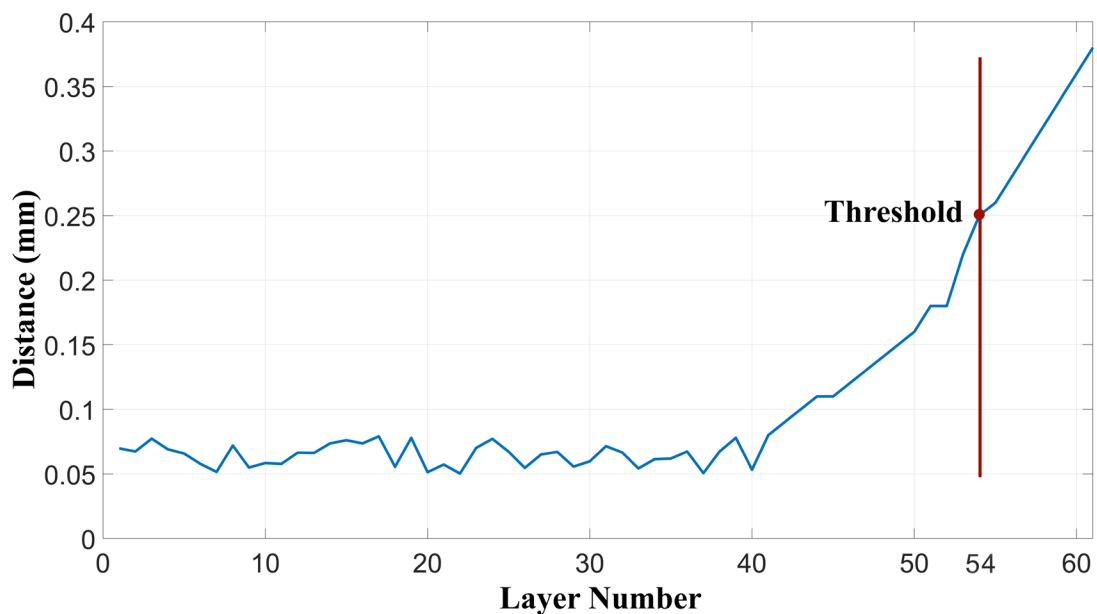


Figure 4.7: Measurement of the distance between the nozzle and the part according to the layer number

## 4.4 FE results of miniscrew applications

The finite element results of miniscrew head designs and their application to the mandible are given together in this section. Firstly, Table 4.3 shows the analysis results for different head designs. The bracket head miniscrew had the lowest stress, whereas the button head miniscrew had the highest amount of stress. Compared to the results of the cross head and mushroom head, which were almost identical, the through-hole

head performed a little worse. The stress distributions of the miniscrews are shown in Figure 4.8.

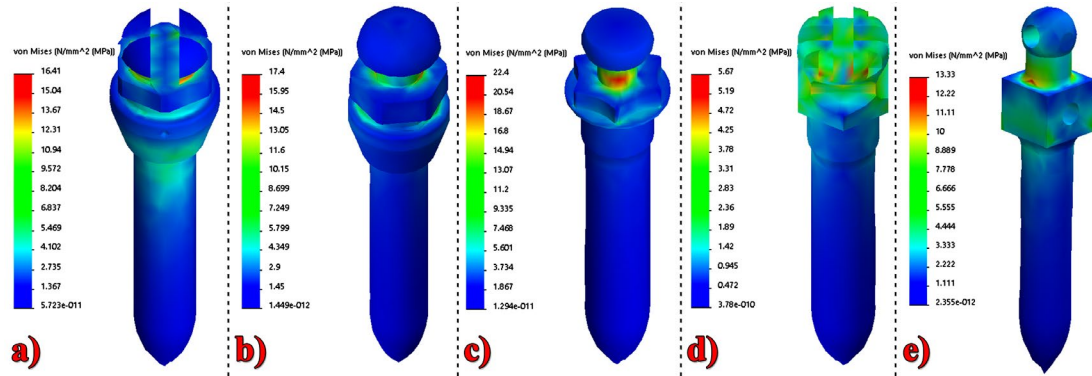


Figure 4.8: Stress distributions of Miniscrew head types isolated from bone block (cross head, mushroom head, button head, bracket head, through-hole head, respectively)

Table 4.3: Analysis results for each model

Miniscrew Head Designs	Cross	Mushroom	Button	Bracket	Through-Hole
Von Mises Stress (MPa)	16.41	17.40	22.40	5.67	13.66
Total Deformation (mm)	1.02E-03	7.80E-04	8.03E-04	4.26E-04	1.23E-03
Strain	1.66E-04	1.36E-04	1.45E-04	9.87E-05	1.45E-04

The collar and head sections of the mushroom head, button head, and bracket head were the areas with the greatest concentration of stress, despite the fact that stress was distributed across the thread components in cross head and through-hole head miniscrews. The neck area of the mushroom head and button head had the greatest stress value. On the other hand, it was determined that more stress occurs on the bone block in the button head compared to the other models. In all models, the stress was induced in the upper approximately 2 cm of the bone block, and the highest stress was

at the top surface and the intersection with the miniscrew. According to simulation results, the bone block's maximum von Mises stresses were 4.25 MPa for the cross head, 2.47 MPa for the mushroom head, 3.99 MPa for the button head, 2.49 MPa for the bracket head, and 5.80 MPa for the through-hole head.

According to the results of total deformation, the bracket head had the lowest displacement, whereas the through-hole head had the highest displacement. On the other hand, there wasn't much of a difference between button head and mushroom head miniscrews. The bracket head showed the least strain, as was the case with total deformation. However, the highest strain was calculated for the cross head miniscrew. The strain values in the button head and through-hole head were found to be almost indistinguishable. In Figure 4.9, all analysis results were combined and shown on a single figure by adding the colour scale to demonstrate the difference. Accordingly, Figures 4.9a to 4.9e show the stress distribution in the bone block by hiding the miniscrew. Figures 4.9f to 4.9j indicate deformed miniscrew models with a scale factor of approximately 1500. Finally, the strain results of the models are given in Figures 4.9k to 4.9o.

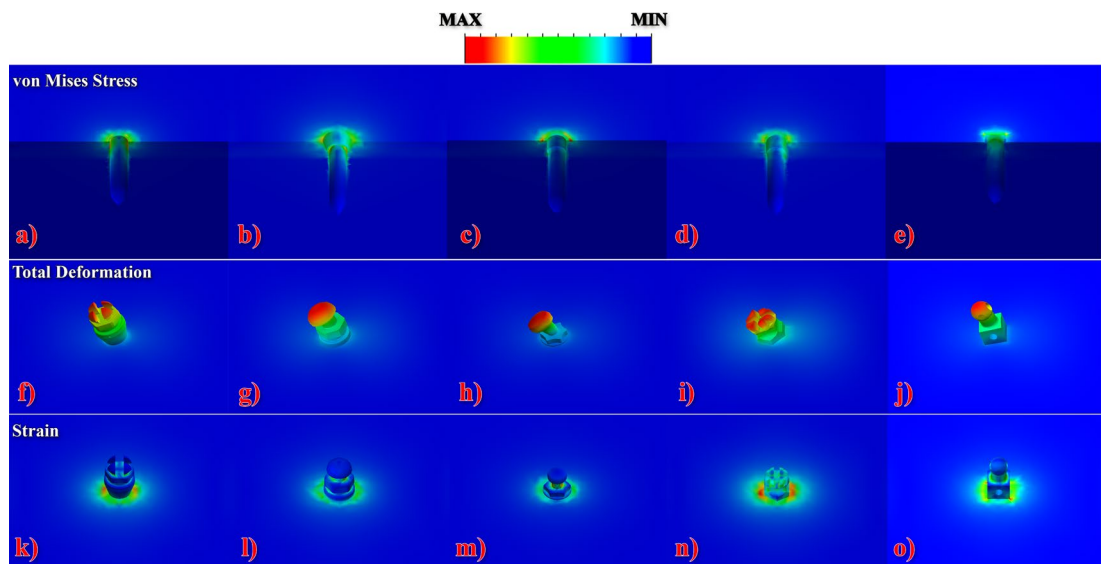


Figure 4.9: (a-e) Von Mises stress distributions of the miniscrew cavity, (f-j) Total deformations of miniscrew head types, (k-o) Equivalent strain results of miniscrew head types, for all images, from left to right, cross head, mushroom head, button head, bracket head, and through-hole head, respectively

Mesh convergence analysis was carried out by reducing mesh sizes from 2 mm to 0.5 mm. Figure 4.10 displays the outcome of the mesh convergence analysis for the mushroom head miniscrew. As a result, the allowable change was reduced below 5% with around 239 thousand elements in a 0.5 mm mesh size, and iteration was terminated. Additionally, nearly 230 thousand elements were calculated with little variation in 0.5 mm after an investigation of all models was completed. Node and element numbers for all models are shown in Table 4.4.

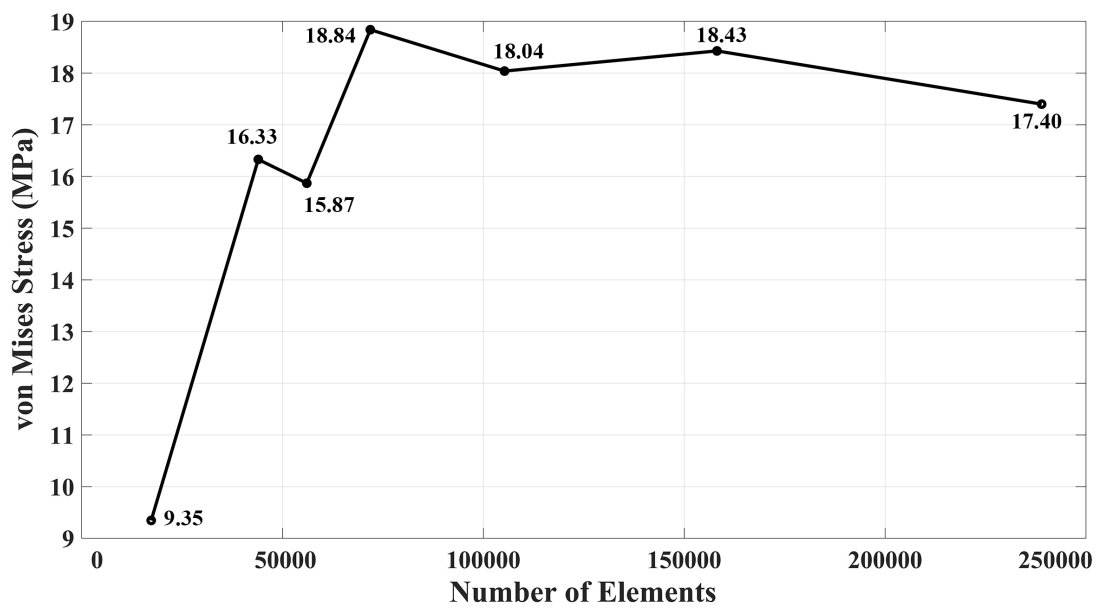


Figure 4.10: Mesh convergence analysis result for von Mises stress

Table 4.4: Meshing details of all models

Miniscrew Head Designs	Cross	Mushroom	Button	Bracket	Through-Hole
Total nodes	327361	334906	332820	331841	317955
Total elements	233030	238958	237563	236811	226359

Furthermore, the results of the analysis of different insertion methods on the mandible are mentioned in the following. In order to understand the impacts of insert angle, screw lengths, and force directions associated with the power arm on the mandibular, stress distribution and maximum von-Mises stress were determined. Maximum von-Mises stress results for different miniscrew insertion conditions are shown in Figure 4.11. Because there are 36 separate FE results in total, each main parameter's results are displayed as boxplots. Accordingly, the minimum and maximum stresses were determined at 18.61 MPa and 37.11 MPa for 6 mm and 10 mm lengths, respectively. On the other hand, the lowest stress was estimated at an insertion angle of  $60^\circ$ , while the maximum stress occurred at an angle of  $-15^\circ$ . Furthermore, considering the force directions, the lowest stress was  $60^\circ$  and the highest stress was  $45^\circ$ . As inspected individually according to the miniscrew length, the highest stress at 6 mm was obtained as 25.03 MPa at  $-15^\circ$  insertion angle and  $30^\circ$  force direction. On the other hand, a  $45^\circ$  insertion angle and a  $60^\circ$  force direction resulted in the lowest stress at 10 mm, which was measured to be 29.36 MPa. The maximum stress in 8 mm was calculated as 29.93 MPa with  $45^\circ$  at both insertion and force angles, and the minimum stress was 21.44 MPa with  $60^\circ$  at both insertion and force angles.

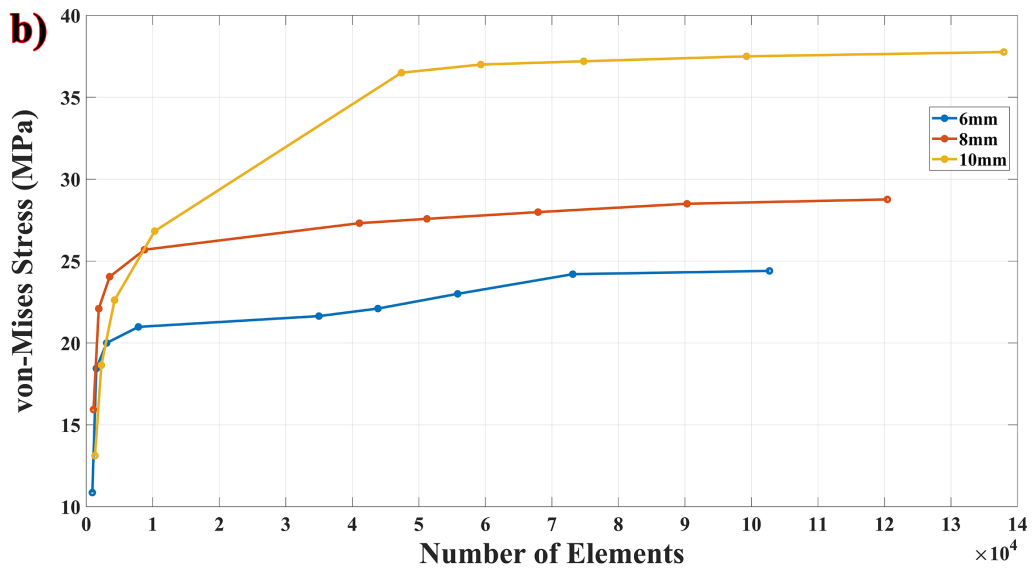
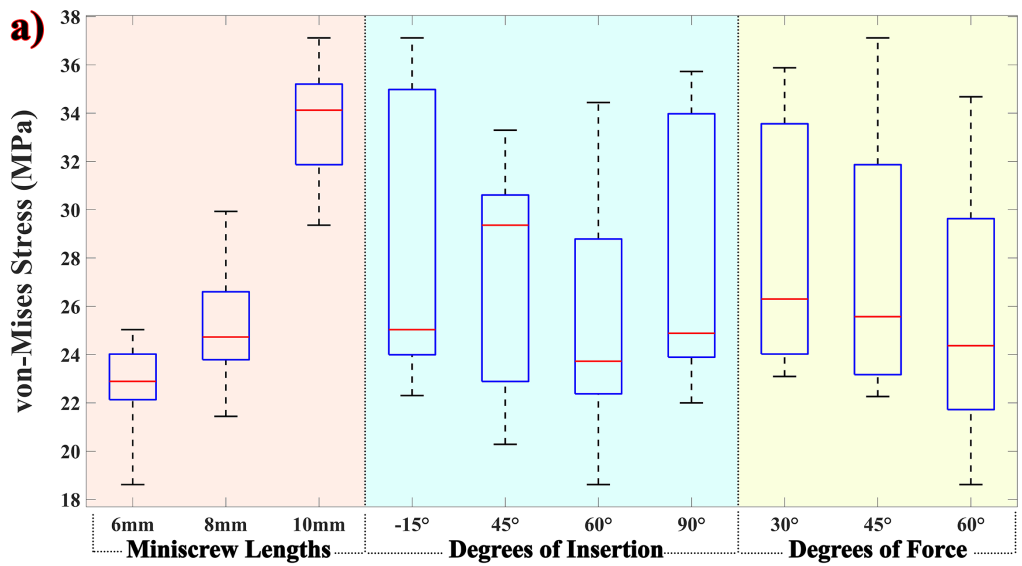


Figure 4.11: (a) Von Mises stress results of all models, (b) the graph of mesh convergence analysis for three models in different lengths

The stress was more evenly distributed than in other situations in the 10 mm screw length with a -15° insertion angle, where the stress is highest. At a screw length of 6 mm and an insertion angle of 60°, the mandibular surface is least affected by the stress distribution. In each case, it was discovered that the neck of the miniscrew was under the highest strain. On the other hand, the lowest stress points are towards the tip of the miniscrew. In addition, the stress distribution along the ramus on the mandible and the stress distributions observed only on miniscrews are shown in Figures 4.12a and 4.12b

for each condition, respectively. Moreover, for the convergence of results, sensitivity analysis was carried out by meshing them at various sizes ranging from 1 mm to 0.3 mm (Figure 4.12). Accordingly, FEA software accurately predicted von Mises stress at the ninth iteration with a 0.3% error.

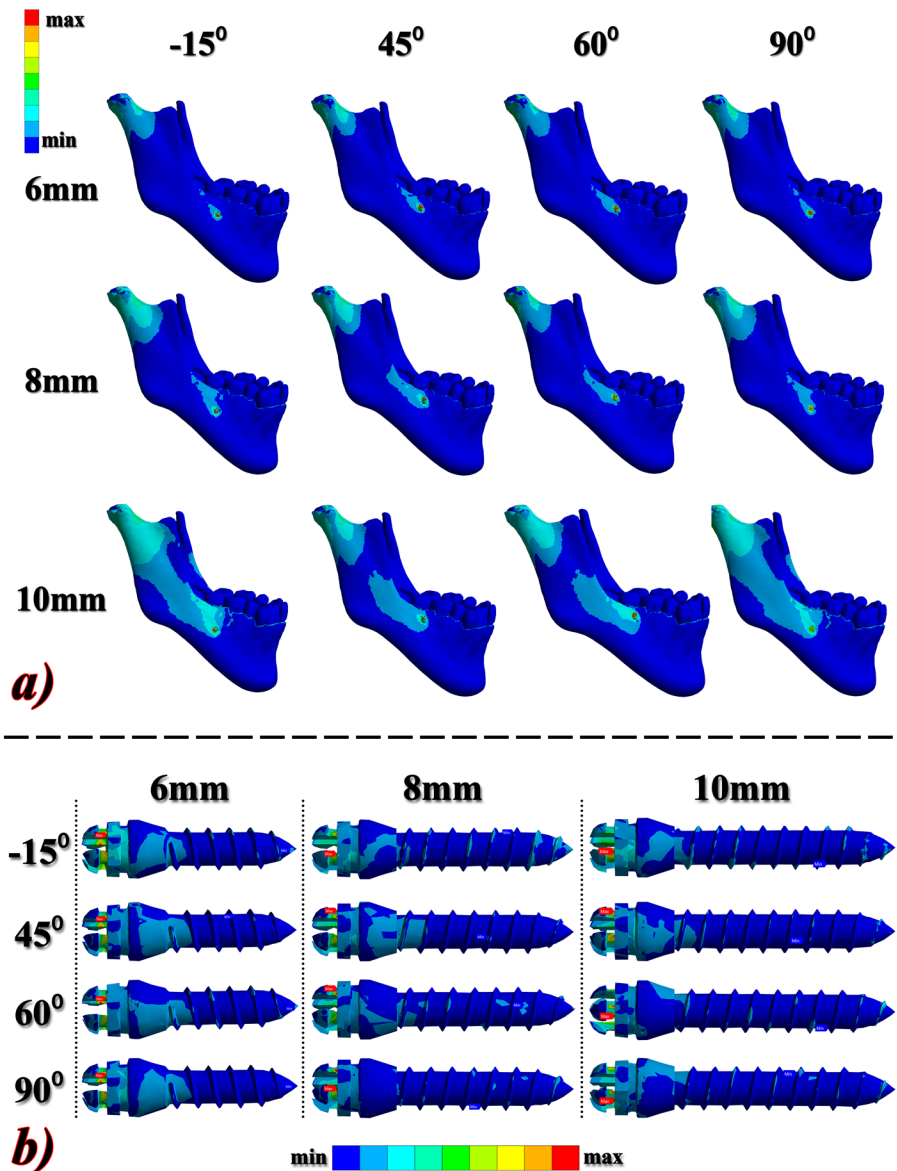


Figure 4.12: (a) Sagittal view of stress distributions on the mandible according to insertion angles and miniscrew lengths, (b) Frontal view of stress distributions of miniscrew separated from mandible and teeth models

The findings of the statistical analysis carried out to compare each group to itself are shown in Table 4.5. Because each group had a normal distribution and homogeneous variances, the Tukey test was chosen. As a result, in contrast to the others, a significant difference between the miniscrew lengths was observed. According to the Tukey test in Table 4.6, there were significant differences in miniscrew lengths between 6 mm and 10 mm and 8 mm and 10 mm. On the other hand, no statistically significant difference in force directions or insertion angles was calculated.

Table 4.5: Averages of von Mises stress values and statistical analysis results (\* indicates statistically significant differences and the significant value was 0.05)

	Variables	Mean (MPa)	± SD (MPa)	p-value
Miniscrew Lengths (mm)	6	22.99	2.35	0.001
	8	25.32	2.63	
	10	33.11	3.35	
Insertion Angles (°)	-15	28.11	5.94	0.432
	45	27.59	4.66	
	60	25.29	4.99	
	90	27.57	5.43	
Force Directions (°)	30	28.12	4.86	0.679
	45	27.75	5.33	
	60	25.55	5.35	

Table 4.6: P-values for each condition (\* indicates statistically significant differences and the significant value was 0.05)

Miniscrew Lengths/ Force Directions	p-value	Insertion Angles	p-value
6 mm – 8 mm	0.120	-15° – 45°	0.997
6 mm – 10 mm	0.001	-15° – 60°	0.674
8 mm – 10 mm	0.001	-15° – 90°	0.996
30° – 45°	0.983	45° – 60°	0.793
30° – 60°	0.453	45° – 90°	1.000
45° – 60°	0.559	60° – 90°	0.798

In this study, simulations were conducted on a computer with the Windows 10 operating system, an Intel Xeon 3.50 GHz CPU, and 16 GB of RAM. Even though each model's computation time was different, they all required around 8 minutes and 50 seconds.

# Chapter 5

## Discussion

In this section, the simulations performed for femoral head fractures and miniscrew stability to eliminate the deficiency in the literature and all processes and challenges confronted are discussed in detail. Although both simulation and experimental studies were carried out for femur fractures, only simulation was performed on miniscrew stability due to the lack of a measuring device and the tiny dimensions of miniscrews. Firstly, in the femoral head fractures, it was concluded that the FE results were remarkably similar to the experimental result. Accordingly, there was a 12.06% deviation between the simulation and the compression test for the left model and 12.90% for the right model. In the following, similar studies in the literature were examined and their results were provided. Haider et al. calculated a minimum 9.6% and a maximum 14% average error between FEA results and experimental study [143]. According to another study using human cadaver femurs, the mean absolute deviation between the experimental study and the FEA was determined to be 22% [144]. As a consequence, it can be deduced that the deviation rate ( $\approx 12\%$ ) is comparable to that of previous research and even produce better results than some of them. In addition, maximum von-Mises stresses were determined in the femoral neck in left-right models for the predicted stress distribution by FE simulation (Figures 4.2a and 4.2b). Likewise, the femoral neck appeared to be where the fracture first emerged in the compression test (Figures 3.5c and 3.5d).

Moreover, the results' correlation coefficients ( $R^2=0.99$ ) are higher than in prior research. Lengsfeld et al. found that the correlation coefficient between three different techniques that combine simulation and experimentation ranged from 0.91 to 0.94 [145]. Similarly, Hambli and Allaoui (2013) reported that the correlation coefficient between experimental and FE simulation results in proximal femur fractures was 0.94

[146]. Trabelsi et al. (2011) reported a high correlation ( $R^2=0.93$ ) between patient-specific FE data and experimental results on human femurs, in another study [144].

Femur fractures are relatively prevalent, especially in the elderly, and their surgeries can be particularly challenging [147]. Technologies that facilitate doctors' accountability have been developed and used in the healthcare industry over time [148]. This study has demonstrated how 3D printers may speed up a variety of daily tasks and deliver effective outcomes in the medical industry. It is also safe to use in the training of biomedical engineers and in the field of medical education. The democracy of 3D technology and material costs have been decreasing day by day. Students and lecturers will therefore be better equipped to comprehend the theory thanks to practical instruction [149].

The creation of anatomical models using 3D printers and FDM principles has been discussed in the literature from many different perspectives [150]. The affordable price of FDM printers is one of the causes [151]. However, they need a large number of anatomical models because FDM printers take a long time to produce and need support structures [152]. On the other hand, BJ, SLA, and SLS technologies may be used to print tissue architectures in reality. These methods can produce extremely satisfactory outcomes for delicate objects that demand attention to detail. The results of this study using BJ powder technology were obtained to be quite accurate, and the finite element analysis and experimental results were in agreement. Additionally, it has been demonstrated that faster printing is possible, and the cost of components created with BJ is fairly comparable to those made with other techniques. While the same models took roughly 3 days to print on an Ultimaker 2 Extended, the material cost was estimated to be around 370 g with 50% infill. In contrast, 197 g of the material was used in the BJ, and the printing process took roughly 3 hours. This time interval is about equivalent to one-twenty-fourth of all FDM printing. Considering the cost, model printing with FDM is roughly \$22.5, including energy costs, whereas printing with BJ cost a total of \$26. BJ has significantly faster printing times than FDM but is slightly more expensive overall. The printing duration is crucial for preoperative planning because patients should wait as little as possible [153].

One of the study's limitations is that bone phantoms can only be printed using the same powder material in Projet160, which results in the production of cortical and trabecular structures with identical material properties. However, by separating these components, high-resolution printing of the model can solve this problem. Through the use of a quite low layer thickness (0.1 mm) and a powder-filled printer bed, this printing technique may produce porous structures suitable for the 3D model of the femur bones [154]. The smaller layer thickness is feasible with the most recent SLS or BJ printers. Table 1.4 lists different powder technologies with resolutions that range between 10 and 150  $\mu\text{m}$  [155]. In addition, because the BJ technique doesn't require support structures and the excess powders can be recycled, it also reduces wasteful material usage. On the other hand, compared to FDM, the main drawback of the powder technique is the part's weak mechanical strength. Depending on the material, FDM methods range in strength from 20 to 75 MPa (Table 1.4), BJ prints' strengths can reach up to 48 MPa after being impregnated with a specific binder made of polyester resins [156]. However, 3D models, which have a high strength, are not necessary for the aforementioned uses. In addition, compared to other printer technologies, because we are unable to use an SLA printer, a cost and time analysis could not be conducted.

Producing a 3D image for the segmentation of CT images is quite simple using the free software in Table 1.6. The segmentation procedure, however, may vary depending on the CT equipment, the Hounsfield Unit (HU), the bone structure, etc. The threshold algorithm considers the HU value to be a level value, and the best value can be either indiscriminately or automatically determined [157]. Sometimes this value may not comprise hard tissue, and sometimes soft tissues may be contained. It is challenging to determine the threshold value since it might differ based on the radiological instruments and even from record to record. As a result, including the incorrect tissue in the model might lead to inaccurate findings. In this study, the most accurate model was produced by a layer-by-layer analysis of the image utilizing adaptive threshold and region-growing techniques.

Furthermore, besides the 3D-printed bone model, different fixation methods were compared in the study with composite bone. The medial malleolus plays a significant role in supplying ankle stability; hence, the treatment technique is highly significant.

However, nowadays, there is debate regarding the best fixation technique. Orthopedists typically favor K-wire, tension bands, or screws as treatment options.

The novel medial malleolar compression plate has the following benefits:

- The medial malleolar plate delivers compression at the vertical fracture site because of its distinctive sliding mechanism.
- The likelihood of skin issues is limited because of its low profile, and we believe that it won't need to be removed.
- Owing to the strong fixation, it will be able to support weight-bearing and early ankle motions.
- Numerous screw choices may be available.

Limitations of composite bone models

- Since the generations of composite bones are crucial in biomechanical studies, the latest generation will give the best results, but the cost is quite high.
- This novel plate is not compared with hook plate.

Moreover, in this thesis, in the process of printing the slider mechanism in 3D, solution methods for printer problems have been developed. The printing process on 3D printers is fraught with problems such as filament breakage, nozzle blockage, power failure, material shortage, or filament holder drop. For example, the filament flow is interrupted, and the printing process continues without melting the filament because the 3D printers cannot deliver this flow. This results in a waste of time because the printer is idle and the printing process is disrupted. A tracking system with a camera and weight measurement has been designed to address these kinds of problems. Hence, by stopping the extrusion flow and motor mobility, significant electricity costs are avoided. In addition, recently considering the increasing costs, filament losses are prevented. The aforementioned faults are detected early thanks to this study, and time lost is minimized by informing the user. The system monitoring the weight of the filament uses a load sensor to determine whether the filament is moving smoothly, giving the ability to identify problems with printing. Compared to other studies detecting printer errors, Straub has established a good approach, however huge costs

have emerged [158]. In addition, Lyngby et al. used complicated robotic systems by minimizing the cost [159]. While many image processing-based defect detection systems have been developed, a system that measures filament weight has not been designed yet. Both tracking systems simultaneously track the printing and successfully detect possible errors. Additionally, the system can be modified to work with many printer types as long as it doesn't interfere with 3D printer performance.

In another study, on the effects of miniscrew head designs, the stress distributions were concentrated on the shanks of the miniscrews in cross head and through-head designs. This was assumed to be caused by the various collar styles. Since it was determined that collar and neck designs are crucial and their differences have a significant impact on the result. For instance, because of the smaller diameter design, the neck absorbed the maximum stress in the button design. This led to the conclusion that von Mises stress and neck diameter had an inverse relationship. Because the button head, mushroom head, cross head, through-hole head, and bracket head all had lower neck diameters of 1 mm, 1.3 mm, 2.2 mm, 2.83 mm, and 2.6 mm, respectively. The high neck diameter and hexagonal collar of the bracket design are two factors that contribute to its lower stress than the others. Additionally, compared to the through-hole, which has a cube design, and the bracket, which has a hexagonal design, the results of von Mises stress are higher in the cross head, mushroom head, and button head, which have a cylindrical neck design. The hexagonal neck shape lowers the stress value despite the cross head and bracket head designs being near to one another. The stress distribution in the bracket head design was restricted to the miniscrew head and was unable to impact the miniscrew tip. One of the lowest von Mises stresses in this design was determined to be 2.49 MPa in the bone block. The mushroom head, with a von Mises stress value of 2.47 MPa, is another design with a low von Mises stress in the bone block. With a total length of 4.75 mm, the neck and collar components have the highest design, which prevents stress from spreading to the miniscrew tip. The bracket head, at 4.07 mm, is the next-highest length after the mushroom head. The load on the miniscrew head is increased in these two designs because the overall length of the neck and collar component is longer than the other parts. Additionally, the load is divided into four in cross and bracket head designs so that it is spread equally across the surfaces. Since the two stress values were so widely apart, the parameter's impact on stress was, however, rather modest. On the other hand,

with other head designs, the load is delivered along a cylindrical surface. Although the results from these models are quite similar, it cannot be established that only one parameter influences stress because there are several other factors that vary. However, applying force to different surfaces caused a change in the region where the stress is concentrated. Consequently, the stress in the cross and bracket head designs was concentrated at the corner points and finer trims, which may cause it to become more fragile. The distance between the bone surface and the applied load is another crucial factor. The cross head, mushroom head, button head, bracket head, and through-hole head all have a distance of 2.81 mm, 2.6 mm, 1.5 mm, 1.81 mm, and 2.15 mm, respectively. On the other hand, Table 4.3 shows that the order of highest stress values is button head, mushroom head, cross head, through-hole head, and bracket head, going from largest to smallest. The button head created the most stress while having the shortest distance. The maximum distance, on the other hand, was measured at the cross head, and an average stress value was determined. Hence, it is not possible to assume that the distance of the applied load to the bone surface and the resulting stress has a linear or inverse relationship. However, this variable showed that it had an impact on the findings of the research.

All models had about 20,000 elements at the beginning, and there were about 230,000 elements at the end of mesh convergence. These numbers are higher than those in prior research, which increases the computational time [138]. However, a small element size is required to converge the output and reduce the impact of a mesh size change to less than 5%. After mesh convergence analysis, von Mises stresses corresponding to previous studies were verified. By applying 2 N of force to a miniscrew head at a 90° insertion angle, Te-Chun et al.'s study, for instance, calculated von Mises stress as roughly 15 MPa [123]. The stress value from our study's cross head, mushroom head, and through-hole head designs is remarkably similar to this amount. Similarly, while they calculated the total deformation as 3 μm, our study determined approximately 1 μm of total deformation in the cross head and through-hole head designs. In the study of Letizia et al., von Mises stress was calculated as 5.6 MPa in the bone block when they inserted the miniscrew as perpendicular and applied 2 N to the miniscrew head at a force direction of 0° [124]. The highest von Mises stress value determined by our simulation was 5.8 MPa and was found in the bone block. Even though the FEA software used in the two research was different, highly similar results were found. The

von Mises stresses in Yushan et al.'s research to compare the thread properties were between 9 and 20 MPa with their designs similar to our cross head design [122]. Correlatively, in our study, the von Mises stress value was 16.41 MPa in the cross head. Considering all the results, they were very supportive of the validation stage of our models because we produced results that were comparable to previous research.

There are some limitations to this study. The first is that the bone structure is not homogeneous and has anisotropic properties that show different characteristics everywhere. However, solving such a complex problem is tricky and requires more running time in FEA. Additionally, it takes a long time to establish the material qualities via image processing, and computed tomography scans of the maxilla or mandible are required. Thereby, the bone structure was simplified, and a bone block was used instead of a complex bone structure. The bone structure was represented by defining two material properties, cortical and cancellous, in the bone block. Although the cortical thickness in the literature varies, it was determined as 2 mm on average [123]. The effect of bone density on the results is not the focus of this study. In addition, it was demonstrated that this is not a disadvantage since the same bone block is used in all models. Another limitation is that the thread design is not included in the models. Studies deal with optimal dimensions by changing thread properties [122]. However, in this study, threads are not created to avoid problems in the contact regions and to ensure mesh convergence. Because contact meshes in the cavity of the bone block with the miniscrew threads are sometimes not detected, analysis cannot be solved. Not creating threads on all models does not cause a disadvantage because other dimensions are the same on all models except for the head designs. As a result, this study did not investigate more characteristic features by keeping the insertion angle, miniscrew dimensions, force direction, and bone properties constant. Since there are studies assessing and comparing these parameters, they are not the focus of this study.

In this study, since the different miniscrew head designs available on the market were compared, their original dimensions and shapes were not modified. Among these designs, neck and collar geometries, head designs and dimensions, and force properties applied to the surface were discussed as a whole instead of examining their effects separately. However, investigating each of these parameters in detail will be beneficial for developing a more stable miniscrew in future studies.

Furthermore, in our other study, finite element models of the mandible and the miniscrew were created, and the stress patterns generated by the implants at the bone-implant interface were assessed under different insertion angulations ( $-15^\circ$ ,  $45^\circ$ ,  $60^\circ$ , and  $90^\circ$ ) to the alveolar process bone, screw lengths, and force application directions by using the 3D finite element method. This study was performed on the mandible model to assess the effects on the mandible and to resemble the simulation as close to reality as possible, instead of assuming a representative bone block by simplifying the mandible. As in our previous study, studies have often used FEA on the bone block to compare various parameters and determine the stability of the miniscrew. Issa Fathima et al. investigated the stress produced by varying the miniscrew lengths and cortical thickness at various insertion angles. They claimed that the stress intensified as the miniscrew length extended and that the stress was lowest at an angle of  $90^\circ$  [125]. In an alternate study, Te-Chun et al. evaluated the von Mises stress on the bone block by changing a variety of miniscrew configurations. They also observed that as the miniscrew length increased, the stress increased as well [128]. In our conducted study, the stress increased as the miniscrew length went from 6 mm to 10 mm (Figure 4.11a). The lengthening of the miniscrew alone does not, however, outweigh other factors. In addition to miniscrew length, additional factors that affect primary stability include insertion angle, force direction, cortical thickness, and miniscrew diameter. For example, the results for 6 mm miniscrew length and a  $-15^\circ$  insertion angle and 8 mm miniscrew length  $60^\circ$  insertion angles were almost the same. Thus, a variety of factors influence the outcomes of the simulation. In the study of Letizia et al. on the bone block, they calculated von Mises stress of approximately 31.2 MPa in the 8 mm miniscrew length and  $90^\circ$  insertion angle by applying 2 N to the miniscrew head [124]. We computed this value by simulating equivalent scenarios in our study, and it is exceedingly comparable to the 24.9 MPa stress. However, in their analysis, the  $120^\circ$  insertion angle had the highest stress value. In another study by Hamidreza et al., in which they compared the effect of thread on the bone block, the average of all different situations was 36.94 MPa at  $0^\circ$  force direction and  $90^\circ$  insertion angle at the same force and about 10 mm miniscrew length [127]. An average von Mises stress of 35.72 MPa was calculated in our study using a 10 mm miniscrew with a  $90^\circ$  insertion angle. Additionally, they observed that the stress dropped as the force angle increased, which is consistent with the findings of our investigation. On the other hand, there are studies

using more complex simulations than bone block simplification. Hussein et al., who performed treatment planning on the mandible, determined von Mises stress as 26.5 MPa by applying a 2 N compression force to 8 mm miniscrew length [126]. Similar to this, when positioned perpendicular to the surface with identical miniscrew parameters, our von Mises stress was measured at 25.63 MPa. In another study accomplished by Jason, an FEA model of the maxilla bone was created and inserted with an 8 mm length and 1.6 mm diameter miniscrew with three different insertion angles of 45°, 60°, and 90°. The lowest reported von Mises stress was 31.56 MPa at 60° [141]. Our research reported that von Mises stress was lower than the others at a 60° insertion angle for all screw lengths and force directions (Figure 4.11a).

The results of statistical analysis show that the variation in miniscrew lengths is consistent with the findings of prior studies. In fact, it has been convincingly demonstrated that an increase in the miniscrew's length results in a considerable alteration in stress. In contrast, there were no noticeable changes in the insertion angles or force directions. In a similar way, Jason et al. found no significant difference in cortical bone stress at any insertion angle [141].

Prior studies often used varied angulations parallel to the vertical plane for the force delivered to the miniscrew head [127,128]. However, this is very difficult in terms of application, especially at angles like 60° and 120°, because the force is applied as a mixture of horizontal and vertical planes, to power the arm or bone directly. Therefore, in this study, 30°, 45°, and 60° varying angles according to the force arm length were investigated instead of changing the force in the vertical plane.

Miniscrew success rates have been documented by several authors in the literature, however, the association between the angulation of miniscrew insertion and stress on the bone has not been sufficiently investigated [125]. The primary mechanical stability of miniscrews is greatly influenced by direct contact with bone. The invasion of inflammatory cells as a biological reaction does not occur in areas of direct contact. The mineralized bone tissue is in contact with the miniscrew one day after it was inserted, and osteoblasts are firmly adhered to the titanium implant surface. After about 1-2 weeks, the bone resorbs in areas with direct bone contact and is replaced by newly formed living bone. Miniscrews remain clinically stable despite the temporary loss of

hard bone contact. However, under different conditions and depending on the application, it can be observed miniscrews failure or loss. This study demonstrated that using bigger miniscrew lengths and a  $-15^{\circ}$  angulation would result in a higher failure rate.

Various other factors that may play a role in the stability of miniscrews and affect the success rate have been investigated in the literature. First of all, the self-drilling miniscrew utilized in this investigation had a diameter of 1.6 mm and a head length of 2.2 mm. Since they have more bone connections, drill-free screws were chosen. However, it has been advised to use the predrilling technique for inserting miniscrews into thick cortical bone [140]. In addition, miniscrews can be displaced within the bone during mechanical retention. Liou et al. reported that the miniscrews applied 400 grams of force were extruded 1.0 - 1.5 mm in 7 of 16 patients and overturned [105]. Studies report that an average of 0.5 - 2.0 mm thick bone should be around miniscrews and authors suggested that miniscrews should be placed at certain distances from anatomical structures [160]. Moreover, Gracco et al. reported as a result of their FEM analysis that the lowest values of the maximum von Mises stress for a given level of osseointegration were calculated for 9 mm screws at the lowest miniscrew length in their study. The authors explained the reason for the increase in the magnitude of stress with the increase in the screw length is due to the increase in the bending moment acting first on the screw and then on the bone [161]. Therefore, in this study, the cortical thickness was determined as 2.5 mm in the FE modeling, and the inter radicular spaces between the first molar and the second premolar at a distance of 11 mm from the alveolar crest were chosen as an optimal miniscrew insertion site [139]. The lowest stress values occurred at the shortest screw length of 6 mm, in line with previous studies.

# Chapter 6

## Conclusion

In this thesis, hard tissue-related finite element analyses were carried out. The first of these analyses was performed on femur fractures, and their experimental validation was provided. At the same time, how the femur samples will be obtained in 3D and the results of the compression test application have been compared statistically. Additionally, commercial composite tibia bones to find the best fixation technique in medial malleolus fractures have offered an alternative to 3D-printed bone models in the experimental study. Both models' benefits and drawbacks for use in preoperative planning, training, and biomechanical testing are thoroughly discussed. Simultaneously, a 3D-printed gripper that was appropriate for the study's test device was created, and occurred printing issues were overcome using a real-time monitoring system with image processing and measuring of filament weight. In addition, the most strength primary stability methods were investigated using FEA with various application methods for miniscrews, which have been frequently used in orthodontics recently. The following provides further information on the findings of these studies.

The CT-reconstructed models were appropriately manufactured on a 3D printer. Since biomedical engineering is expanding in our country, it is essential that these technologies be understood and applied extensively. This thesis outlines the use of 3D printers to produce human or patient hard tissue. In the near future, anatomical models will be possible to be produced by means of the expansion of 3D printers in educational institutions. The biocompatible printer will produce implants and other medical devices that are used in the treatment of illnesses. It is essential for biomedical engineers to learn about this technology in this regard. Applications for 3-D printers will be available for usage in laboratories at universities with biomedical engineering programs, and teaching these technologies to students will be extremely beneficial for

their educational advancement. Therefore, in order to use 3D technology, proficiency with 3D software is required. Throughout the first year of undergraduate study, several institutions provide computer-aided drawing sessions, which are recognized for assisting students in understanding and utilizing contemporary technology. This research attempts to reveal the details of this mechanism's function in biomedical engineering. Additionally, the study's key findings are highlighted in the paragraphs that follow.

- Between simulation and experimental data on femur fractures, there was an error of about 12%, which is rather similar to the literature.
- In the compression test, the fracture line was located in the femoral neck, likewise in the simulation, high-stress values were found on the same line.
- The correlation coefficients between simulations and experimental data ( $R^2=0.99$ ) are also higher than those of previous studies.
- In areas where fast prototyping is critical, such as pre-operative planning, BJ or SLS printer technologies are superior in many ways despite being pricey.

The following are significant inferences from the compression test on composite polyurethane bones.

- In AO OTA type 44A2 malleolar fractures, the novel medial malleolar compression plate outperforms the conventional one-third semitubular plate with lag screws in terms of biomechanical properties.
- In the MP group, twice as much force was needed to produce a displacement as in the TP group.
- The sliding mechanism generated extremely beneficial results in applying the axial force precisely to the correct position in the compression test.

In this study, there was significant demand for a sliding mechanism since there were so many samples of bone models. A lot of problems with 3D printers were found creating this mechanism. As a consequence, several problems have been resolved by the camera system created to rapidly intervene in incomplete printings. Additionally, it can be tracked in real-time via the application at any time and from any location. Also, this system can be utilized to create bone models for pre-operative planning or

similar purposes. As a result, in the case of a possible problem, both printing losses will be avoided with immediate action, and time losses will be compensated. On the other hand, for FDM-type printers, the filament weight tracking system alerts the user before the material runs out. By accomplishing this, in the event that there may be a material shortage, it can minimize the chance that a printer would use power in vain and that will encounter unforeseen circumstances.

The following is a summary of the outcomes from the analysis of miniscrew different head designs. As a consequence of the study, the bracket head had the least amount of stress. In contrast, the maximum stress was determined at the button head. In the mushroom head, button head, and bracket head, the stress was concentrated mostly on the collar and head sections. The study's findings lead to the prediction that bracket head designs will raise the success rate of miniscrew treatments. However, only five prominent miniscrew head designs were used in this investigation. Future research should include other head shapes and a more complicated model.

The study, which focused on the insertion methods and length characteristics of miniscrews, came to the following notable conclusions.

- A total of 36 different FE models were simulated, including miniscrew lengths, miniscrew insertion angles, and forces in various directions according to power arm lengths.
- The most suitable miniscrew length was determined to be 6 mm with a 60° insertion angle.
- The failure rate in treatments may rise when the chosen miniscrew length gets longer for use on the mandible as a temporary anchoring because it generates more stress.
- Although there was a significant difference between miniscrew lengths, no significant difference was observed in terms of insertion angles and force directions.
- At a ventral insertion angle of 15 degrees, the maximum stress value was observed.
- The shorter the power arm is used, the lower the stress occurs due to the increased force direction.

- A single parameter does not clearly dominate the others since several parameters affect miniscrew stability. The best conditions, nonetheless, are illustrated in this thesis.

## References

- [1] Hedlund R, Lindgren U. Trauma type, age, and gender as determinants of hip fracture. *J Orthop Res* 1987;5:242–6. <https://doi.org/10.1002/jor.1100050210>.
- [2] Blanco JF, da Casa C, Sánchez de Vega R, Hierro-Estévez MA, González-Ramírez A, Pablos-Hernández C. Oldest old hip fracture patients: centenarians as the lowest complexity patients. *Aging Clin Exp Res* 2020;32:2501–6. <https://doi.org/10.1007/s40520-020-01476-5>.
- [3] Tuzun S, Eskiuyurt N, Akarirmak U, Saridogan M, Senocak M, Johansson H, et al. Incidence of hip fracture and prevalence of osteoporosis in Turkey: the FRACTURK study. *Osteoporos Int* 2012;23:949–55. <https://doi.org/10.1007/s00198-011-1655-5>.
- [4] Groff H, Kheir MM, George J, Azboy I, Higuera CA, Parvizi J. Causes of in-hospital mortality after hip fractures in the elderly. *Hip Int* 2020;30:204–9. <https://doi.org/10.1177/1120700019835160>.
- [5] Nollin Z, Norris B. Complex bifocal femoral fractures. *Fracture Reduction and Fixation Techniques: Spine-Pelvis and Lower Extremity*, Springer; 2020, p. 235–51. [https://doi.org/10.1007/978-3-030-24608-2\\_18](https://doi.org/10.1007/978-3-030-24608-2_18).
- [6] Somersalo A, Paloneva J, Kautiainen H, Lönnroos E, Heinänen M, Kiviranta I. Incidence of fractures requiring inpatient care. *Acta Orthop* 2014;85:525–30. <https://doi.org/10.3109/17453674.2014.908340>.
- [7] Turgut A, Gönç U. Surgical approaches for the fractures of the medial and lateral malleolus. *TOTBID Dergisi* 2016;15:182–90. <https://doi.org/10.14292/totbid.dergisi.2016.24>.
- [8] Dumigan RM, Bronson DG, Early JS. Analysis of fixation methods for vertical shear fractures of the medial malleolus. *J Orthop Trauma* 2006;20:687–91.

- [9] Wegner AM, Wolinsky PR, Robbins MA, Garcia TC, Maitra S, Amanatullah DF. Antigliding plating of vertical medial malleolus fractures provides stiffer initial fixation than bicortical or unicortical screw fixation. *Clin Biomech* (Bristol, Avon) 2016;31:29–32. <https://doi.org/10.1016/j.clinbiomech.2015.10.005>.
- [10] Corey RM, Cannada LK, Bledsoe G, Israel H. Biomechanical evaluation of medial malleolus fractures treated with headless compression screws. *J Clin Orthop Trauma* 2019;10:310–4. <https://doi.org/10.1016/j.jcot.2018.04.010>.
- [11] Rajan K, Samykano M, Kadirgama K, Harun WSW, Rahman MM. Fused deposition modeling: process, materials, parameters, properties, and applications. *Int J Adv Manuf Technol* 2022;120:1531–70. <https://doi.org/10.1007/s00170-022-08860-7>.
- [12] Ventola CL. Medical applications for 3D printing: current and projected uses. *Pharmacy and Therapeutics* 2014;39:704.
- [13] Aimar A, Palermo A, Innocenti B. The role of 3D printing in medical applications: a state of the art. *J Healthc Eng* 2019;2019. <https://doi.org/10.1155/2019/5340616>.
- [14] Martorelli M, Gloria A, Bignardi C, Calì M, Maietta S. Design of additively manufactured lattice structures for biomedical applications. *J Healthc Eng* 2020;2020. <https://doi.org/10.1155/2020/2707560>.
- [15] Ramya A, Vanapalli SL. 3D printing technologies in various applications. *International Journal of Mechanical Engineering and Technology* 2016;7:396–409.
- [16] Chennakesava P, Narayan YS. Fused deposition modeling-insights. *Proceedings of the international conference on advances in design and manufacturing ICAD&M*, vol. 14, 2014, p. 1345.
- [17] Kun K. Reconstruction and development of a 3D printer using FDM technology. *Procedia Eng* 2016;149:203–11. <https://doi.org/10.1016/j.proeng.2016.06.657>.

- [18] Šljivic M, Pavlovic A, Kraišnik M, Ilić J. Comparing the accuracy of 3D slicer software in printed enduse parts. *IOP Conf Ser Mater Sci Eng*, vol. 659, IOP Publishing; 2019, p. 012082. <https://doi.org/10.1088/1757-899X/659/1/012082>.
- [19] Griffey J. 3-D printers for libraries. *Libr Technol Rep* 2017;53:1–31.
- [20] Pu'ad NASM, Haq RHA, Noh HM, Abdullah HZ, Idris MI, Lee TC. Review on the fabrication of fused deposition modelling (FDM) composite filament for biomedical applications. *Mater Today Proc* 2020;29:228–32. <https://doi.org/10.1016/j.matpr.2020.05.535>.
- [21] Dizon JRC, Gache CCL, Cascolan HMS, Cancino LT, Advincula RC. Post-processing of 3D-printed polymers. *Technologies (Basel)* 2021;9:61. <https://doi.org/10.3390/technologies9030061>.
- [22] Park S, Fu KK. Polymer-based filament feedstock for additive manufacturing. *Compos Sci Technol* 2021;213:108876. <https://doi.org/10.1016/j.compscitech.2021.108876>.
- [23] Shilov SY, Rozhkova YA, Markova LN, Tashkinov MA, Vindokurov I V, Silberschmidt V V. Biocompatibility of 3D-printed PLA, PEEK and PETG: adhesion of bone marrow and peritoneal lavage cells. *Polymers (Basel)* 2022;14:3958. <https://doi.org/10.3390/polym14193958>.
- [24] Hiemenz J. 3D printing with FDM: how it works. *Stratasys Inc* 2011;1:1–5.
- [25] Siemiński P. Introduction to fused deposition modeling. *Addit Manuf*, Elsevier; 2021, p. 217–75. <https://doi.org/10.1016/B978-0-12-818411-0.00008-2>.
- [26] Jerez-Mesa R, Gomez-Gras G, Travieso-Rodriguez JA, Garcia-Plana V. A comparative study of the thermal behavior of three different 3D printer liquefiers. *Mechatronics* 2018;56:297–305. <https://doi.org/10.1016/j.mechatronics.2017.06.008>.
- [27] Tuan Rahim TNA, Abdullah AM, Md Akil H, Mohamad D, Rajion ZA. Preparation and characterization of a newly developed polyamide composite

- utilising an affordable 3D printer. *J Reinf Plast Compos* 2015;34:1628–38. <https://doi.org/10.1177/0731684415594692>.
- [28] Doshi M, Mahale A, Singh SK, Deshmukh S. Printing parameters and materials affecting mechanical properties of FDM-3D printed parts: perspective and prospects. *Mater Today Proc* 2022;50:2269–75. <https://doi.org/10.1016/j.matpr.2021.10.003>.
- [29] Mazzoli A. Selective laser sintering in biomedical engineering. *Med Biol Eng Comput* 2013;51:245–56. <https://doi.org/10.1007/s11517-012-1001-x>.
- [30] Kumar MB, Sathiya P, Varatharajulu M. Selective laser sintering. *Advances in Additive Manufacturing Processes China: Bentham Books* 2021:28–47.
- [31] Schmid M, Simon C, Levy GN. Finishing of SLS-parts for rapid manufacturing (RM)-a comprehensive approach. 2009 International Solid Freeform Fabrication Symposium, University of Texas at Austin; 2009. <https://doi.org/10.26153/tsw/15081>.
- [32] Kruth J-P, Wang X, Laoui T, Froyen L. Lasers and materials in selective laser sintering. *Assembly Automation* 2003;23:357–71. <https://doi.org/10.1108/01445150310698652>.
- [33] Lupone F, Padovano E, Casamento F, Badini C. Process phenomena and material properties in selective laser sintering of polymers: a review. *Materials* 2021;15:183. <https://doi.org/10.3390/ma15010183>.
- [34] Ghalme SG, Mankar A, Bhalerao Y. Biomaterials in hip joint replacement. *Int J Mater Sci Eng* 2016;4:113–25. <https://doi.org/10.17706/ijmse.2016.4.2.113-125>.
- [35] Saffarzadeh M, Gillispie GJ, Brown P. Selective laser sintering (SLS) rapid prototyping technology: a review of medical applications. *Proceedings of the 53rd Annual Rocky Mountain Bioengineering Symposium, RMBS 2016 and 53rd International ISA Biomedical Sciences Instrumentation Symposium, Denver, CO, USA, 2016, p. 8–10.*

- [36] Lohfeld S, Tyndyk MA, Cahill S, Flaherty N, Barron V, McHugh PE. A method to fabricate small features on scaffolds for tissue engineering via selective laser sintering. *J Biomed Sci Eng* 2010;3:138. <https://doi.org/10.4236/jbise.2010.32019>.
- [37] Msallem B, Sharma N, Cao S, Halbeisen FS, Zeilhofer H-F, Thieringer FM. Evaluation of the dimensional accuracy of 3D-printed anatomical mandibular models using FFF, SLA, SLS, MJ, and BJ printing technology. *J Clin Med* 2020;9:817. <https://doi.org/10.3390/jcm9030817>.
- [38] Queral V, Rincón E, Mirones V, Rios L, Cabrera S. Dimensional accuracy of additively manufactured structures for modular coil windings of stellarators. *Fusion Engineering and Design* 2017;124:173–8. <https://doi.org/10.1016/j.fusengdes.2016.12.014>.
- [39] Ziaee M, Crane NB. Binder jetting: A review of process, materials, and methods. *Addit Manuf* 2019;28:781–801. <https://doi.org/10.1016/j.addma.2019.05.031>.
- [40] Lim IY, Ting CH, Ng CK, Tey JY, Yeo WH, Ramesh S, et al. 3D printing of high solid loading zirconia feedstock via screw-based material extrusion. *Ceram Int* 2023. <https://doi.org/10.1016/j.ceramint.2023.05.011>.
- [41] Mostafaei A, Elliott AM, Barnes JE, Li F, Tan W, Cramer CL, et al. Binder jet 3D printing—process parameters, materials, properties, modeling, and challenges. *Prog Mater Sci* 2021;119:100707. <https://doi.org/10.1016/j.pmatsci.2020.100707>.
- [42] Lv X, Ye F, Cheng L, Fan S, Liu Y. Binder jetting of ceramics: powders, binders, printing parameters, equipment, and post-treatment. *Ceram Int* 2019;45:12609–24. <https://doi.org/10.1016/j.ceramint.2019.04.012>.
- [43] Suwanprateeb J, Sanngam R, Panyathanmaporn T. Influence of raw powder preparation routes on properties of hydroxyapatite fabricated by 3D printing technique. *Materials Science and Engineering: C* 2010;30:610–7. <https://doi.org/10.1016/j.msec.2010.02.014>.

- [44] Wang Y, Zhao YF. Investigation of sintering shrinkage in binder jetting additive manufacturing process. *Procedia Manuf* 2017;10:779–90. <https://doi.org/10.1016/j.promfg.2017.07.077>.
- [45] Karakurt I, Lin L. 3D printing technologies: techniques, materials, and post-processing. *Curr Opin Chem Eng* 2020;28:134–43. <https://doi.org/10.1016/j.coche.2020.04.001>.
- [46] Kessler A, Hickel R, Reymus M. 3D printing in dentistry—State of the art. *Oper Dent* 2020;45:30–40. <https://doi.org/10.2341/18-229-L>.
- [47] Jiang J, Xu X, Stringer J. Support structures for additive manufacturing: a review. *Journal of Manufacturing and Materials Processing* 2018;2:64. <https://doi.org/10.3390/jmmp2040064>.
- [48] Surange VG, Gharat P V. 3D printing process using fused deposition modelling (FDM). *Int Res J Eng Technol* 2016;3:1403–6.
- [49] Hashmi AW, Mali HS, Meena A. The surface quality improvement methods for FDM printed parts: a review. *Fused Deposition Modeling Based 3D Printing*, Springer; 2021, p. 167–94. [https://doi.org/10.1007/978-3-030-68024-4\\_9](https://doi.org/10.1007/978-3-030-68024-4_9).
- [50] Ciklacandir S, Mihcin S, Isler Y. Detailed investigation of three-dimensional modeling and printing technologies from medical images to analyze femoral head fractures using finite element analysis. *IRBM* 2022;43:604–13. <https://doi.org/10.1016/j.irbm.2022.04.005>.
- [51] Eshkalak SK, Ghomi ER, Dai Y, Choudhury D, Ramakrishna S. The role of three-dimensional printing in healthcare and medicine. *Mater Des* 2020;194:108940. <https://doi.org/10.1016/j.matdes.2020.108940>.
- [52] Kumar P, Rajak DK, Abubakar M, Ali SGM, Hussain M. 3D printing technology for biomedical practice: a review. *J Mater Eng Perform* 2021;30:5342–55. <https://doi.org/10.1007/s11665-021-05792-3>.

- [53] Oberoi G, Nitsch S, Edelmayer M, Janjić K, Müller AS, Agis H. 3D Printing—encompassing the facets of dentistry. *Front Bioeng Biotechnol* 2018;6:172. <https://doi.org/10.3389/fbioe.2018.00172>.
- [54] Tran T, Liu W, Chen BK, Molotnikov A, Wu X, Pun J. CT-based agile 3D printing system for pre-operative planning of orthopaedic surgeries. *International Journal of Agile Systems and Management* 2020;13:48–59. <https://doi.org/10.1504/IJASM.2020.105868>.
- [55] Grant JA, Bishop NE, Götzen N, Sprecher C, Honl M, Morlock MM. Artificial composite bone as a model of human trabecular bone: the implant–bone interface. *J Biomech* 2007;40:1158–64. <https://doi.org/10.1016/j.jbiomech.2006.04.007>.
- [56] Stirling ERB, Lewis TL, Ferran NA. Surgical skills simulation in trauma and orthopaedic training. *J Orthop Surg Res* 2014;9:1–9. <https://doi.org/10.1186/s13018-014-0126-z>.
- [57] Elfar J, Stanbury S, Menorca RMG, Reed JD. Composite bone models in orthopaedic surgery research and education. *J Am Acad Orthop Surg* 2014;22:111. <https://doi.org/10.5435/JAAOS-22-02-111>.
- [58] Papini M, Zdero R, Schemitsch EH, Zalzal P. The biomechanics of human femurs in axial and torsional loading: comparison of finite element analysis, human cadaveric femurs, and synthetic femurs. *J Biomech Eng* 2007;129:12–9. <https://doi.org/10.1115/1.2401178>.
- [59] Heiner AD. Structural properties of fourth-generation composite femurs and tibias. *J Biomech* 2008;41:3282–4. <https://doi.org/10.1016/j.jbiomech.2008.08.013>.
- [60] Chung KJ, Huang B, Choi CH, Park YW, Kim HN. Utility of 3D printing for complex distal tibial fractures and malleolar avulsion fractures: technical tip. *Foot Ankle Int* 2015;36:1504–10. <https://doi.org/10.1177/1071100715595695>.

- [61] Nägl K, Reisinger A, Pahr DH. The biomechanical behavior of 3D printed human femoral bones based on generic and patient-specific geometries. *3D Print Med* 2022;8:35. <https://doi.org/10.1186/s41205-022-00162-8>.
- [62] Pal AK, Mohanty AK, Misra M. Additive manufacturing technology of polymeric materials for customized products: recent developments and future prospective. *RSC Adv* 2021;11:36398–438. <https://doi.org/10.1039/D1RA04060J>.
- [63] Ji K, Wang Y, Wei Q, Zhang K, Jiang A, Rao Y, et al. Application of 3D printing technology in bone tissue engineering. *Biodes Manuf* 2018;1:203–10. <https://doi.org/10.1007/s42242-018-0021-2>.
- [64] Wang Z, Runzi M, Gilchrist M, Gong H. Mechanical properties of high-performance plastic polyether-ether-ketone (PEEK) printed by fused deposition modeling. 2021 International Solid Freeform Fabrication Symposium, University of Texas at Austin; 2021. <https://doi.org/10.26153/tsw/17574>.
- [65] Wu W, Geng P, Li G, Zhao D, Zhang H, Zhao J. Influence of layer thickness and raster angle on the mechanical properties of 3D-printed PEEK and a comparative mechanical study between PEEK and ABS. *Materials* 2015;8:5834–46. <https://doi.org/10.3390/ma8095271>.
- [66] Vukasovic T, Vivanco JF, Celentano D, García-Herrera C. Characterization of the mechanical response of thermoplastic parts fabricated with 3D printing. *The International Journal of Advanced Manufacturing Technology* 2019;104:4207–18. <https://doi.org/10.1007/s00170-019-04194-z>.
- [67] Second-Generation Composite Bones n.d. <https://www.matweb.com/search/DataSheet.aspx?MatGUID=82d1e15c662d4c97b75df5e9d9171da9> (accessed March 2, 2023).
- [68] Properties of 3D Printing Materials n.d. <https://assets-eu-01.kc-usercontent.com/8ff24b0e-57a3-0157-62d1-fa4ac9734eb5/6b107d1d-6e8f-47ff-8d0a-ed69e1dfa308/materialise-datasheets-19-07-2022.pdf> (accessed March 2, 2023).

- [69] Ott SM. Cortical or trabecular bone: what's the difference? *Am J Nephrol* 2018;47:373–6. <https://doi.org/10.1159/000489672>.
- [70] Mirkhalaf M, Men Y, Wang R, No Y, Zreiqat H. Personalized 3D printed bone scaffolds: A review. *Acta Biomater* 2022. <https://doi.org/10.1016/j.actbio.2022.04.014>.
- [71] Mirkhalaf M, Goldsmith J, Ren J, Dao A, Newman P, Schindeler A, et al. Highly substituted calcium silicates 3D printed with complex architectures to produce stiff, strong and bioactive scaffolds for bone regeneration. *Appl Mater Today* 2021;25:101230. <https://doi.org/10.1016/j.apmt.2021.101230>.
- [72] James AP, Dasarathy B V. Medical image fusion: a survey of the state of the art. *Information Fusion* 2014;19:4–19. <https://doi.org/10.1016/j.inffus.2013.12.002>.
- [73] Acharya R, Wasserman R, Stevens J, Hinojosa C. Biomedical imaging modalities: a tutorial. *Comput Med Imaging Graph* 1995;19:3–25. [https://doi.org/10.1016/0895-6111\(94\)00043-3](https://doi.org/10.1016/0895-6111(94)00043-3).
- [74] Withers PJ, Bouman C, Carmignato S, Cnudde V, Grimaldi D, Hagen CK, et al. X-ray computed tomography. *Nat Rev Methods Primers* 2021;1:18. <https://doi.org/10.1038/s43586-021-00015-4>.
- [75] Cantatore A, Müller P. Introduction to computed tomography. Kgs Lyngby: DTU Mechanical Engineering 2011.
- [76] DenOtter TD, Schubert J. Hounsfield unit 2019.
- [77] Starly B, Fang Z, Sun W, Shokoufandeh A, Regli W. Three-dimensional reconstruction for medical-CAD modeling. *Comput Aided Des Appl* 2005;2:431–8. <https://doi.org/10.1080/16864360.2005.10738392>.
- [78] Wang P, Yang J, Hu Y, Huo J, Feng X. Innovative design of a helmet based on reverse engineering and 3D printing. *Alexandria Engineering Journal* 2021;60:3445–53. <https://doi.org/10.1016/j.aej.2021.02.006>.

- [79] Abdullah JY, Omar M, Pritam HMH, Husein A, Rajion ZA. Comparison of 3D reconstruction of mandible for pre-operative planning using commercial and open-source software. *AIP Conf Proc*, vol. 1791, AIP Publishing LLC; 2016, p. 020001. <https://doi.org/10.1063/1.4968856>.
- [80] Mandolini M, Brunzini A, Facco G, Mazzoli A, Forcellese A, Gigante A. Comparison of three 3D segmentation software tools for hip surgical planning. *Sensors* 2022;22:5242. <https://doi.org/10.3390/s22145242>.
- [81] Davis JR. *Tensile testing*. ASM international; 2004.
- [82] Material Testing Market. Newsmantraa 2022. <https://www.digitaljournal.com/pr/material-testing-market-size-and-share-latest-report-2021-2030-analysis-by-top-manufacturers-like-zwick-roell-germany-mts-systems-us-shimadzu-japan-and-tinius-olsen-us> (accessed June 4, 2023).
- [83] Gedney R. *Tensile testing basics, tips and trends*. Admet Quality Test & Inspection 2005.
- [84] Marrett R, Peacock DCP. Strain and stress. *J Struct Geol* 1999;21:1057–63.
- [85] Hall EO. *Yield point phenomena in metals and alloys*. Springer Science & Business Media; 2012.
- [86] Greaves GN, Greer AL, Lakes RS, Rouxel T. Poisson's ratio and modern materials. *Nat Mater* 2011;10:823–37.
- [87] Roylance D. *Stress-strain curves*. Massachusetts Institute of Technology Study, Cambridge 2001.
- [88] Vaidya A, Pathak K. Mechanical stability of dental materials. *Applications of nanocomposite materials in dentistry*, Elsevier; 2019, p. 285–305. <https://doi.org/10.1016/B978-0-12-813742-0.00017-1>.
- [89] Reddy JN. *Introduction to the finite element method*. McGraw-Hill Education; 2019.

- [90] Dhatt G, Lefrançois E, Touzot G. Finite element method. John Wiley & Sons; 2012.
- [91] Çıklaçandır S. Biomechanics of acetabular fractures with low energy trauma via finite element modeling and analysis. Izmir Katip Celebi University, 2019.
- [92] Xie J. A generic finite element solver by meta-expressions. Northwestern University, 2022.
- [93] Rho J-Y, Hobatho MC, Ashman RB. Relations of mechanical properties to density and CT numbers in human bone. *Med Eng Phys* 1995;17:347–55. [https://doi.org/10.1016/1350-4533\(95\)97314-F](https://doi.org/10.1016/1350-4533(95)97314-F).
- [94] Geraldes DM, Phillips ATM. A comparative study of orthotropic and isotropic bone adaptation in the femur. *Int J Numer Method Biomed Eng* 2014;30:873–89. <https://doi.org/10.1002/cnm.2633>.
- [95] Chen C-H, Chang C-S, Hsieh C-H, Tseng Y-C, Shen Y-S, Huang I-Y, et al. The use of microimplants in orthodontic anchorage. *J Oral Maxillofac Surg* 2006;64:1209–13. <https://doi.org/10.1016/j.joms.2006.04.016>.
- [96] Bussick TJ, McNamara Jr JA. Dentoalveolar and skeletal changes associated with the pendulum appliance. *Am J Orthod* 2000;117:333–43. [https://doi.org/10.1016/S0889-5406\(00\)70238-1](https://doi.org/10.1016/S0889-5406(00)70238-1).
- [97] McNamara Jr JA, Peterson Jr JE, Alexander RG. Three-dimensional diagnosis and management of class II malocclusion in the mixed dentition. *Semin Orthod*, vol. 2, Elsevier; 1996, p. 114–37. [https://doi.org/10.1016/S1073-8746\(96\)80048-X](https://doi.org/10.1016/S1073-8746(96)80048-X).
- [98] Haydar S, Üner O. Comparison of Jones jig molar distalization appliance with extraoral traction. *Am J Orthod* 2000;117:49–53. [https://doi.org/10.1016/S0889-5406\(00\)70247-2](https://doi.org/10.1016/S0889-5406(00)70247-2).
- [99] Costa A, Raffainl M, Melsen B. Miniscrews as orthodontic anchorage: a preliminary report. *Int J Adult Orthodon Orthognath Surg* 1998;13:201–9.

- [100] Kanomi R. Mini-implant for orthodontic anchorage. *J Clin Orthod* 1997;31:763–7.
- [101] Takano-Yamamoto T, Kuroda S. Titanium screw anchorage for correction of canted occlusal plane in patients with facial asymmetry. *Am J Orthod* 2007;132:237–42. <https://doi.org/10.1016/j.ajodo.2005.12.032>.
- [102] Park H-S, Kwon T-G, Sung J-H. Nonextraction treatment with microscrew implants. *Angle Orthod* 2004;74:539–49.
- [103] Jasoria G, Shamim W, Rathore S, Kalra A, Manchanda M, Jaggi N. Miniscrew implants as temporary anchorage devices in orthodontics: a comprehensive review. *J Contemp Dent Pract* 2013;14:993–9. <https://doi.org/10.5005/jp-journals-10024-1439>.
- [104] Kravitz ND, Kusnoto B. Risks and complications of orthodontic miniscrews. *Am J Orthod* 2007;131:S43–51. <https://doi.org/10.1016/j.ajodo.2006.04.027>.
- [105] Liou EJW, Pai BCJ, Lin JCY. Do miniscrews remain stationary under orthodontic forces? *Am J Orthod* 2004;126:42–7. <https://doi.org/10.1016/j.ajodo.2003.06.018>.
- [106] Maino BG, Pagin P, Di Blasio A. Success of miniscrews used as anchorage for orthodontic treatment: analysis of different factors. *Prog Orthod* 2012;13:202–9. <https://doi.org/10.1016/j.pio.2012.04.002>.
- [107] Papadopoulos MA, Papageorgiou SN, Zogakis IP. Clinical effectiveness of orthodontic miniscrew implants: a meta-analysis. *J Dent Res* 2011;90:969–76. <https://doi.org/10.1177/0022034511409236>.
- [108] Papageorgiou SN, Zogakis IP, Papadopoulos MA. Failure rates and associated risk factors of orthodontic miniscrew implants: a meta-analysis. *Am J Orthod* 2012;142:577–95. <https://doi.org/10.1016/j.ajodo.2012.05.016>.
- [109] Lim H-J, Choi Y-J, Evans CA, Hwang H-S. Predictors of initial stability of orthodontic miniscrew implants. *Eur J Orthod* 2011;33:528–32. <https://doi.org/10.1093/ejo/cjq122>.

- [110] Moon C-H, Lee D-G, Lee H-S, Im J-S, Baek S-H. Factors associated with the success rate of orthodontic miniscrews placed in the upper and lower posterior buccal region. *Angle Orthod* 2008;78:101–6. <https://doi.org/10.2319/121706-515.1>.
- [111] Kuroda S, Yamada K, Deguchi T, Hashimoto T, Kyung H-M, Yamamoto TT. Root proximity is a major factor for screw failure in orthodontic anchorage. *Am J Orthod* 2007;131:S68–73. <https://doi.org/10.1016/j.ajodo.2006.06.017>.
- [112] Migliorati M, Benedicenti S, Signori A, Drago S, Barberis F, Tournier H, et al. Miniscrew design and bone characteristics: an experimental study of primary stability. *Am J Orthod* 2012;142:228–34. <https://doi.org/10.1016/j.ajodo.2012.03.029>.
- [113] Radwan ES, Montasser MA, Maher A. Influence of geometric design characteristics on primary stability of orthodontic miniscrews. *J Orofac Orthop* 2018;79. <https://doi.org/10.1007/s00056-018-0131-7>.
- [114] Choi S-H, Kim S-J, Lee K-J, Sung S-J, Chun Y-S, Hwang C-J. Stress distributions in peri-miniscrew areas from cylindrical and tapered miniscrews inserted at different angles. *Korean J Orthod* 2016;46:189–98. <https://doi.org/10.4041/kjod.2016.46.4.189>.
- [115] Lin C-L, Yu J-H, Liu H-L, Lin C-H, Lin Y-S. Evaluation of contributions of orthodontic mini-screw design factors based on FE analysis and the Taguchi method. *J Biomech* 2010;43:2174–81. <https://doi.org/10.1016/j.jbiomech.2010.03.043>.
- [116] Radwan ES, Scribante A, Sfondrini MF, Montasser MA. Imaging software programs for reliable mathematical measurements in orthodontics. *Dent J (Basel)* 2020;8:81. <https://doi.org/10.3390/dj8030081>.
- [117] Bollero P, Di Fazio V, Pavoni C, Cordaro M, Cozza P, Lione R. Titanium alloy vs. stainless steel miniscrews: an in vivo split-mouth study. *Eur Rev Med Pharmacol Sci* 2018;22:2191–8.

- [118] Kim K-H, Chung C, Yoo H-M, Park D-S, Jang I-S, Kyung S-H. The comparison of torque values in two types of miniscrews placed in rabbits: tapered and cylindrical shapes-Preliminary study. *Korean J Orthod* 2011;41:280–7. <https://doi.org/10.4041/kjod.2011.41.4.280>.
- [119] Elias CN, Oliveira Ruellas AC de, Fernandes DJ. Orthodontic implants: concepts for the orthodontic practitioner. *Int J Dent* 2012;2012. <https://doi.org/10.1155/2012/549761>.
- [120] Emral ME. Assessment the effects of vertical direction control of the dentofacial structures with intrabony implant mechanics. Ankara University, 2012.
- [121] Melsen B, Verna C. Miniscrew implants: the Aarhus anchorage system. *Semin Orthod*, vol. 11, Elsevier; 2005, p. 24–31. <https://doi.org/10.1053/j.sodo.2004.11.005>.
- [122] Ye Y, Yi W, Fan S, Zhao L, Yu Y, Lu Y, et al. Effect of thread depth and thread pitch on the primary stability of miniscrews receiving a torque load : a finite element analysis. *J Orofac Orthop* 2023;84:79–87. <https://doi.org/10.1007/s00056-021-00351-w>.
- [123] Sucu M, Yilmaz B, Ramoğlu Sİ. Evaluation of initial stress distribution and displacement pattern of craniofacial structures with 3 different rapid maxillary expansion appliance models: a 3-dimensional finite element analysis. *Turk J Orthod* 2021;34:18. <https://doi.org/10.5152/TurkJOrthod.2021.20006>.
- [124] Perillo L, Jamilian A, Shafieyoon A, Karimi H, Cozzani M. Finite element analysis of miniscrew placement in mandibular alveolar bone with varied angulations. *Eur J Orthod* 2015;37:56–9. <https://doi.org/10.1093/ejo/cju006>.
- [125] Jasmine MIF, Yezdani AA, Tajir F, Venu RM. Analysis of stress in bone and microimplants during en-masse retraction of maxillary and mandibular anterior teeth with different insertion angulations: a 3-dimensional finite element analysis study. *Am J Orthod* 2012;141:71–80. <https://doi.org/10.1016/j.ajodo.2011.06.031>.

- [126] Ammar HH, Ngan P, Crout RJ, Mucino VH, Mukdadi OM. Three-dimensional modeling and finite element analysis in treatment planning for orthodontic tooth movement. *Am J Orthod* 2011;139:e59–71. <https://doi.org/10.1016/j.ajodo.2010.09.020>.
- [127] Fattahi H, Ajami S, Rafsanjani AN. The effects of different miniscrew thread designs and force directions on stress distribution by 3-dimensional finite element analysis. *J Dent* 2015;16:341.
- [128] Liu T-C, Chang C-H, Wong T-Y, Liu J-K. Finite element analysis of miniscrew implants used for orthodontic anchorage. *Am J Orthod* 2012;141:468–76. <https://doi.org/10.1016/j.ajodo.2011.11.012>.
- [129] Jiang C, Zhao G-F, Zhu J, Zhao Y-X, Shen L. Investigation of dynamic crack coalescence using a gypsum-like 3D printing material. *Rock Mech Rock Eng* 2016;49:3983–98. <https://doi.org/10.1007/s00603-016-0967-3>.
- [130] Akoglu H. User's guide to correlation coefficients. *Turk J Emerg Med* 2018;18:91–3. <https://doi.org/10.1016/j.tjem.2018.08.001>.
- [131] Jones DA, Cannada LK, Bledsoe JG. Are hook plates advantageous compared to antiglide plates for vertical shear malleolar fractures. *Am J Orthop (Belle Mead NJ)* 2016;45:E98-102.
- [132] Çıklaçandır S, Telli O, İşler Y. Real-time detection system for printing problems of three-dimensional printers. 2022 30th Signal Processing and Communications Applications Conference (SIU), IEEE; 2022, p. 1–4. <https://doi.org/10.1109/SIU55565.2022.9864919>.
- [133] Scribante A, Montasser MA, Radwan ES, Bernardinelli L, Alcozer R, Gandini P, et al. Reliability of orthodontic miniscrews: bending and maximum load of different Ti-6Al-4V titanium and stainless steel temporary anchorage devices (TADs). *Materials* 2018;11:1138. <https://doi.org/10.3390/ma11071138>.
- [134] Herman R, Cope JB. Miniscrew implants: IMTEC mini ortho implants. *Semin Orthod*, vol. 11, Elsevier; 2005, p. 32–9. <https://doi.org/10.1053/j.sodo.2004.11.006>.

- [135] Alrbata RH, Momani MQ, Al-Tarawneh AM, Ihyasat A. Optimal force magnitude loaded to orthodontic microimplants: a finite element analysis. *Angle Orthod* 2016;86:221–6. <https://doi.org/10.2319/031115-153.1>.
- [136] Sidhu M, Chugh VK, Dmello K, Mehta A, Chugh A, Tandon P. Evaluation of stress pattern caused by mini-implant in mandibular alveolar bone with different angulations and retraction forces: a three-dimensional finite element study. *Turk J Orthod* 2020;33:150. <https://doi.org/10.5152/TurkJOrthod.2020.19109>.
- [137] Akış H, Doruk C. Dentofacial effects of fixed functional appliances with or without mini screw anchorage in the treatment of class II division I malocclusion: A finite element analysis. *Turk J Orthod* 2018;31:7. <https://doi.org/10.5152/TurkJOrthod.2018.17026>.
- [138] Meher AH, Shrivastav SS, Vibhute PJ, Hazarey P V. Deflection and stress distribution around mini-screw implants: a finite element investigation into the effect of cortical bone thickness, force magnitude and direction. *J Orthod* 2012;39:249–55. <https://doi.org/10.1179/1465312512Z.00000000037>.
- [139] Poggio PM, Incorvati C, Velo S, Carano A. “Safe zones”: a guide for miniscrew positioning in the maxillary and mandibular arch. *Angle Orthod* 2006;76:191–7.
- [140] Park H-S, Lee Y-J, Jeong S-H, Kwon T-G. Density of the alveolar and basal bones of the maxilla and the mandible. *Am J Orthod* 2008;133:30–7. <https://doi.org/10.1016/j.ajodo.2006.01.044>.
- [141] Pollei JK. Finite element analysis of miniscrew placement in maxillary alveolar bone with varied angulation and material type. The University of North Carolina at Chapel Hill, 2009.
- [142] Kluess D, Soodmand E, Lorenz A, Pahr D, Schwarze M, Cichon R, et al. A round-robin finite element analysis of human femur mechanics between seven participating laboratories with experimental validation. *Comput Methods Biomech Biomed Engin* 2019;22:1020–31. <https://doi.org/10.1080/10255842.2019.1615481>.

- [143] Haider IT, Goldak J, Frei H. Femoral fracture load and fracture pattern is accurately predicted using a gradient-enhanced quasi-brittle finite element model. *Med Eng Phys* 2018;55:1–8. <https://doi.org/10.1016/j.medengphy.2018.02.008>.
- [144] Trabelsi N, Yosibash Z, Wutte C, Augat P, Eberle S. Patient-specific finite element analysis of the human femur—a double-blinded biomechanical validation. *J Biomech* 2011;44:1666–72. <https://doi.org/10.1016/j.jbiomech.2011.03.024>.
- [145] Lengsfeld M, Schmitt J, Alter P, Kaminsky J, Leppek R. Comparison of geometry-based and CT voxel-based finite element modelling and experimental validation. *Med Eng Phys* 1998;20:515–22. [https://doi.org/10.1016/S1350-4533\(98\)00054-X](https://doi.org/10.1016/S1350-4533(98)00054-X).
- [146] Hambli R, Allaoui S. A robust 3D finite element simulation of human proximal femur progressive fracture under stance load with experimental validation. *Ann Biomed Eng* 2013;41:2515–27. <https://doi.org/10.1007/s10439-013-0864-9>.
- [147] Swanson CE, Day GA, Yelland CE, Broome JR, Massey L, Richardson HR, et al. The management of elderly patients with femoral fractures a randomised controlled trial of early intervention versus standard care. *Med J Aust* 1998;169:515–8. <https://doi.org/10.5694/j.1326-5377.1998.tb123397.x>.
- [148] Arnal-Burró J, Pérez-Mañanes R, Gallo-del-Valle E, Igualada-Blazquez C, Cuervas-Mons M, Vaquero-Martín J. Three dimensional-printed patient-specific cutting guides for femoral varization osteotomy: do it yourself. *Knee* 2017;24:1359–68. <https://doi.org/10.1016/j.knee.2017.04.016>.
- [149] O'Reilly MK, Reese S, Herlihy T, Geoghegan T, Cantwell CP, Feeney RNM, et al. Fabrication and assessment of 3D printed anatomical models of the lower limb for anatomical teaching and femoral vessel access training in medicine. *Anat Sci Educ* 2016;9:71–9. <https://doi.org/10.1002/ase.1538>.
- [150] Popescu AT, Stan O, Miclea L. 3D printing bone models extracted from medical imaging data. 2014 IEEE International Conference on Automation, Quality and

Testing, Robotics, IEEE; 2014, p. 1–5.  
<https://doi.org/10.1109/AQTR.2014.6857890>.

- [151] Starosolski ZA, Kan JH, Rosenfeld SD, Krishnamurthy R, Annapragada A. Application of 3-D printing (rapid prototyping) for creating physical models of pediatric orthopedic disorders. *Pediatr Radiol* 2014;44:216–21. <https://doi.org/10.1007/s00247-013-2788-9>.
- [152] Chia HN, Wu BM. Recent advances in 3D printing of biomaterials. *J Biol Eng* 2015;9:1–14. <https://doi.org/10.1186/s13036-015-0001-4>.
- [153] Brouwers L, Pull ter Gunne AF, de Jongh MAC, van der Heijden FHWM, Leenen LPH, Spanjersberg WR, et al. The value of 3D printed models in understanding acetabular fractures. *3D Print Addit Manuf* 2018;5:37–46. <https://doi.org/10.1089/3dp.2017.0043>.
- [154] Bhushan B, Caspers M. An overview of additive manufacturing (3D printing) for microfabrication. *Microsyst Technol* 2017;23:1117–24. <https://doi.org/10.1007/s00542-017-3342-8>.
- [155] Hoang D, Perrault D, Stevanovic M, Ghiassi A. Surgical applications of three-dimensional printing: a review of the current literature & how to get started. *Ann Transl Med* 2016;4. <https://doi.org/10.21037/atm.2016.12.18>.
- [156] Kashapov LN, Kashapov NF, Kashapov RN, Pashaev BY. The application of additive technologies in creation a medical simulator-trainer of the human head operating field. *IOP Conf Ser Mater Sci Eng*, vol. 134, IOP Publishing; 2016, p. 012011. <https://doi.org/10.1088/1757-899X/134/1/012011>.
- [157] Zhang J, Yan C-H, Chui C-K, Ong S-H. Fast segmentation of bone in CT images using 3D adaptive thresholding. *Comput Biol Med* 2010;40:231–6. <https://doi.org/10.1016/j.compbiomed.2009.11.020>.
- [158] Straub J. Initial work on the characterization of additive manufacturing (3D printing) using software image analysis. *Machines* 2015;3:55–71. <https://doi.org/10.3390/machines3020055>.

- [159] Lyngby RA, Wilm J, Eiríksson ER, Nielsen JB, Jensen JN, Aanæs H, et al. In-line 3D print failure detection using computer vision. Joint Special Interest Group meeting between euspen and ASPE: Dimensional Accuracy and Surface Finish in Additive Manufacturing, 2017.
- [160] Huang J, Bumann A, Mah J. Three-dimensional radiographic analysis in orthodontics. *J Clin Orthod* 2005;39:421–8.
- [161] Gracco A, Cirignaco A, Cozzani M, Boccaccio A, Pappalettere C, Vitale G. Numerical/experimental analysis of the stress field around miniscrews for orthodontic anchorage. *Eur J Orthod* 2009;31:12–20. <https://doi.org/10.1093/ejo/cjn066>.

# Appendix

## Publications from the Thesis

### Conference Papers

1. Çıklaçandır S, Telli O, İşler Y. Real-Time Detection System for Printing Problems of Three-Dimensional Printers. 30th Signal Processing and Communications Applications Conference (SIU), IEEE; 2022, p. 1–4. <https://doi.org/10.1109/SIU55565.2022.9864919>.
2. Çıklaçandır S, Gokce Kara G, İşler Y. Investigation of Different Miniscrew Head Designs by Finite Element Analysis. 5th International Conference on Medical Devices (ICMD); 2022.
3. Çıklaçandır S, Çulha S, İşler Y. Design of a Real-Time Tracking System to Eliminate 3D Printing Errors Caused by Thermoplastic Materials. 5th International Conference on Medical Devices (ICMD); 2022. <https://doi.org/10.54856/jiswa.202212213>.

### Journal Articles

1. Cıklaçandır S, Culha S, Isler Y. Design of a Real-Time Tracking System to Eliminate 3D Printing Errors Caused by Thermoplastic Materials. *J Intell Syst Appl* 2022;5:82–85. <https://doi.org/10.54856/jiswa.202212213>.
2. Cıklaçandır S, Mihcin S, Isler Y. Detailed Investigation of Three-Dimensional Modeling and Printing Technologies from Medical Images to Analyze Femoral Head Fractures Using Finite Element Analysis. *IRBM* 2022;43:604–613. <https://doi.org/10.1016/j.irbm.2022.04.005>.
3. Bektas YE, Ozmanevra R, Cici H, Cıklaçandır S, Demirkiran ND, Isler Y, Basci O, Erduran M. A Novel Plate for Vertical Shear Fractures of Medial Malleolus: A Biomechanical Study. *J Am Podiatr Med Assoc* 2023;113:1–20. <https://doi.org/10.7547/22-100>.
4. Cıklaçandır S, Gokce Kara G, Isler Y. Investigation of Different Miniscrew Head Designs by Finite Element Analysis. *Turk J Orthod* 2023; ACCEPTED.

# Curriculum Vitae

Name Surname: Samet Çıklaçandır

## Education:

- |           |   |
|-----------|---|
| 2010–2011 | Erciyes University, School of Foreign Languages   |
| 2011–2015 | Erciyes University, Dept. of Biomedical Engineering (Major, 3.86)   |
| 2011–2015 | Erciyes University, Dept. of Electrical and Electronics Engineering<br>(Double Major, 3.69)                     |
| 2014–2016 | Anadolu University, Dept. of Management of Healthcare<br>Organizations (Associate Degree, Open Education, 3.15) |
| 2016–2016 | Hacettepe University, School of Foreign Languages (Advanced)  |
| 2016–2019 | Izmir Katip Celebi University, Dept. of Biomedical Technologies<br>(MSc, 3.79)                                  |
| 2017–2018 | Oulu University, Dept. of Biomedical Engineering, (Erasmus, fall<br>semester)                                   |
| 2019–2023 | Izmir Katip Celebi University, Dept. of Biomedical Technologies<br>(PhD, 3.95)                                  |

## Computer & Software Skills:

- Microsoft Office Tools, Adobe Photoshop, IBM SPSS
- MATLAB, Visual Studio C#
- LabVIEW, Proteus, BioPAC
- SolidWorks, AutoCAD, Geomagic Studio
- Ansys, Abaqus, Mimics, 3Matic

## Work Experience:

- |             |  |
|-------------|--|
| 2015 – 2016 | Control Engineer                                   |
| 2016 –      | Research Assistant (Izmir Katip Celebi University) |

## Memberships to Scientific Organizations:

IEEE

Certificates:

- Dynamic Web Programming – PHP, Elginkan Foundation Distance Education Center, 03.04.2023 - 30.04.2023
- Mobile Programming with Android, Elginkan Foundation Distance Education Center, 03.04.2023 - 30.04.2023
- Occupational Health and Safety, Elginkan Foundation Distance Education Center, 07.10.2019 - 20.10.2019
- Digital Image Processing, Elginkan Foundation Distance Education Center, 09.09.2019 - 06.10.2019
- Object Oriented Programming - Python, Elginkan Foundation Distance Education Center, 08.04.2019 - 05.05.2019
- Advanced Excel, Elginkan Foundation Distance Education Center, 04.03.2019 - 31.03.2019
- Neuro-linguistic programming (NLP), Elginkan Foundation Distance Education Center, 06.12.2018 - 12.12.2018
- Smart Relay and Micro Level PLC, Elginkan Foundation Distance Education Center, 05.11.2018 - 02.12.2018
- Object Oriented Programming - C Sharp, Elginkan Foundation Distance Education Center, 04.06.2018 - 01.07.2018
- Computer Aided 3D Design – SolidWorks, Elginkan Foundation Distance Education Center, 07.05.2018 - 03.06.2018
- Object Oriented Programming – JAVA, Elginkan Foundation Distance Education Center, 09.10.2017 - 03.12.2017
- Artificial Learning, Hacettepe University, Ankara, 21.08.2017 - 24.08.2017

Publication (Master's thesis):

Çıklaçandır S. Biomechanics of acetabular fractures with low energy trauma via finite element modeling and analysis, Department of Biomedical Technologies, Izmir Katip Celebi University, Izmir, Turkey, 2019.

Publications (Article):

1. Cıklacandır S, Isler Y. Portable Epilepsy Seizure Warning and Emergency Response Armband Design. *J Intell Syst Appl* 2020;3:1–5. <https://doi.org/10.54856/jiswa.202005091>
2. Mihcin S, Cıklacandır S, Kocak M, Tosun A. Wearable motion capture system evaluation for biomechanical studies for hip joints. *J Biomech Eng* 2021;143:044504. <https://doi.org/10.1115/1.4049199>.
3. Cıklacandır S, Culha S, Isler Y. Design of a Real-Time Tracking System to Eliminate 3D Printing Errors Caused by Thermoplastic Materials. *J Intell Syst Appl* 2022;5:82–85. <https://doi.org/10.54856/jiswa.202212213>.
4. Mihçin Ş, Cıklacandır S. Towards integration of the finite element modeling technique into biomedical engineering education. *Biomed Eng (Singapore)* 2022;34:2150054. <https://doi.org/10.4015/S101623722150054X>.
5. Cici H, Ozmanevra R, Bektas YE, Cıklacandır S, Demirkiran ND, Isler Y, Erduran M, Basci O. Biomechanical Comparison of a Closed-Loop Double Endobutton to a Lag Screw in Fixation of Posterior Malleolar Fractures. *J Foot Ankle Surg*, 2022;61:975–978. <https://doi.org/10.1053/j.jfas.2021.12.023>.
6. Cıklacandır S, Mihcin S, Isler Y. Detailed Investigation of Three-Dimensional Modeling and Printing Technologies from Medical Images to Analyze Femoral Head Fractures Using Finite Element Analysis. *IRBM*, 2022;43:604–613. <https://doi.org/10.1016/j.irbm.2022.04.005>.
7. Çıklaçandır S, İşler Y. A cost-effective solution for real-time measurement of human joint angles. *Karaelmas Sci Eng J* 2022;12:119-133. <https://doi.org/10.7212/karaelmasfen.1008037>.
8. Cıklacandır S, Isler Y. Priority assessment of procuring medical equipment in Turkish hospitals using input-weighted fuzzy logic architecture. *Expert Syst Appl* 2023;213:119195. <https://doi.org/10.1016/j.eswa.2022.119195>.
9. Bektas YE, Ozmanevra R, Cici H, Cıklacandır S, Demirkiran ND, Isler Y, Basci O, Erduran M. A Novel Plate for Vertical Shear Fractures of Medial Malleolus: A Biomechanical Study. *J Am Podiatr Med Assoc* 2023;113:1–20. <https://doi.org/10.7547/22-100>.

Publications (Conferences):

1. Çıklaçandır S, Mülayim N, Şahin S. Low-Cost Real-Time Measurement of the ECG, SPO<sub>2</sub> and Temperature Signals in the LabVIEW Environment for Biomedical Technologies Education. International Conference on Research in Education and Science (ICRES); 2017, p. 162–168.
2. Mülayim N, Çıklaçandır S, Can FC, Şahin S. Low-Cost Real-Time Electromyography (EMG) Data Acquisition Experimental Setup for Biomedical Technologies Education. International Conference on Research in Education and Science (ICRES); 2017, p. 155–161.
3. Çıklaçandır S, Karabiber Cura Ö, Kalafat Y, Can FC. Design a Robot Insect Inspired by the Camouflage Characteristics of the Leaf Insect. International Conference on Engineering Technologies (ICENTE); 2017, p. 668–671.
4. Çıklaçandır S, İşler Y. System Design for Entertainment Based Rehabilitation of the Upper Extremity. Medical Technologies National Congress (TIPTEKNO), IEEE; 2017, p. 364–367. <https://doi.org/10.1109/TIPTEKNO.2017.8238037>.
5. Çıklaçandır S, İşler Y. Design of a New Mechanism in Medical Applications with Laser. 26th Signal Processing and Communications Applications Conference (SIU), IEEE; 2018, p. 1–4. <https://doi.org/10.1109/SIU.2018.8404798>.
6. Çıklaçandır S. Finite Element Modelling for Acetabular Bone. Second International Students Science Congress; 2018, p. 97.
7. Çıklaçandır S. Printing of Radiological Images in 3D Printer and Applications of Biomedical Engineering. First International Technological Sciences and Design Symposium; 2018.
8. Çıklaçandır S, Aygün AB. Electroporation Technique in Tumor Treatment and Electronic Design of an Electroporator Device. First International Technological Sciences and Design Symposium; 2018.
9. Çizmeciogulları S, Mihçin Ş, Çıklaçandır S, Azizi E, Akan A. A novel methodology on evaluation of upper extremity motor functions. 9th International Biomechanics Conference; 2018, p. 384–386.
10. Mihcin S, Kose H, Cizmeciogullari S, Ciklacandir S, Kocak M, Tosun A, Akan A. Investigation of wearable motion capture system towards biomechanical modelling. 2019 IEEE International Symposium on Medical Measurements and

- Applications (MeMeA), IEEE; 2019, p. 1–5.  
<https://doi.org/10.1109/MeMeA.2019.8802208>.
11. Çıklaçandır S, İşler Y. Design of a Low-Cost Arduino-Based Respiratory and Sleep Apnea Detection System. International Conference of Applied Sciences Engineering Mathematics (ICASEM); 2020.
  12. Çıklaçandır S, İşler Y. Identification of Human Activities from Sensor Arrays of the Rokoko Smartsuit Pro using the Nearest Neighbor Classifier. International Conference of Applied Sciences Engineering Mathematics (ICASEM); 2021.
  13. Çıklaçandır S, Çulha S, İşler Y. Design of a Real-Time Tracking System to Eliminate 3D Printing Errors Caused by Thermoplastic Materials. 5th International Conference on Medical Devices (ICMD); 2022.  
<https://doi.org/10.54856/jiswa.202212213>.
  14. Çıklaçandır S, Gokce Kara G, İşler Y. Investigation of Different Miniscrew Head Designs by Finite Element Analysis. 5th International Conference on Medical Devices (ICMD); 2022.
  15. Çıklaçandır S, Telli O, İşler Y. Real-Time Detection System for Printing Problems of Three-Dimensional Printers. 30th Signal Processing and Communications Applications Conference (SIU), IEEE; 2022, p. 1–4.  
<https://doi.org/10.1109/SIU55565.2022.9864919>.
  16. Çıklaçandır FG, Çıklaçandır S, Semih U. Ensemble Learning Based Classification of Infected and Uninfected Cells. 2nd International Artificial Intelligence and Data Science Congress; 2022.
  17. Cıklaçandır S, Ozkan S, Isler Y. A Comparison of the Performances of Video-Based and IMU Sensor-Based Motion Capture Systems on Joint Angles. Innovations in Intelligent Systems and Applications Conference (ASYU), IEEE; 2022, p. 1–5. <https://doi.org/10.1109/ASYU56188.2022.9925507>.
  18. Karacaoglu B, Sahin AM, Cıklaçandır S, Yilmaz M, Mihcin S. Development of a Force Sensor for Biomechanical Simulations of a Cycling Activity. Medical Technologies Congress (TIPTEKNO), IEEE; 2022, p. 1–4.  
<https://doi.org/10.1109/TIPTEKNO56568.2022.9960221>.
  19. Cıklaçandır S, Yilmaz M, Ozmert OS, Sahin AM, Mihcin S. Comparison of Traditional, MRI, and 3D Scanning Anthropometric Measurements in Hand

Prosthesis Design. Medical Technologies Congress (TIPTEKNO), IEEE; 2022, p. 1–4. <https://doi.org/10.1109/TIPTEKNO56568.2022.9960218>.

Publication (Book Chapter):

Çıklaçandır S, Mihcin S. Biyomedikal Mühendisliğinde İnsan Hareketleri Yakalama Sistemleri. Eds: Günday A, Minaz MR, Gece Kitaplığı Yayınları; 2020.

Projects:

1. “Collecting data with wearable motion data collection systems and investigating and analyzing their suitability for biomechanical models”, Izmir Katip Celebi University Scientific Research Council Agency, 2019-GAP-MÜMF-0015, 19.04.2019 – 19.04.2020.
2. “3D Finite Element Analysis of the Effects of Different Rapid Maxillary Expansion Appliances on the Craniofacial Skeleton”, Izmir Katip Celebi University Scientific Research Council Agency, 2023-TDR-FEBE-0005, 10.05.2023 – 15.08.2023.